Silicon Carbide RF-MEM Resonators

by

Tomas A. Dusatko

Department of Electrical and Computer Engineering

McGill University, Montréal, Canada

A thesis submitted to McGill University in partial fulfillment of the requirements of the degree of

Master of Engineering

September 2006

Your file Votre référence
ISBN: 978-0-494-51437-5
Our file Notre référence
ISBN: 978-0-494-51437-5

Abstract

A low-temperature (<300°C) method to fabricate electrostatically actuated microelectromechanical (MEM) clamped-clamped beam resonators has been developed. It utilizes an amorphous silicon carbide (SiC) structural layer and a thin polyimide spacer. The resonator beam is constructed by DC sputtering a tri-layer composite of low-stress SiC and aluminum over the thin polyimide sacrificial layer, and is then released using a microwave O_2 plasma etch. Deposition parameters have been optimized to yield low-stress films (<50MPa), in order to minimize the chance of stress-induced buckling or fracture in both the SiC and aluminum. Characterization of the deposited SiC was performed using several different techniques including scanning electron microscopy, EDX and XRD.

Several different clamped-clamped beam resonator designs were successfully fabricated and tested using a custom built vacuum system, with measured frequencies ranging from 5MHz to 25MHz. A novel thermal tuning method is also demonstrated, using integrated heaters directly on the resonant structure to exploit the temperature dependence of the Young's modulus and thermally induced stresses.

Sommaire

Une méthode à basse température (<300°C) pour fabriquer une poutre résonatrice microélectronique (MEM) fixée aux extrémités actuée électrostatiquement a été développé. Elle utilise une couche structurale de carbure de silicium (SiC) amorphe et une mince entretoise de polyimide. La poutre résonatrice est construite en pulvérisant un composite de trois couche de SiC à basse tension et de l'aluminium au-dessus de la couche sacrificiel de mince polyimide, et est ensuite relâchée en utilisant des micro-ondes de plasma O2 gravé. Les paramètres de déposition ont été optimisés pour atteindre les feuils de basse tension (<50 MPa), pour minimisé les chances de flambage induit par la tension ou de fracture dans le SiC et l'aluminium. La caractérisation du SiC déposé a été fait en utilisant plusieurs différentes techniques incluant la microscopie électronique à balayage EDX, et XRD.

Plusieurs différente conception de poutre résonatrice fixée ont été fabriquées avec succès et éprouvés avec un système à vide fabriqué à mesure, avec une plage de fréquence mesurés entre 5 MHz à 25 MHz. Une nouvelle méthode à accorder thermiquement est aussi démontrée en utilisant des éléments électrique intégrés directement sur la structure résonatrice pour exploiter la dépendance de température sur le module de Young et les tensions induits thermiquement.

Acknowledgements

First and foremost, I would like to thank Frederic Nabki who played an important role in the conception and implementation of this work. Without his support, this project would not have been possible. Second, I would like to thank Professor Mourad El-Gamal for his continuous guidance throughout the entire length of this project. His advice and support was much appreciated.

I am also grateful to all of the people at the McGill Nanotools facility who have provided me with assistance throughout the course of this work: Don Berry, Neal Lemaire, Dr. Mathieu Nannini, and especially Vito Logiudice for his continuous support and ceaseless enthusiasm. I would also like to thank Professor Srikar Vengallatore, who provided me with much needed insight into many aspects of the project.

I would like to extend a special thanks to everyone in the mechanical and electrical workshops who helped design and assemble the custom built vacuum system required for this work: Bob Thomson, Jozsef Boka, and Don Pavlasek.

Lastly, I would also like to take this opportunity to thank my family and Marie-France, who have shown untiring patience and support, and who have continuously reminded me of my priorities and the need to keep things in perspective.

Table of Contents

Abstract ____ *i*

Sommaire ____ *ii*

Acknowledgements ____ *iii*

Chapter 1 Introduction ____ *1*

1.1 Motivation ____ **1**

1.2 MEMS-based Transciever Architectures ____ **3**

1.3 Miniaturization of High-Q Oscillators and Filters ____ **7**

1.4 Research Contributions of this Work ____ **13**

1.5 Thesis Organization ____ **14**

1.6 References ____ **15**

Chapter 2 Resonator Theory of Operation and Modeling ____ *18*

2.1 Modal Analysis of MEM Resonators ____ **19**

2.2 Quality Factor ____ **26**

2.2.1 Gas Damping ____ 27

2.2.2 Anchor Loss ____ 27

2.2.3 Thermo-elastic Damping ____ 28

2.2.4 Q-loading by External Circuitry ____ 30

2.3 Small-signal Resonator Model ____ **32**

2.3.1 Mechanical modeling of MEM resonators ____ 32

2.3.2 Capacitive transduction and sensing ____ 38

2.3.3 Small-signal electrical model ____ 41

2.4 Selective Excitation of Beam Resonators ____ **46**

2.5 Non-linearity in MEM Resonators ____ **49**

2.5.1 Frequency Pulling ____ 50

2.5.2 Material Hardening and Higher-order Spring Constants ____ 52

2.6 Temperature Stability ____ **56**

2.7 References ____ **58**

Chapter 3 Fabrication Technology ____ *61*

3.1 Process Requirements ____ **62**

3.1.1 MEM Resonator Requirements ____ 62

3.1.2 CMOS/Bipolar Integration 63
3.1.3 A Simplified Surface Micromachining Process Flow 63

3.2 Structural Layer 65
3.2.1 Material Selection 65
3.2.2 Deposition of SiC 67
3.2.2.1 Deposition Rate 70
3.2.2.2 Material Study Results 72
3.2.2.3 Stress Control 78
3.2.3 Etching of SiC 81
3.2.3.1 Etch rate 82
3.2.3.2 Residue 85

3.3 Interconnect Layer 94
3.3.1 Deposition of Al 94
3.3.2 Etching of Al 96

3.4 Sacrificial Layer 97
3.4.1 Chromium 98
3.4.1.1 Deposition 98
3.4.1.2 Etching 98
3.4.2 Polyimide 99
3.4.2.1 Deposition 100
3.4.2.2 Etching 101

3.5 Substrate 102

3.6 Complete Process Overview 102

3.7 References 105

Chapter 4 MEM Resonators Fabrication and Testing 109

4.1 Fabricated Devices 109
4.1.1 Standard Clamped-clamped Beam 110
4.1.2 Standard Clamped-clamped Beam with Electrode Shaping 113
4.1.3 Standard Clamped-clamped Beam with Integrated Heaters 114

4.2 Measurement of Resonator Gap Thickness 116

4.3 Measurement Setup 120
4.3.1 Dicing and Packaging 120
4.3.2 Vacuum System and Test Fixture 123
4.3.3 Measurement Setup 125

4.4 DC Test Results 126

4.5 AC Measurements 129
4.5.1 Q-factor 130
4.5.2 Resonant Frequency 136
4.5.3 Frequency Tuning Using Integrated Heaters 139
4.5.4 Q-factor vs. Input power 142

4.6 References 144

Chapter 5 Conclusion 146

5.1 Summary 146

5.2 Topics for Future Research 147

5.2.1 Process Optimization 147
5.2.2 CMOS/bipolar Integration 148
5.2.3 Resonator Temperature Dependence and Long Term Stability 148

Chapter 1 Introduction

1.1 MOTIVATION

Due to the increasing interest in mobile communication, there is a large demand for the development of low-power, compact, and inexpensive wireless transceivers. Pursuant to this goal, heterodyning architectures used today typically minimize or eliminate the number of off-chip components required for filtering and reference frequency generation. Specifically, the ultra-stable quartz crystals and the RF ceramic and SAW filters responsible for band and channel selection are typically large and costly. These components alone can be responsible for the majority of the real-estate required for a complete system, and represent a sizeable cost. Furthermore, this issue will most likely become a significant bottleneck to the development of reconfigurable, multi-band handsets which may require a different set of off-chip components for each band. Although the number of these components can be reduced by appropriate selection of the transceiver architecture, it is usually at the expense of more complex transistor circuits and greater power consumption [1].

Recently, the development of micro-electro-mechanical (MEM) resonators and filters with quality factors (Q-factor) on the order of >10,000 have shown great promise for reducing the cost, power-consumption and size of mobile handsets. These micro-devices take a fraction of the space required by typical off-chip quartz and ceramic RF filters, and consume little to no DC power; for example, a typical surface-mount quartz crystal can occupy an area of >50mm^2 [2], while a MEM resonator with comparable properties may take as little as 2000μm^2, which represents an area reduction of ~25,000x. More importantly, however, is that these micro-mechanical devices can be fabricated using a wide range of materials and processes that are commonly used in the microelectronics industry, and thus are amenable to monolithic integration. By combining these high-Q MEM resonators and filters directly with

active electronics, a fully integrated transceiver can be envisioned which requires no external passive devices. Furthermore, as a result of the availability of a large number of MEM high-Q filters, new transceiver architectures that emphasize the use of high-Q devices as opposed to minimizing them may be possible [3].

The main hurdle to direct integration with CMOS and bipolar technologies, however, remains the high-temperature deposition processes used to fabricate these devices. Depending on the metallization scheme, pre-fabricated electronics can only withstand limited additional thermal processing. To prevent unwanted diffusion of the doped areas, the temperature must be kept below ~800-900°C. If the interconnects are made of aluminum, the maximum temperature must further be limited to no greater than ~400°C [4]. In the past, polysilicon was the most commonly used structural material for MEM resonators (e.g. [5]-[12]) as it has good mechanical properties and the deposition processes are mature. Although good for fabricating resonant structures, the high deposition temperatures involved preclude processing of CMOS/bipolar wafers with aluminum metallization. To get around these temperature restrictions, researchers at the University of Berkeley have replaced the aluminum interconnects with tungsten, however, at the cost of higher complexity and reduced transistor performance [13]. Another approach is to integrate the MEMS fabrication flow directly with the electronics, and perform all high-temperature steps before metallization. Although this method has been used successfully in the past, such as in the commercially available accelerometers produced by Analog Devices [14], it does not have the flexibility associated with an "electronics-first" approach.

The issue of temperature budget is aggravated even further with the desire to integrate new materials into MEM devices. Conventional MEMS fabrication processes have generally used silicon structural layers because of the availability of mature deposition and etching methods, however, a recent trend to push RF-MEM devices into the UHF range has spurred a flurry of research into alternatives. Most of the best alternatives to Si are in the ceramic-class of materials such as silicon carbide (SiC), alumina (Al_2O_3), or diamond (C). These materials are characterized by their high stiffness and Young's modulus; however, typical chemical-vapor deposition (CVD) processes for these materials require very high temperatures that are not

compatible with pre-fabricated electronics; for example, traditional CVD of SiC is usually done at temperatures in excess of 900-1000°C.

This work attempts to address the problem of integrating MEM resonators with active electronics. A low-temperature (<300°C) silicon carbide-based surface micromachining process module has been developed that is intended to be compatible with CMOS/bipolar technologies that use aluminum interconnects. Not only does this process allow for a modular fabrication approach for integrating MEM resonators with active electronics, but it also uses silicon carbide which has superior mechanical and chemical properties.

1.2 MEMS-BASED TRANSCIEVER ARCHITECTURES

A complete MEMS based transceiver architecture was first proposed by C. T.-C. Nguyen [3]. With the successful fabrication of micro-mechanical resonators with Q's in excess of >10000, new super-heterodyning architectures become possible with all large off-chip passive components replaced with micromachined RF devices. Shown in Figure 1-1 is a simplified receive path of a super-heterodyne architecture.

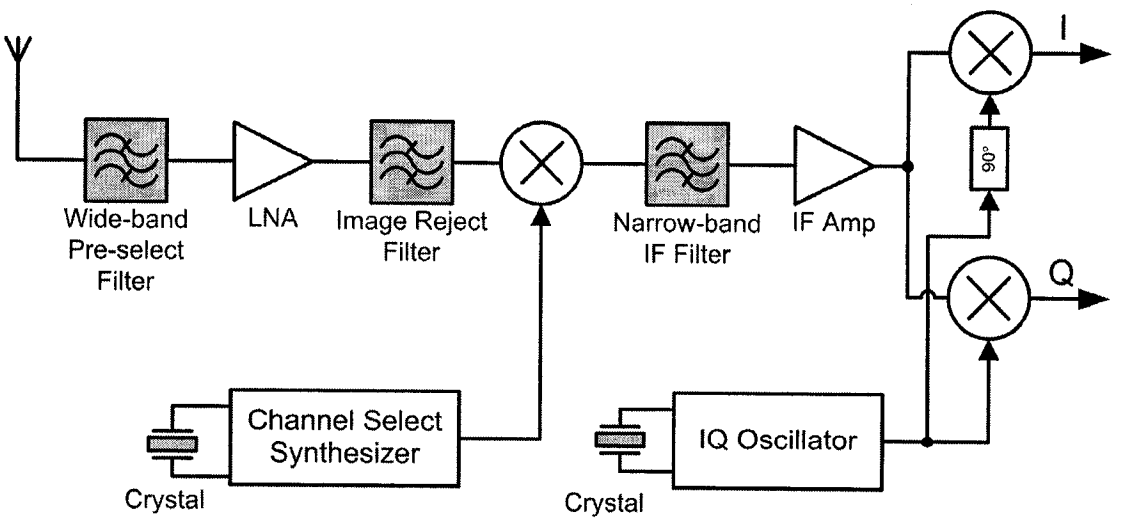

Figure 1-1: Simplified super-heterodyne receiver architecture

In this figure, all components which are traditionally implemented off-chip are shaded in grey. Specifically, the RF filters used for band-selection and image rejection along with the IF filter are typically implemented using large ceramic or SAW filters, since on-chip LC filters are not able to provide the necessary high-Q. A similar situation exists for the generation of the reference tone that is used in the channel selection synthesizer. To ensure both long and short term stability, it is typically locked to an off-chip quartz crystal which acts as the oscillator's reference. If the Q of the crystal is greater than about ~1000, the reference frequency will not be significantly affected by the temperature dependence of the active electronics, which is typically very large, and will depend mainly on the crystal properties. Typical uncompensated AT-cut quartz crystals have a frequency drift of around ±50ppm over the temperature range from -20°C to 70°C [2], which is orders of magnitude better than that achievable with active electronics only.

Replacing these external components with their micromachined on-chip equivalents, however, may allow for comparable (if not better) performance. One major advantage of using MEM high-Q devices over their external counterparts is that they can be used in large numbers, without increasing the overall cost of the system. Thus, they can be arrayed into large filter banks for band and even channel selection at RF. Using this idea, two possible transceiver architectures have been proposed [3].

The first and most straightforward one is to simply replace all off-chip components with on-chip micromachined ones. Although this does not necessarily exploit the full potential of micromachined devices, it still allows for monolithic integration, significantly reducing the overall assembly cost. This is illustrated in Figure 1-2, where all the off-chip components in grey are replaced with their micromachined equivalent.

Recently, MEM resonators with high-Qs at frequencies beyond 1GHz have been demonstrated [15], which indicates that band and possibly channel selection can be performed at RF. Similarly, by combining several resonators into arrays, low-insertion loss bandpass filters have also been demonstrated from HF to UHF frequencies [6],[16]-[19]. By combining these MEM resonators with a trans-impedance amplifier in a positive feedback loop, low-phase noise reference oscillators can also be created to replace the quartz reference

crystal. Recently, an array of disk resonators used as a reference oscillator was shown to meet the stringent GSM phase noise requirements [20].

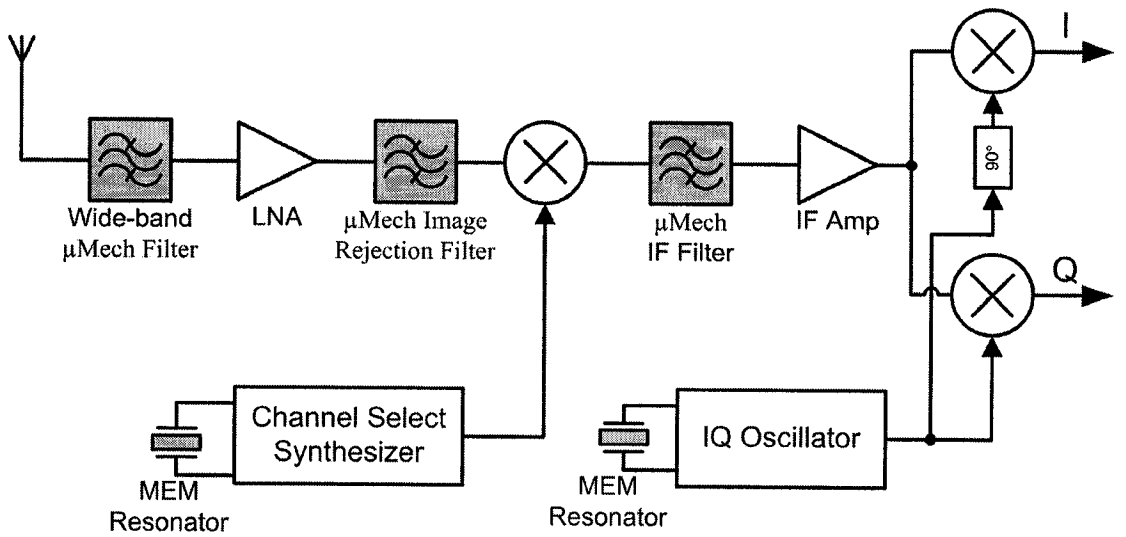

Figure 1-2: Super-heterodyne architecture with off-chip components replaced by MEM devices

Another variant of the super-heterodyne architecture which makes better use of the large-scale integration afforded by MEM resonators is shown in Figure 1-3 [1]. In this case, the image reject and pre-select filters are replaced by a bank of switchable high-Q MEM resonators that select the desired channel directly at RF frequencies. Since MEM resonators can be integrated in large numbers, this bank could contain hundreds of high-Q filters which can be used to implement a truly multi-band reconfigurable handset. One of the major advantages of MEM resonators is that they can be switched on and off by simply removing the bias voltage, and thus there is no need for lossy series switches in the receive path, which can greatly degrade the overall noise figure of the system [21]. Similarly, the conversion down to IF is also performed with a programmable bank of micromechanical oscillators. Instead of using a PLL for fine channel selection, which consumes a significant amount of power, each channel has a separate micromechanical oscillator which can be switched on or off. Lastly, the mixer is implemented using the inherent non-linearity of the MEM resonator, and can be used to both mix the RF signal down to IF and filter out unwanted channels [22].

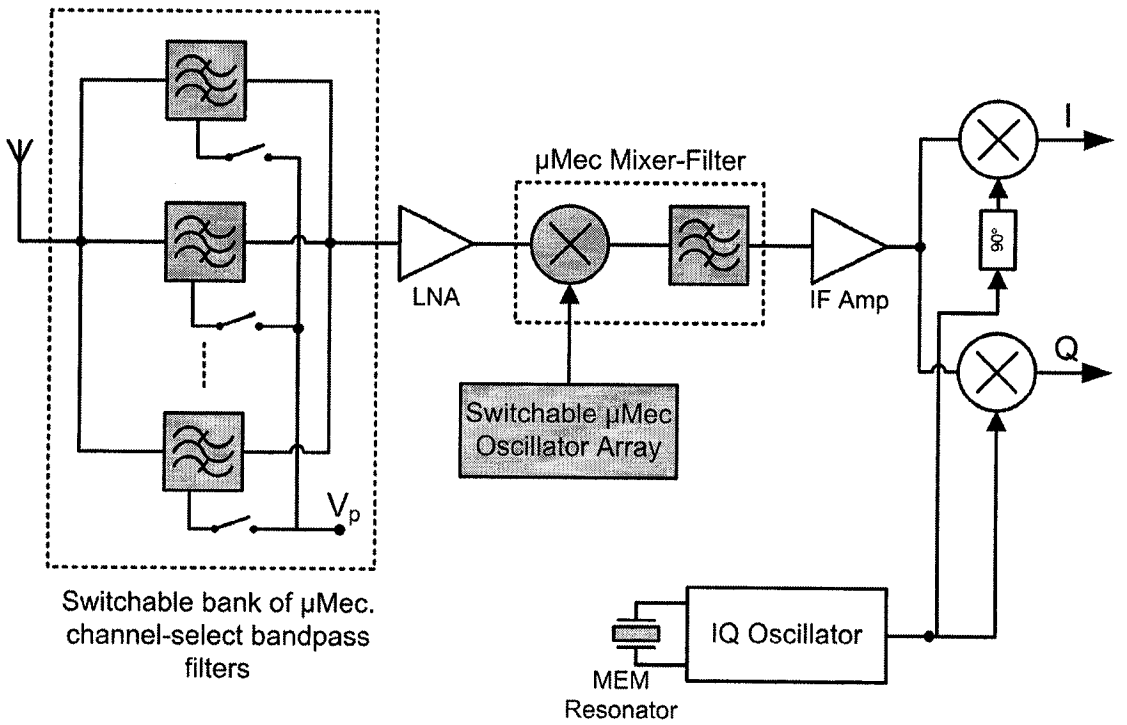

Figure 1-3: New MEMS-based receiver architecture

Besides the inherent area and cost savings, this particular architecture can be used to trade off high-Q for power consumption [3]. First, since channel selection is done at RF, the dynamic range and linearity requirements of the LNA in the receive path can be reduced, since high-power out-of-band interfering signals are significantly attenuated; for example, in CDMA cellular systems, the IIP_3 of the LNA is selected to avoid densitization by a single tone (generated by AMPS) 900kHz away from the CDMA signal center frequency and must be greater than +7.6dBm [23]. As shown in [3], however, if the MEM channel select filter can reject the single tone by 40dB, then the linearity requirement on the LNA relaxes to less than -29dBm. Another advantage of the reduced level of interfering signals is that the local-oscillator phase-noise requirements can also be relaxed. This helps to further reduce the power-consumption of the system.

Although the performance of MEM devices have become as good (or better) than their macroscopic counterparts, several issues still need to be addressed before they can become a commercially viable technology. The most significant is the stability of these devices with

changes in the ambient temperature. One of the main advantages of using quartz crystals is that the resonant frequency is relatively stable with temperature, and typically varies less than 50ppm over the commercial temperature range. MEM devices, however, are typically not as stable and therefore require some type of temperature compensation. A recent attempt to mitigate this problem using electronic compensation showed a dramatic improvement in temperature stability [24]; however, the performance is still not comparable to that achievable with compensated quartz crystals.

1.3 MINIATURIZATION OF HIGH-Q OSCILLATORS AND FILTERS

In all of the MEM components described above, the basic building block is a micromechanical resonator. Every mechanical structure has a natural mode of resonance; however, on the macro scale, these occur at very low frequencies - typically lower than a few kilo-Hertz. By shrinking the size into the micro-scale, these devices can take advantage of scaling induced phenomena such as reduced power consumption and higher frequency of oscillation. For a single beam that is 50μm long and clamped at both ends (Figure 1-4) the flexural-mode resonant frequency can be in excess of 5MHz, depending on the material. For smaller beams, the resonant frequency can be pushed as high as ~100MHz.

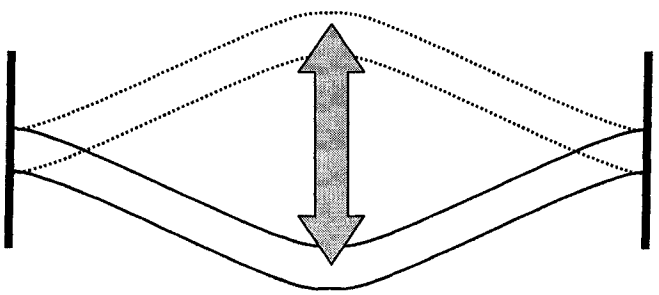

Figure 1-4: Flexural-mode resonance of a simple clamped-clamped beam

Micromechanical resonator designs have varied significantly over the last several years, and development has proceeded in two different directions: electro-statically actuated resonators

and piezo-electric film bulk-acoustic resonators. Piezoelectric films can be used to generate bulk-acoustic-waves (BAW) and, in recent years, have been successfully implemented as high-frequency reference oscillators and filters [25]-[27]; however, one of the major drawbacks of this technology is that the resonant frequency of these resonators is dependant on the thickness of the film. As a result, it is difficult to create resonators with different frequencies on the same chip since film thicknesses on a given layer are fixed by the process.

Electro-statically actuated MEM devices allow for more design flexibility since the resonant frequency is set by geometry, which can be easily modified for different applications. Initial electrostatic resonator designs were mostly based on a comb-drive connected to a large shuttle mass that vibrated laterally on the substrate [5]. Although effective as a proof-of-concept, these designs had very little practical value, as their resonant frequencies were well below 500KHz - the main reasons being the large mass of the structure and relatively low spring constant. The next generation of designs concentrated on increasing the resonant frequency of the devices, while preserving a reasonable Q value (Q>1000), and were based on the simple clamped-clamped poly-silicon cantilever beam [6]. Although this structure has the potential of generating high-frequency signals, energy loss to the substrate through the anchors makes these designs impractical for applications requiring Q's in excess of 10,000. Also, in order to generate signals greater than a few 100MHz, the length of the cantilever beam becomes very small and subject to variations in processing and mass loading. Another dominant form of energy loss for this design is squeeze-film damping. To obtain a reasonable Q-factor, these designs must be operated in a vacuum in the order of a few milliTorr. This raises further issues about packaging and integration.

The second generation of beam resonators was centered around a 'free-free' design [7], where the vibrating structure was a beam that was suspended above the substrate at nodal points (Figure 1-5).

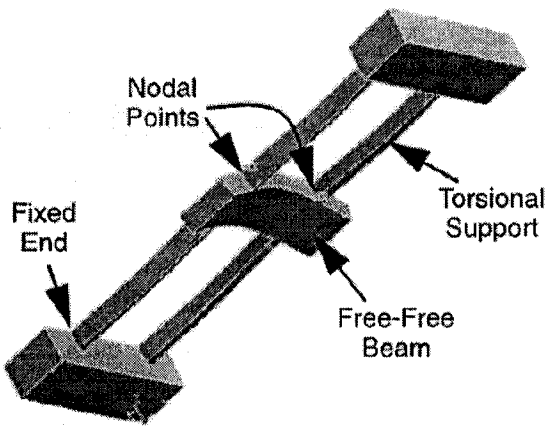

Figure 1-5: Free-free beam resonator design [6]

This significantly increased the Q-factor of the device, since it greatly reduced energy losses to the substrate; however, viscous gas-damping was still a large issue. Designs of this type were fabricated and successfully operated at frequencies from 30-90MHz [7]. Using this technique, other similar designs using higher-order modes were used to generate signals up to 102MHz. Also, because of the complex flexural mode shape, differential signals could be generated [8]-[9].

Because of the need for resonators that could reach the UHF range and beyond, in the last few years, a new generation of resonators has been developed that utilize bulk-acoustic waves. The bulk acoustic resonance mode has a very high effective stiffness, and thus can be used to generate high frequencies with very high Q-factors. Since the amount of energy stored in the device is related to the stiffness, these high-k resonators store a much larger amount of kinetic energy [11]; for example, the spring constant of a typical 1GHz BAW resonator is on the order of 100MN/m, while that of a flexural mode beam is on the order of 1500N/m. Thus, the losses due to gas-damping for the BAW resonators are a much smaller percentage of the total energy, which yields a much higher Q-factor. Also, for a given frequency, the characteristic dimensions of the devices tend to be much larger than their flexural-beam counterpart. This makes fabrication easier and more reliable.

The most commonly used shape for recent BAW resonators has been the disk structure, because of its simplicity and the number of available resonant modes that can be exploited. The first order contour mode of a disk is illustrated in Figure 1-6.

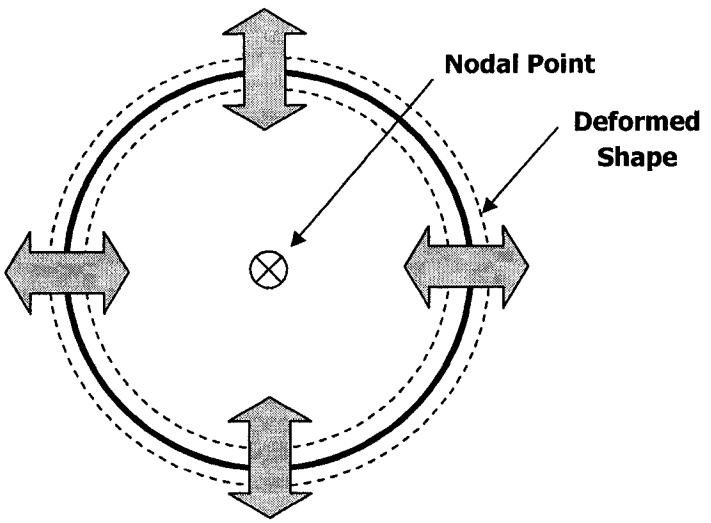

Figure 1-6: First radially symmetric resonant mode of a disk

In this case, the entire diameter of the disk increases and contracts in a way similar to breathing. Recent developments on this design have centered on the support structure, process improvement, and the exploration of new materials. Originally made in poly-silicon, the first successful disk resonator was fabricated with a diameter of 34μm and had a resonant frequency of 160MHz with a Q-factor of over 9000 in vacuum [28].

The main problem with this design was that, if the single central support was not placed at the exact center of the device (due to inevitable alignment errors between masking steps), then the Q-factor was greatly reduced. This raised problems regarding the reliability of the design, if it were ever to be implemented in an industrial application. To solve this problem, Nguyen and his research group pioneered a new process where the single support stem was self-aligned to the resonator disk [12]. In this process, a stem hole was first etched through the resonator disk and subsequently filled with poly-silicon. This ensured that there would be

no alignment errors, since the disk and the stem were essentially patterned using the same lithographic mask. With this technique, poly-silicon disk resonators were again successfully fabricated with resonant frequencies as high as 1.14GHz, with a Q-factor of >1000 *in air*. Because of the high-stiffness and low-energy loss to the substrate, high-Q could still be maintained at atmospheric pressure. Another disk design has also been explored that uses a lower-frequency mode of operation (the wineglass resonator) and has lateral support structures at nodal points. This design operated at a frequency of 73.4MHz, with an amazing Q-factor of 98000 in vacuum, the largest reported to date for a disk resonator [10]. In 2004, Nguyen's team also unveiled a diamond-disk resonator that was successfully fabricated and resonated at 1.51GHz with a Q-factor of >11000 in vacuum, the highest frequency of a mechanical resonator, to date [29].

One of the main issues with the disk resonator is its large motional resistance, which makes future use with electronics challenging. Because of its high stiffness, the motional resistance of the device is very large. If the resonator is used in a filter, the large motional resistance necessitates the use of large terminating resistors to reduce the pass-band ripples [30]. It also introduces a significant noise component, since the Brownian noise generated by the device is directly related to the size of the motional resistance. If the resonator is to be used in an oscillator, this large resistance necessitates the use of a trans-impedance amplifier with an enormous gain. Also, the high motional resistance may limit the highest attainable frequency for a given circuit technology [30]. Although research is still ongoing, there have been several potential solutions to this problem. One solution is to create banks of identical filters that resonate at the same frequency. In this case, the motional resistance of each of the resonators combines in parallel in order to reduce the overall resistance. The main difficulty with this solution is that, if there is even a small variation between the resonant frequencies of the different devices, the combined frequency response will create significant ripples in the pass-band [17].

Recently, a new circular BAW design has been explored. This new design is comprised of an annulus, instead of a disk [31]. The main advantage is that the high-frequency resonant modes are almost completely independent of the average radius of the ring; the resonant

frequency of this structure is in fact determined by the width of the ring. Thus, the width of the ring can be used to set the resonant frequency of the device, while the average radius can be increased to reduce the effective motional resistance to the desired level. Using this structure, a prototype has demonstrated a Q-factor of 14600 at a resonant frequency of 1.2GHz, but with a series resistance that is 12x smaller than its disk BAW counterpart [15]. The main design challenge for this device is supporting the structure in such a way that energy loss to the substrate is minimized. There are still many different modes that have yet to be explored, especially those compound modes which could be used to generate differential signals.

Another important metric for resonators is the Q-factor-frequency (Q-f) product. For high-quality AT-cut quartz crystal oscillators, this value is constant and has a value of approximately $1.6x10^{13}$ Hz [29]. Whether this empirical relation exists for MEM resonators still remains to be seen, however, some general trends can be seen in the literature. Summarized inTable 1-1 are the highest Q-frequency products that have been published to date for poly-silicon resonators. Note that the highest Q-f product was obtained using a bulk-acoustic-wave ring resonator which has high-isolation and an extremely high spring constant. Furthermore, this value is on par with those for high-quality quartz crystals, which is promising. As can be seen from this table, and as expected, the beam designs clearly do not perform as well as the BAW resonators. Although the potential limit for the Q-frequency product for poly-silicon seems to be on the order of 10^{13} Hz, the development of new materials will continue to increase this limit. Two possible candidates are silicon carbide and diamond - both have excellent acoustic properties.

Table 1-1: Q-frequency product for several published polysilicon resonators

Type	Frequency (MHz)	Q	Q-Frequency Product (x1e12 Hz)
Annulus BAW [15]	1200	14600	17.5
Stemless disk BAW [10]	73	98000	7.15
Self-aligned disk BAW [12]	732	7330	5.4
Disk BAW [28]	160	9400	1.5

Type	Frequency (MHz)	Q	Q-Frequency Product (x1e12 Hz)
Higher-mode free-free beam [9]	102	11500	1.17
Free-free beam [7]	92	7450	0.7
Clamped-clamped beam [6]	8.51	8000	0.07

1.4 RESEARCH CONTRIBUTIONS OF THIS WORK

This work describes a new, surface micromachining process that is intended to address the current need for RF-MEMS fabrication technologies that can be integrated with active electronics. Currently, most MEM filters are made from poly-silicon at relatively high temperatures, and thus are not amenable to "post-electronics" fabrication. As a result, most processes that include active electronics and MEMS functionality intertwine the steps required for fabricating electronics. Although this method probably yields the best results, as the entire process can be optimized simultaneously, it does not allow for much flexibility. In general, MEM devices do not require as advanced fabrication processes as those used in the IC industry and thus, a better approach is to post-process CMOS/bi-polar wafers, using an additional MEMS module. Not only does this increase process flexibility, since the active electronics can be upgraded to newer technologies as they become available, but this method does not require IC foundries to modify any of their existing and well established process flows.

The fabrication process described in this work has been specifically tailored to build high-quality RF beam resonators; it uses a metallized silicon carbide structural layer in conjunction with a thin polyimide sacrificial layer. Polyimide is an organic polymer which is readily etched using dry methods and thus, stiction is not an issue during the release step [32]. All interconnects are fabricated from sputtered aluminum, and isolation from the substrate is accomplished using a 2.5μm silicon oxide layer. The complete fabrication process does not include any steps at temperatures higher than 300°C, and is suitable for integration with active electronics.

The following is a summary of the research contributions of this thesis:

1) A thorough discussion on the operation and modeling of MEM resonators is provided, including several new derivations for model parameters that take into account mode and electrode shape. Several important properties of these devices are also addressed, such as non-linearity and temperature stability;

2) Development of a complete low-temperature, low-stress, silicon carbide-based fabrication process that has been optimized for building flexural-mode resonators;

3) Optimization of low-temperature deposition and etching processes for silicon carbide, polyimide, chrome and aluminum;

4) Design and testing of several novel flexural-mode resonator structures that include electrode shaping for mode selection and integrated thermal heaters for frequency tuning;

5) Design of a custom-built vacuum test system and methodology for measuring the Q-factor of MEM resonators at pressures as low as 10mTorr.

1.5 THESIS ORGANIZATION

This thesis consists of five chapters. The first chapter provides an overview of the current state of research for the design and fabrication of RF-MEM resonators, and discusses the motivation for developing such devices. It also includes a brief summary of the research contributions of this thesis.

Chapter 2 provides a detailed discussion of the theory of operation of MEM resonators and modeling. It describes a suitable lumped-element model that can be used to simulate the small-signal operation of these devices, and addresses important issues such as thermal stability, noise and non-linear operation.

Chapter 3 describes the development of a complete, low-temperature surface-micromachining process that has been developed for fabricating high-Q integrated MEM resonators. Each of the major device layers are treated in sequence, including the structural, metallization, and sacrificial layers. For each material, the development of etching and

deposition recipes are provided along with a discussion of some of the difficulties encountered. This chapter concludes with a detailed summary of the overall process.

Chapter 4 provides a description of the RF MEM resonator designs that have been fabricated using this process, and presents measured test results. Comparison of these results is also performed with the theory that has been established in Chapter 2, and describes potential reasons for the observed deviations. A description of the custom-built vacuum system and test methodology is also provided.

Lastly, chapter 5 summarizes the results of this work and presents possibilities for future improvement.

1.6 REFERENCES

[1] C. T. Nguyen, "Vibrating RF MEMS overview: applications to wireless communications," *Proceedings, Photonics West: MOEMS-MEMS 2005*, San Jose, California, Paper No. 5715-201, Jan. 22-27, 2005.

[2] *International Crystal Manufacturing Co. Inc.*, Catalog, Available at: http://www.icfmg.com

[3] C. T. Nguyen, "Transceiver front-end architectures using vibrating micromechanical signal processors (invited)," *Dig. of Papers, Topical Meeting on Silicon Monolithic Integrated Circuits in RF Systems,* pp. 23-32, Sept. 2001.

[4] P. J. French, "Development of surface micromachining techniques compatible with on-chip electronics," *J. Micromech. Microeng.*, vol. 6, pp. 197-211, 1996.

[5] C. T. Nguyen and R. T. Howe, "An integrated CMOS micromechanical resonator high-Q oscillator," *IEEE Journal of Solid-State Circuits*, vol. 34 (4), pp. 440-455, Apr. 1999.

[6] F. D. Bannon *et. al.*, "High-Q HF microelectromechanical filters," *Journal of Solid-State Circuits*, vol. 35, no. 4, pp. 512-526, April 2000.

[7] K. Wang *et. al.*, "VHF free-free beam high-Q micromechanical resonators," *IEEE Journal of Microelectromechanical Systems*, vol. 9, no. 3, pp. 347-360, Sept. 2000.

[8] K. Wang et. al., "High-order micromechanical electronic filters," *Proceedings of the 1997 IEEE International Micro Electro Mechanical Systems Workshop*, pp. 25-30, Jan. 1997.

[9] M. U. Demirci *et. al.*, "Higher-mode free-free beam micromechanical resonators," *2003 IEEE International Frequency Control Symposium*, pp. 810-818, May 2003.

[10] M. Abdelmoneum *et. al.*, "Stemless wine-glass-mode disk micromechanical resonators," *IEEE 16th Annual Conference on Micro Electro Mechanical Systems, 2003 (MEMS '03)*, pp. 698-701, Jan. 2003.

[11] J. Clark *et. al.*, "High-Q VHF micromechanical contour-mode disk resonators," *International Electron Devices Meeting, IEDM 2000*, pp. 493-496, Dec. 2000.

[12] J. Wang *et. al.*, "1.14-GHz self-aligned vibrating micromechanical disk resonator," *IEEE Radio Frequency Integrated Circuits (RFIC) Symposium*, pp. 335-338, June 2003.

[13] J. M. Bustillo *et. al.*, "Process technology for modular integration of CMOS and polysilicon microstructures," *Microsystems Technology*, vol. 1, pp. 30-41, 1994.

[14] W. Kuehnel *et. al.*, "A surface micromachined silicon accelerometer with on-chip detection circuitry," *Sensors and Actuators A*, vol. 45 (1), pp. 7-16, 1994.

[15] S.-S. Li, *et. al.*, "Micromechanical hollow-disk ring resonators," *Proceedings of the 17th IEEE Micro Electro Mechanical Systems Conf.*, Maastricht, The Netherlands, pp. 821-824, Jan. 2004.

[16] S.-S. Li, *et. al.*, "Bridged micromechanical filters," *Proceedings of the IEEE Conf. on Ultrasonics, Ferroelectrics, and Freq. Control*, Montreal, Canada, pp. 144-150, Aug. 2004.

[17] M. U. Demirci, *et. al.*, "Mechanically corner-coupled square μresonator array for reduced series motional resistance," *Dig. of Tech. Papers, Transducers '03*, Boston, MA, pp. 955-958, June 2003.

[18] M. U. Demirci, *et. al.*, "A low impedance VHF micromechanical filter using coupled-array composite resonators," *Dig. of Tech. Papers, Transducers '05*, Seoul, Korea, June 2005.

[19] S.-S. Li, *et. al.*, "Small percent bandwidth design of a 423-MHz notch-coupled micromechanical mixler," *Proceedings of the IEEE Ultrasonics Symposium*, pp. 1295-1298, Sept. 2005.

[20] Y.-W. Lin *et. al.*, "Low phase noise array-composite micromechanical wine-glass disk oscillators," *Technical Digest of the IEEE Electron Devices Mtg.*, Washington, DC, pp. 287-290, Dec. 2005.

[21] S.-S. Li, *et. al.*, "Self-switching vibrating micromechanical filter bank," *Proceedings of the IEEE Frequency Control/Precision Time and Time Interval Symposium*, Vancouver, Canada, pp. 135-141, Aug. 2005.

[22] A.-C. Wong *et. al.*, "Micromechanical mixer-filters ("Mixlers")," *IEEE J. Microelectromech. Syst.*, vol. 13 (1), pp. 100-112, Feb. 2004.

[23] W. Y. Ali-Ahmad, " RF system issues related to CDMA receiver specifications," *RF Design*, pp. 22-32, Sept. 1999.

[24] W.-T. Hsu *et. al.,* "A programmable MEMS FSK transmitter," 2006 IEEE *International Solid-State Circuits Conference (ISSCC 2006)*, Digest of Technical Papers, pp. 290-291, Feb. 2006.

[25] B. Antkowiak *et. al.*, "Design of a high-Q, low-impedance, GHz-range piezoelectric MEMS resonator," *the 12th International Conference on Solid State Sensors, Actuators and Microsystems (Transducers '03),* pp. 841-846, June 2003.

[26] B. Otis *et. al.*, "A 300-μW 1.9-GHz CMOS oscillator utilizing micromachined resonators," *IEEE Journal of Solid-State Circuits*, vol. 38, no. 7, pp. 1271-1274, July 2003.

[27] A. P. S. Khanna *et. al.*, "A 2GHz voltage tunable FBAR oscillator," *the 2003 International Microwave Symposium Digest*, vol. 2, pp. 717-720, June 2003.

[28] J. Clark *et. al.*, "High-Q VHF micromechanical contour-mode disk resonators," *International Electron Devices Meeting, IEDM 2000*, pp. 493-496, Dec. 2000.

[29] J. Wang *et. al.*, "1.51-GHz nanocrystalline diamond micromechanical disk resonator with material-mismatched isolating support," *IEEE 17th Annual Conference on Micro Electro Mechanical Systems, 2004 (MEMS '04)*, pp. 641-644, Jan. 2004.

[30] T.-C. Nguyens. *Micromechanical Signal Processesors*. Ph.D. Thesis Dissertation, Berkely,1994.

[31] B. Bircumshaw et. al., "The radial bulk annular resonator: Towards a 50Ω RF MEMS filter," *the 12th International Conference on Solid State Sensors, Actuators and Microsystems (Transducers '03)*, pp. 875-878, June 2003.

[32] N. Tas *et. al.*, "Stiction in surface micromachining," *J. Micromech. Microeng.*, vol. 6, pp. 385-397, 1996.

Chapter 2 Resonator Theory of Operation and Modeling

MEM resonators operate as micro-transducers that convert signals from the electrical to mechanical domain and vice versa. Thus, a suitable model is required that can be used to both analyze their mechanical and electrical properties simultaneously. Practical implementations involving MEM resonators often include circuits that are used to process both the input and output electrical signals of the device, and thus it is also important that these models be easily incorporated into conventional circuit simulation software. Presently, the number of available software packages that can be used to analyze micro-electro-mechanical systems are few, and are mostly focused on the mechanical properties of these devices. Some of the more commonly used software packages include Ansys [1], Intellisuite [2], MEMSPro [3], and Coventerware [4]. With these packages, however, RF electrical parameters are generally difficult, if not impossible, to obtain. Similarly, integration with common IC simulation suites such as Cadence [5] is usually not directly supported. As a result, the easiest way to simulate RF systems that include MEM resonators is to first use these packages to extract the mechanical properties of the devices, and then construct a general *behavioral model* based on the basic governing equations that can be incorporated into a circuit simulation package. Since the form of the differential equations governing linear RLC circuits are identical to those that describe the linear motion of mass-spring-damper systems, the mechanical properties of MEM resonators can be modeled using an equivalent combination of passive electrical components. If mechanical non-linearities are ignored, the mechanical device can be replaced with this equivalent lumped-model and easily incorporated into any circuit simulation software package. These models must capture both the mechanical properties of the device such as its resonant frequencies and the effects of viscous damping, along with the capacitive transduction that converts the input from an electrical signal to a mechanical force.

This chapter begins with an analysis of transverse vibration in MEM resonators, and develops a suitable lumped-element model which captures both the electrical transduction and mechanical properties of MEM resonators. The effect of resonator non-linearity on performance is also addressed along with a brief discussion on the temperature stability of MEM resonators.

2.1 MODAL ANALYSIS OF MEM RESONATORS

The resonators considered in this work can be modeled as simple composite beams with supports at both ends, as shown in Figure 2-1. The core material is SiC which acts as the structural layer, while on the top and bottom are thin layers of metal which are used to improve conductivity. In general, there are an infinite number of modes in which this structure can vibrate since it is a distributed-parameter system; however, with careful design, the desired modes can be isolated, while many of the spurious modes can be reduced or even completely eliminated. The two main types of vibrations that have been utilized for MEM resonators are the bulk-mode that involves the expansion and contraction of the entire volume of the structure, and the flexural-mode where the beam displaces in a direction perpendicular to its length. Although flexural-mode vibration has a lower frequency, it is commonly used since this mode can be easily excited. The bulk-mode, which has a much higher frequency and less energy loss, is generally more difficult to excite, and micromachined structures must employ very small lateral gaps that require specialized fabrication processes [6]. As a result, this work focuses on the flexural-mode beam resonators.

The resonant frequencies of a given structure can be found by solving the governing equations of motion. In its most general form, it is a complex partial differential equation with four degrees of freedom: three spatial (x, y, z) and time. By applying specific boundary conditions and solving this partial differential equation, the vibration shape and modes can be determined analytically.

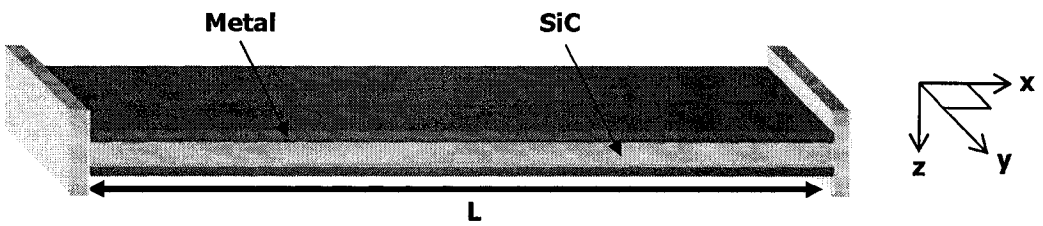

Figure 2-1: Simple composite beam anchored at both ends

In the case of a beam, the differential equation that describes transverse (flexural) vibration can be shown to be [7]

$$\bar{D}\frac{\partial^4 w(x,t)}{\partial x^4} - \bar{N}\frac{\partial^2 w(x,t)}{\partial x^2} + \bar{m}\frac{\partial^2 w(x,t)}{\partial t^2} + \bar{c}\frac{\partial w(x,t)}{\partial t} = q(x,t) \qquad \text{Eq. (2.1)}$$

where, $w(x,t)$ is the displacement of the beam in the z-direction at any position x at time t, $\bar{D}$ is the effective stiffness of the beam, $\bar{N}$ is the axial force along the length of the beam, $\bar{m}$ is the effective mass per unit length, $\bar{c}$ is the effective damping and $q(x,t)$ is a function that describes the external distributed load along the length of the beam. Note that, to a first order, the width of the beam does not have any effect on the transverse vibration of the resonator. The stiffness, effective axial force and distributed mass of the beam further depend on the shape of its cross-section and its material properties. In the case of beams that are composed of more than one material in different layers, the stiffness and equivalent Young's modulus will depend on the relative location and volume fraction of each of the different layers in the composite beam and can be calculated as [8],

$$\bar{D} = \sum_{i=1}^{N} E_i I_i \qquad \text{Eq. (2.2)}$$

$$\bar{m} = \sum_{i=1}^{N} \rho_i A_i \qquad \text{Eq. (2.3)}$$

where E_i is the Young's modulus of layer i, I_i is the second moment of area, ρ_i is the density, and A_i is the cross-sectional area. Thus, when the beam is a composite of several different materials, its effective stiffness and mass will become a combined function of the properties of all the materials. In the case of wide beams which have a width much greater than its thickness ($W > 10t$), the Young's modulus in Eq. (2.2) should be replaced by its effective value, $E/(1-\nu^2)$ [9], where υ is the Poisson ratio.

Similarly, the effective axial stress in the beam will be related to the intrinsic stress in each of the different material layers. The total axial force resulting from the residual stress in each layer of the composite can be approximated as

$$\bar{N} = \sum_{i=1}^{N} \sigma_i A_i \qquad \text{Eq. (2.4)}$$

where σ_i is the tensile residual stress in layer i (for compressive residual stress the sign of σ_i is negative). Residual stress from the fabrication process is usually unavoidable in surface micro-machining, and thus it is an important consideration when estimating the resonant frequency of the device.

In order to solve Eq. (2.1) and obtain an analytical expression for the amplitude of vibration of the MEM resonator, a separation of the time and displacement variables is required. From the *expansion theorem* in modal analysis [10], the overall displacement can be written as an infinite sum of its eigenfunctions as,

$$w(x,t) = \sum_{i=1}^{\infty} X_i(x) T_i(t) \qquad \text{Eq. (2.5)}$$

where $X_i(x)$ are the *normalized mode-shapes* of the system which are only functions of position, and $T_i(t)$ are functions of time which are called the *principle co-ordinates* [7]. The mode-shapes represent the relative displacement of the beam in the transverse direction when it is vibrating at one of its natural frequencies, while the time function indicates the temporal response of each mode to a given forcing function. This separation of variables allows the time and space variables to be decoupled and solved separately using standard techniques.

Assuming the beam vibrates in one of its natural modes, the deflection will vary harmonically with time as

$$\tilde{w}(x,t) = X_i(x)\tilde{T}e^{j\omega t} \qquad \text{Eq. (2.6)}$$

where $\tilde{T}$ is a complex variable representing the amplitude and phase of the principle co-ordinates. Substituting Eq. (2.6) into the un-damped ($\bar{c} = 0$), homogeneous form ($q(x,t)=0$) of Eq. (2.1) yields an expression for the mode-shapes that is independent of time (all terms dependent on time can be factored out):

$$\bar{D}\frac{d^4X_i}{dx^4} - \bar{N}\frac{d^2X_i}{dx^2} - \bar{m}\omega^2 X_i = 0\,. \qquad \text{Eq. (2.7)}$$

This ordinary differential equation can be easily solved with standard techniques, and provides an analytical expression for the relative deflection of the MEM resonator when it is vibrating in one of its modes, X_i.

A solution to Eq. (2.7) can be found by considering the boundary conditions imposed at the ends of the beam. In the case of a *clamped-clamped* beam (Figure 2-1) where its ends are fixed, both the displacement and its derivative are zero at the ends of the beam. Mathematically, these boundary conditions can be expressed as

$$X_i(x)\big|_{x=0} = 0, \quad \left.\frac{dX_i(x)}{dx}\right|_{x=0} = 0, \quad X_i(x)\big|_{x=L} = 0, \quad \left.\frac{dX_i(x)}{dx}\right|_{x=L} = 0 \qquad \text{Eq. (2.8)}$$

where L is the length of the beam. Using these boundary conditions to solve Eq. (2.7) an analytical expression for the mode-shape can be shown to be [11]

$$X_i(x) = A\left[\cos(\lambda x) - \cosh(\mu x) + \Gamma(L)\cdot\left(\sin(\lambda x) - \frac{\lambda}{\mu}\sinh(\mu x)\right)\right] \qquad \text{Eq. (2.9)}$$

where A is an arbitrary constant and Γ, λ, and μ are constants that depend on the mode number and beam properties and are given by

$$\Gamma(L) = \frac{\cos(\lambda L) - \cosh(\mu L)}{\frac{\lambda}{\mu}\sinh(\mu L) - \sin(\lambda L)} \quad \text{Eq. (2.10)}$$

$$\lambda = k\left[\sqrt{a^2+1} - a\right]^{1/2} \quad \text{Eq. (2.11)}$$

$$\mu = k\left[\sqrt{a^2+1} + a\right]^{1/2} \quad \text{Eq. (2.12)}$$

where,

$$a = \frac{\bar{N}}{2\bar{D}k^2} \quad \text{Eq. (2.13)}$$

$$k^4 = \frac{\bar{m}}{\bar{D}}\omega^2. \quad \text{Eq. (2.14)}$$

Note that Eq. (2.9) reduces to the more commonly cited beam equation [12] if the residual stress in the beam is assumed to be equal to zero. In this case, the equation for the mode-shape becomes

$$X_i(x) = A\left[\cos(kx) - \cosh(kx) + \Gamma(L)\cdot\left(\sin(kx) - \sinh(kx)\right)\right] \quad \text{Eq. (2.15)}$$

where,

$$\Gamma(L) = \frac{\cos(kL) - \cosh(kL)}{\sinh(kL) - \sin(kL)}. \quad \text{Eq. (2.16)}$$

Each of the mode-shapes calculated with Eq. (2.9) or Eq. (2.15) will also have an associated resonant frequency. When designing MEM resonators, this is one of the most important design parameters, since these natural frequencies will determine the pass-band of a MEM resonator. Depending on the application, any of these resonant modes can be used to filter electrical signals; however, the amplitude of the other modes must be minimized in order to eliminate leakage at unwanted frequencies. The resonant frequency associated with each mode-shape can be found by solving the characteristic equation of the system and is given by

$$\cos(\lambda L)\cosh(\mu L) - \frac{1}{2}\left(\frac{\mu}{\lambda} - \frac{\lambda}{\mu}\right)\sin(\lambda L)\sinh(\mu L) = 1 \ . \qquad \text{Eq. (2.17)}$$

Unfortunately, an exact, closed-form expression for the resonant frequency as a function of the beam parameters cannot be obtained because of the transcendental nature of this equation. Approximate solutions, however, can be found using the Rayleigh energy method [11] as,

$$\omega_i(\bar{N}) \approx \frac{\alpha_i^2}{L^2}\sqrt{\frac{\bar{D}}{\bar{m}}}\cdot\left(1+\gamma_i\frac{\bar{N}L^2}{12\bar{D}}\right)^{1/2} \qquad \text{Eq. (2.18)}$$

where γ_i, and α_i are constants that depend on the mode-number, and mode-shape. Values of these constants for the first five resonant modes are summarized below in Table 2-1 and can be calculated using the formulas derived in [11].

Table 2-1: Resonant frequency constants for a clamped-clamped beam

Mode Number	α_i	γ_i
1	4.7300	0.2949
2	7.8532	0.1453
3	10.9956	0.08117
4	14.1371	0.05155
5	17.2788	0.03555

As shown in Eq. (2.18), a tensile axial force (N positive) tends to increase the resonant frequency, while a compressive force (N negative) tends to reduce it. Using this property it is possible to tune the resonant frequency of the beam by externally applying an axial force. This can be accomplished in several different ways for a beam resonator. One possible method is to add a heater to the beam which not only lowers the effective Young's modulus, but will also introduce a compressive stress due to thermal expansion.

The resonant frequency of the composite beam in Figure 2-1 is plotted in Figure 2-2 for several different values of the beam length. For this plot, the core material was assumed to be 2μm thick amorphous SiC (*E=275GPa*), while the upper and lower layers are assumed to be 0.25μm thick aluminum (*E=75GPa*).

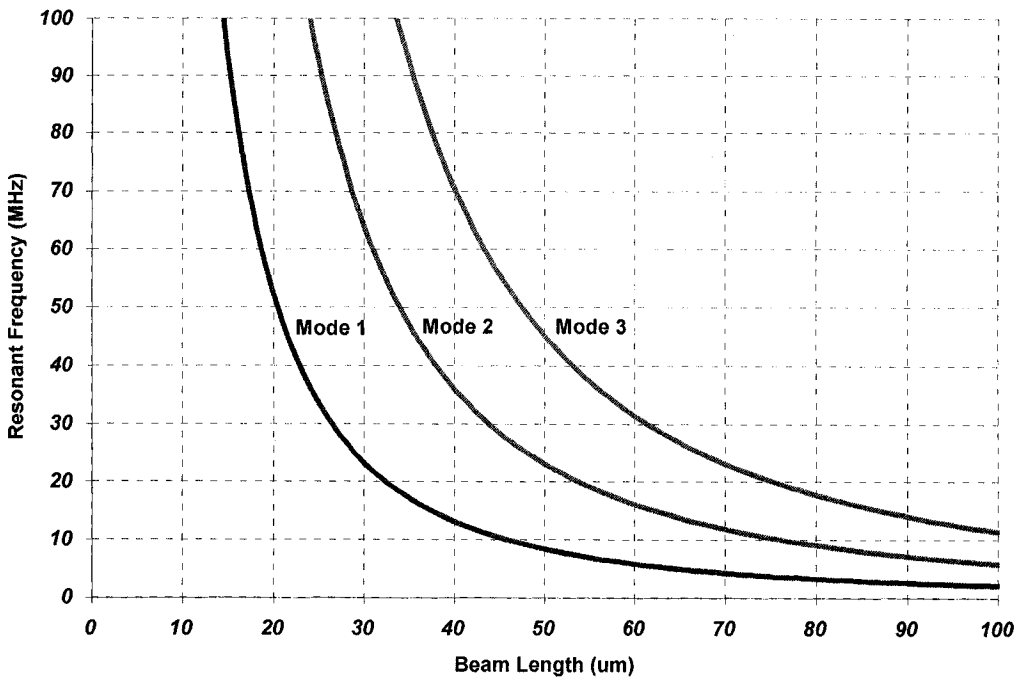

Figure 2-2: Resonant frequency of a clamped-clamped beam of different lengths

As expected, the resonant frequency decreases with increasing beam length. Plots of the first three associated mode-shapes, calculated using Eq. (2.9) are shown in Figure 2-3. In these cases, the axial stress was assumed to be zero in order to simplify the calculation. As shown in Figure 2-3 when the beam vibrates in its fundamental mode (Mode 1) all points of the beam move in phase, while for all other higher-order modes, parts of the beam vibrate out of phase with each other. This property can be advantageous when using MEM resonators in fully differential systems where electrical signals are either 90° or 180° out of phase. By using multiple electrodes under the length of the beam for different phases, higher-order resonant modes of the beam can be excited and used to filter differential signals [13].

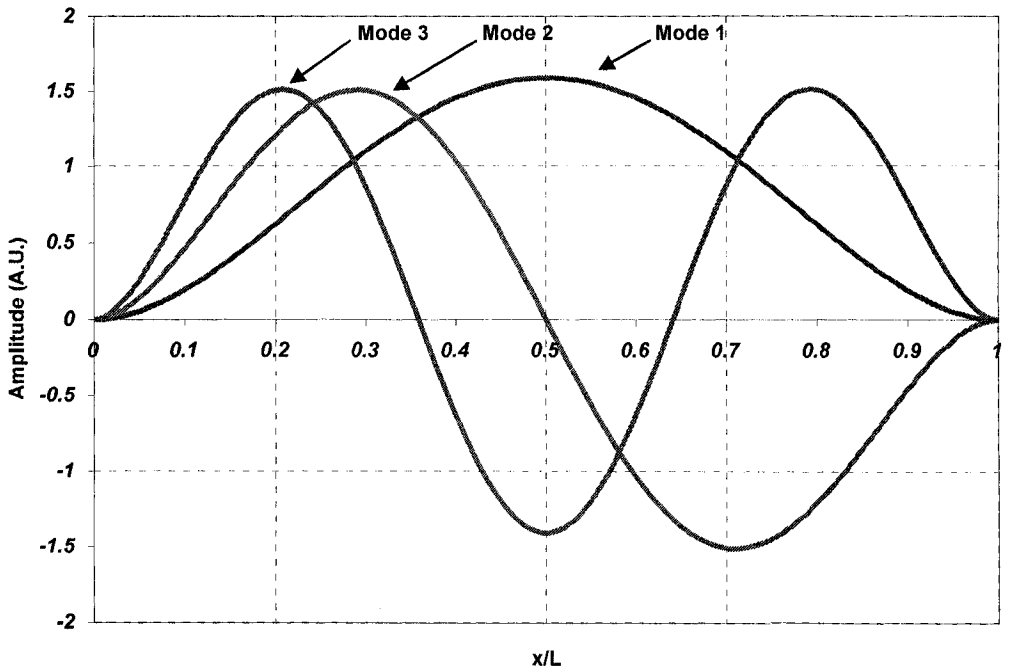

Figure 2-3: First three mode-shapes of a clamped-clamped beam

2.2 QUALITY FACTOR

The Q-factor of a filter is a metric that characterizes its level of selectivity in the frequency domain and is defined as

$$Q = \frac{\omega_o}{\Delta\omega_{-3db}} \qquad \text{Eq. (2.19)}$$

where $\Delta\omega_{-3db}$ is the -3dB bandwidth, and ω_o is the center frequency of resonance, both in radians ($\omega=2\pi f$). A linear system with a high-Q has a high selectivity, and thus has a very narrow bandwidth. On the other hand, a system with a low Q has a very large bandwidth and thus, acts as a wide-band filter. In terms of physical quantities, the Q-factor is also equal to the amount of energy stored in the system divided by the amount of energy that is lost per cycle,

$$Q = \frac{\Delta E_{stored}}{\Delta E_{lost}} \qquad \text{Eq. (2.20)}$$

Thus, to maximize the Q-factor energy, all sources of energy loss must be minimized (e.g. damping).

The resonance of a MEM device also has an associated Q-factor. In general, mechanical resonance has a very high level of selectivity (high-Q) due to the low level of intrinsic damping, and is therefore ideal for narrow-band filtering applications. In the case of a mechanical resonator, maximizing the Q of the device is synonymous with increasing the stiffness (stored energy) and minimizing energy loss (damping). When MEM resonators are used as the tank in a reference oscillator, the Q-factor has a large impact on the phase-noise performance of the system, and therefore should be as large as possible [15]-[16].

The main sources of energy loss in MEM resonators are through viscous gas-damping, thermo-elastic damping, and the radiation of acoustic waves through the supports.

2.2.1 Gas Damping

Gas-damping can be reduced by operating the resonator in a vacuum. For high-performance devices this is becoming the norm, as it is the only way to obtain relatively high-Q values (>10000) [13]. For reasonable performance, devices should be operated at pressures that are less than ~100mTorr [17].

2.2.2 Anchor Loss

Significant energy loss also occurs through the anchors of the resonators. Since the MEM resonator must be affixed to the substrate in some way, this type of loss in unavoidable. As the beam vibrates, it generates a periodic force on the supports that are fixed to the substrate. This force, in turn, generates acoustic waves and radiates energy into the substrate. Although design techniques exist to minimize this loss, such as locating the supports at stationary nodal points [14], alignment errors and fabrication tolerances ultimately limit the effectiveness of these methods.

2.2.3 Thermo-elastic damping

The last major source of energy loss in MEM resonators is due to thermo-elastic damping, which is a characteristic of the resonator material and cannot be avoided. As a result, it sets the upper thermodynamic limit on the Q-factor [18]. It is essentially the conversion of mechanical strain into heat, which then leads to entropic dissipation. Local adiabatic changes in the stress state result in temperature increases and therefore, the conduction of heat through the material. As shown in [18]-[19], there are three components to this damping in polycrystalline materials: Zener damping (discussed on next page), inter-crystalline damping, and intra-crystalline damping. Each type of loss contributes to the overall Q of the system, and is given by,

$$Q_{\text{total}}^{-1} = Q_{\text{Zener}}^{-1} + Q_{\text{inter}}^{-1} + Q_{\text{intra}}^{-1} \,. \qquad \text{Eq. (2.21)}$$

The most important property of each one of these three types of thermo-elastic damping mechanisms is that the loss is maximized at certain frequencies of vibration. Thus, this should be a major consideration for design, since resonators that vibrate near these frequencies will be less efficient. The critical resonant frequency where thermo-elastic damping is maximum is related to the physical properties of the beam and is given by [18],

$$f_d = \psi \frac{\kappa}{\rho C_p L^2} = \frac{1}{\tau_d} \qquad \text{Eq. (2.22)}$$

where L is the characteristic dimension, ρ is the density, κ is the thermal conductivity, C_p is the specific heat of the material, and ψ is a proportionality constant of order unity that is related to the temperature profile . The Q^{-1} due to thermoelastic damping is commonly approximated with a Lorentzian, and depends on the operating frequency of the device as,

$$Q^{-1} = \Delta \frac{\omega\tau_d}{1+(\omega\tau_d)^2} \qquad \text{Eq. (2.23)}$$

where,

$$\Delta = \frac{\alpha^2 TE}{\rho C_p} \qquad \text{Eq. (2.24)}$$

where α is the coefficient of thermal expansion, T is the absolute equilibrium temperature of the beam, E is the Young's modulus. From Eq. (2.23) it can be shown that at the characteristic damping frequency, the Q reaches a minimum value of $\Delta/2$. To calculate the total Q factor, the associated constants must be calculated for the assumed temperature distribution in the resonator.

As a flexural-mode resonator vibrates, the top and bottom surfaces will periodically be cycled from tensile to compressive stress. When the material is under tensile stress, the material cools slightly, while when under compressive stress it heats up. This creates a temperature gradient across the cross-section of the beam that leads to irreversible heat flow. If the temperature profile across the beam cross-section is approximated as sinusoidal, as is the case in a flexural mode resonator, ψ is equal to $\pi/2$ [18]. The resulting time-constant, is therefore given by,

$$\tau_{zener} = \frac{\rho C_p h^2}{\kappa \pi^2} \qquad \text{Eq. (2.25)}$$

where h is the characteristic dimension. In the case of a flexural mode beam, this is equal to the beam thickness. It is important to note that the conductivity in the material is strongly dependant on the size and type of its grain structure; for example, the conductivity of a material with columnar grains will be different from that of a fine-grained material. This type of damping is referred to as Zener damping and is the dominant form of damping in low frequency resonators (<100MHz).

Intra-crystalline damping is related to the conduction of heat inside the grains of the material and occurs on a relatively short time-scale. The corresponding frequency is related to the average grain size, d, and is given by [18],

$$\tau_{\text{intra}} = \frac{\rho C_p d^2}{\kappa_{SC} \pi^2} \qquad \text{Eq. (2.26)}$$

where κ_{SC} is the single-crystal value of the thermal conductivity. Note that, in this case, the thermal conductivity is equal to the single-crystal value and not the bulk poly-crystalline value. This equation is valid as long as the characteristic dimension is much larger than the average grain size.

Lastly, inter-crystalline damping is due to the conduction of heat between adjacent grains. The time-constant for this mode of loss was shown by Zener to be equal to [18],

$$\tau_{\text{inter}} = \frac{\rho C_p d^2}{3\pi^2 \kappa_{poly}} \cong \frac{5}{3}\tau_{\text{intra}} \qquad \text{Eq. (2.27)}$$

By combining these three losses as shown in Eq. (2.21), a maximum value for the Q factor at different frequencies can be determined. Srikar et. al. [18] showed that for a poly-crystalline beam resonator with a thickness of 2μm and an average grain size of 100nm, the characteristic damping frequencies where the Zener, intracrystalline, and intercrystalline loss are maximum occur at 7.1MHz, 14.1GHz and 8.5GHz, respectively.

For the case of amorphous SiC, only Zener damping will be present since the material is not polycrystalline. Using the property values for Hexalloy SiC given in Table 2-2 [20], the peak thermo-elastic damping a 2μm thick flexural mode resonator can be calculated with Eq. (2.25) to be approximately ***23MHz***.

Table 2-2: Properties of Hexoloy SiC

Property	Value
Density [kg / m^3]	3000
Thermal Conductivity [W / m^3 °K]	118
Specific Heat [J / kg °K]	670

2.2.4 Q-loading by external circuitry

The energy loss mechanisms described in sections 2.2.1 to 2.2.3 are responsible for determining the *unloaded* Q-factor of the resonator; however, when it is used in a system

with external circuitry, the effective Q-factor of the resonator will in fact be much lower due to loading from these external components. Consider the situation shown in Figure 2-4, where the terminals of the resonator are connected to external circuitry with output and input resistances equal to R_o and R_i, respectively.

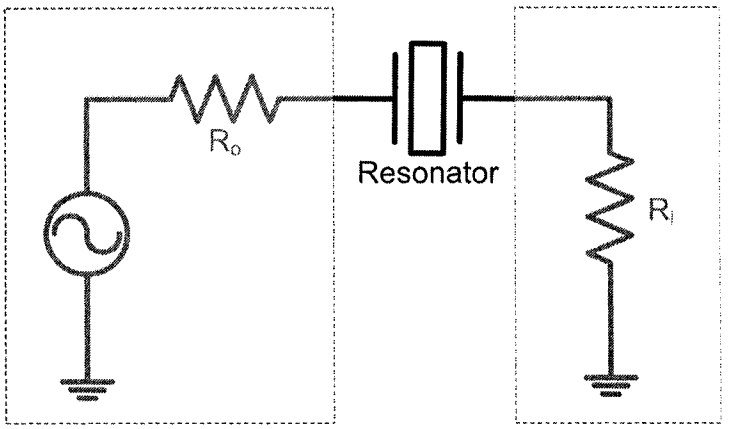

Figure 2-4: Resistive loading on resonator by external circuitry

At resonance, the losses in the resonator can be modeled by a simple resistor, and therefore the unloaded Q factor of the resonator is proportional to

$$Q_{ul} \propto \frac{1}{R_x} \qquad \text{Eq. (2.28)}$$

where R_x is called the equivalent resistance of the resonator. When connected to external circuitry, however, the input and output resistances load the device and add directly to the loss in the resonator loop. Thus, the effective Q-factor of the resonator becomes inversely proportional to the *total* losses in the loop and can be expressed as

$$Q_l \propto \frac{1}{R_o + R_x + R_i} \qquad \text{Eq. (2.29)}$$

where Q_l is the loaded Q-factor of the resonator. Combining Eq. (2.28) and Eq. (2.29), yields the following useful relation:

$$Q_l = \frac{Q_{ul}}{1+\left(\frac{R_i + R_o}{R_x}\right)} \qquad \text{Eq. (2.30)}$$

Therefore, the effective Q-factor of the overall system will be reduced when loaded by the output and input impedances of the external circuitry. As a result, the input and output resistances of circuitry connected to the resonator should be made as small as possible to reduce this loading effect and maintain the high-Q provided by the resonator.

2.3 SMALL-SIGNAL RESONATOR MODEL

In general, the differential equations that model MEM resonators are highly non-linear, and obtaining closed form solutions for their behavior is usually impossible in most cases. For small deflections of the beam, however, the system can be considered linear and analyzed using the techniques outlined in section 2.1. Since MEM resonators convert signals from the electrical to mechanical domain, a small-signal model is required that can capture the mechanical resonance of the device along with various electrical effects such as capacitive feed-through and resistive loading by external circuitry. The following section describes how the mechanical resonator can be modeled using a combination of passive electrical components. Using this approach, these models can then be easily incorporated into circuit simulation packages where they can be analyzed in conjunction with external circuitry.

2.3.1 Mechanical modeling of MEM resonators

Many analogies can be drawn between mechanical and electrical systems [21]. Since both can be modeled using linear system theory, all concepts and design techniques that are used for circuit design can be used for mechanical design, as well. This simplifies the design procedures since techniques and tools for designing circuits are readily available and well developed. Like electric circuits, the response of mechanical systems can be described in terms of the poles and zeros of the system's Laplace transform transfer function. In fact, the linear differential equations that govern the motion of lumped parameter mechanical systems

take the same general form of a resonant RLC circuit. To more clearly see the similarity between the two systems, consider the governing equations of a series RLC circuit and those of the lumped mass-spring-damper mechanical system shown below.

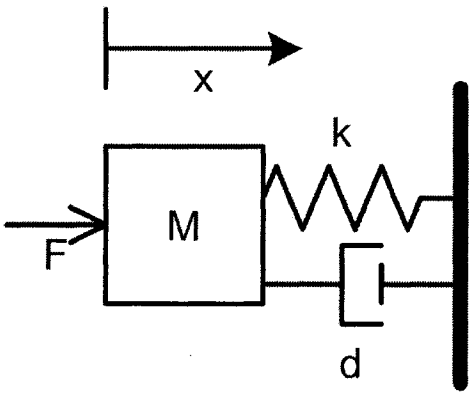

Figure 2-5: Lumped spring-mass-damper system

Using phasor notation, the voltage-current (V-I) response of a series electrical RLC circuit can be described as,

$$\tilde{V} = j\omega L\tilde{I} + \frac{1}{j\omega C}\tilde{I} + R\tilde{I} \qquad \text{Eq. (2.31)}$$

while the response of a mechanical system consisting of a single mass, spring and damper can be expressed as,

$$F = j\omega M\dot{x} + \frac{K}{j\omega}\dot{x} + D\dot{x} \qquad \text{Eq. (2.32)}$$

where x is the displacement amplitude, K is the stiffness of the lumped-element mechanical system, M is the equivalent mass, and D is the damping. Note that, if current is equated to velocity and voltage equated to force, there is a clear similarity between the two equations. By inspection, the mass is seen to be equivalent to inductance, the spring constant equal to the inverse of capacitance, and the damping equal to the resistance. An RLC circuit is shown in Figure 2-6 along with its mechanical equivalent system.

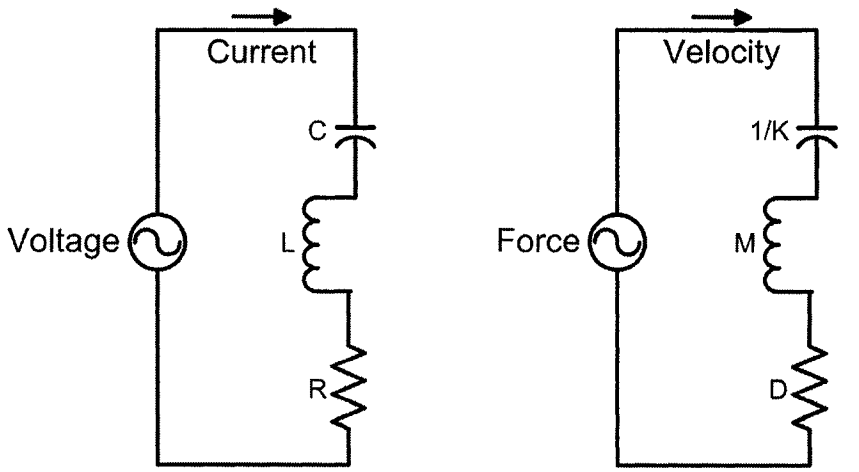

Figure 2-6: Series RLC analogy

Similarly, a parallel model can be derived if current is equated with force and voltage equated with velocity. In this case, the mass is equivalent to inductance, the spring constant equal to the inverse of capacitance, and the damping equal to the resistance, as shown below.

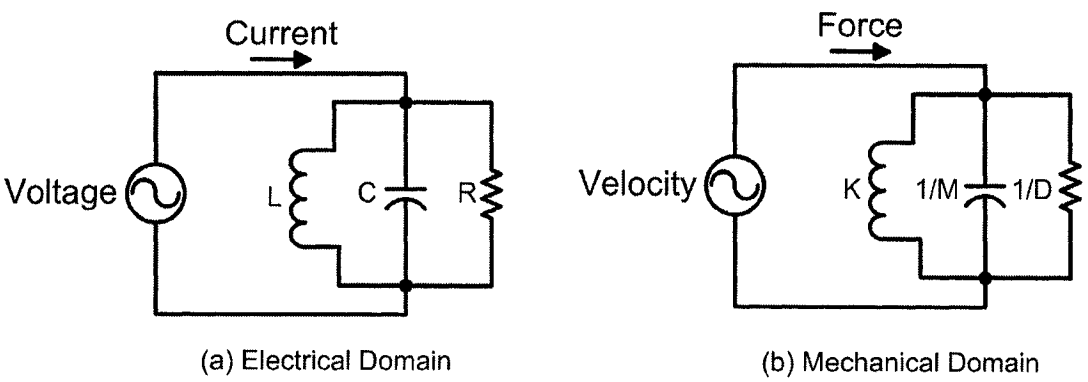

Figure 2-7: Parallel RLC analogy

Both of the above analogies are numerically equivalent and will produce the same results when used for design. The choice of which to use remains left to the designer and will depend on the application. A summary of the correspondence between the electrical and mechanical domains, for both analogies, is provided in Table 2-3.

Table 2-3: Summary of electrical - mechanical analogy

Electrical Variable	Mechanical Variable (series analogy)	Mechanical Variable (parallel analogy)
Voltage (V)	Force (F)	Velocity (v)
Current (I)	Velocity (v)	Force (F)
Inductance (L)	Mass (m)	Compliance (1/k)
Capacitance (C)	Compliance (1/k)	Mass (m)
Resistance (R)	Damping (d)	Damping^{-1} (1/d)

Using the series analogy, the mechanical impedance of the device can be defined as [21]

$$Z_m = \frac{\dot{X}}{F} . \qquad \text{Eq. (2.33)}$$

This impedance, called the mobility, is the ratio of the velocity of the structure *at a certain location* to the driving force. Note that, for distributed structures such as MEM resonators, the impedance will change depending on the location at which it is calculated; for example, at a nodal point where the velocity is always zero, the impedance will also be zero. Similarly, the mechanical impedance of a free-end would be infinite, while the impedance of a clamped end (i.e. anchor) would be zero. Using this impedance analogy, it is easy to derive the response of several coupled mechanical systems by simply combining their mechanical impedances in the correct manner (i.e. series impedances add, while parallel impedances combine in the same way as electrical resistors). This makes it much easier to analyze the effect of the support structure on the resonator or other coupled resonators.

Although a lumped-element mass-spring-damper mechanical model can be used to describe a single resonance peak, most mechanical structures contain an infinite number of modes, and thus a more complex model is required [21]. As is commonly known, the response of a linear system can be broken down into the sum of a number of second-order responses using partial fraction expansion techniques. The total impedance of such a system becomes the sum of the impedances corresponding to each of the different modes. This is equivalent to modeling

each resonant mode with a mass-spring-damper sub-system. The total output response is then the sum of the responses of each of these sub-systems.

The response of a second order mechanical system can be described by its Laplace transform,

$$\frac{W(s)}{F(s)} = \frac{\omega_r^2 / k}{s^2 + \frac{\omega_r}{Q} s + \omega_r^2} \qquad \text{Eq. (2.34)}$$

where $W(s)$ is the displacement of the mass, Q is the Q-factor of the mechanical resonance and k is the mechanical spring constant. Using the definition of the mechanical impedance and substituting $s = j\omega$ in the above equation, the frequency response of the driving point mobility of a single mode can be shown to be,

$$Z_i = \frac{j\omega}{m_i} \frac{1}{\left(\omega_{ni}^2 - \omega^2 + j \frac{\omega \cdot \omega_{ni}}{Q_i} \right)} \qquad \text{Eq. (2.35)}$$

where Q_i is the Q-factor of the mechanical response for a particular mode, and m_i is the equivalent mass of that mode.

The regular mass of a structure cannot be used in these models, however, since most resonant structures that are of interest to MEMS designers have complex mode shapes. This fact becomes extremely important when dealing with resonators that commonly utilize higher-order and bulk acoustic modes. The resonant structure must be treated as a distributed system, with an *effective* mass and *effective* modal force. This generalized mass is usually some fraction of the actual mass of the system and is *dependant on the mode-shape* [7].

The generalized mass for a given mode is found by substituting the equation for the displacement of the resonator (Eq. (2.5)) back into the original equation of motion (Eq. (2.1)) and isolating for the terms that are only dependent on time. After some manipulation, this yields the following set of differential equations (one for each mode),

$$\sum_{i=1}^{\infty} X_i \left(\bar{m} \frac{d^2 T_i}{dt^2} + \bar{c} \frac{dT_i}{dt} + \bar{m}\omega^2 T_i \right) = q \ . \qquad \text{Eq. (2.36)}$$

To isolate for one specific mode, N, this equation can be multiplied by the corresponding mode shape and integrated from one end of the beam to the other. Using the fact that different mode-shapes are orthogonal and that the value of their inner product is zero (see section 2.4), this equation reduces to

$$\underbrace{\int_0^L X_N^2 dx}_{\substack{\text{mode-shape} \\ \text{dependent} \\ \text{constant}}} \left(\bar{m} \frac{d^2 T_N}{dt^2} + \bar{c} \frac{dT_N}{dt} + \bar{m}\omega^2 T_N \right) = \underbrace{\int_0^L X_N q dx}_{\text{effective modal force}} \ . \qquad \text{Eq. (2.37)}$$

This second-order ordinary differential equation describes the time response of the beam for mode number N. As seen above, the response of a single mode reduces to a simple second-order differential equation. In this case, the generalized mass that can be used to model the response of this mode is given by

$$m_N = \int_0^L \bar{m} X_N^2 dx \ . \qquad \text{Eq. (2.38)}$$

Similarly, as shown in Eq. (2.37), the equivalent force that excites mode N is given by

$$F_N = \int_0^L X_N \cdot q \cdot dx \ . \qquad \text{Eq. (2.39)}$$

This result shows that the equivalent force which excites each mode is actually a scaled function of q that depends on the mode-shape. Thus, depending on the distribution of the forcing load, different modes will be emphasized while others will be suppressed.

Using this equivalent mass, the equivalent spring constant can also be determined as,

$$k_N = \omega_r^2 m_N \ . \qquad \text{Eq. (2.40)}$$

Similarly, the damping co-efficient can also be determined from the Q-factor of the particular mode,

$$d_N = \frac{m_N \omega_r}{Q} . \qquad \text{Eq. (2.41)}$$

Using this lumped-element approximation, the behavior of the resonator and its interaction with the support structure can be easily analyzed. Although this method will not be as accurate as finite-element modeling, it still provides great insight into the factors that affect the resonant modes of the structure and the effect of losses on the resonator.

2.3.2 Capacitive transduction and sensing

MEM resonators exploit the high-Q resonance of mechanical structures to perform highly selective filtering for applications in RF-analog electronics. The resonance action is similar to that used in quartz crystals; the electrical signal is first transformed into a mechanical force that causes the mechanical structure to vibrate at select frequencies. With careful design, the vibrating structure can be used to output an electric current that is a filtered version of the input signal. Thus, the filtering process is composed of three main steps: electro-mechanical transduction to convert the input signal to a mechanical force, high-Q filtering using mechanical resonance, and lastly, mechanical-electrical conversion to create an output current. In quartz crystals, these actions are performed using the piezoelectric property of the material; however, in most MEM resonators the electro-mechanical transduction is performed using electrostatic (capacitive) actuation. Consider the simple beam resonator shown in Figure 2-8. It is composed of a single mechanical beam with a length L and a width W which acts as both the top electrode and resonant structure. The bottom electrode is located under the beam at a distance g_o and is connected to the input signal.

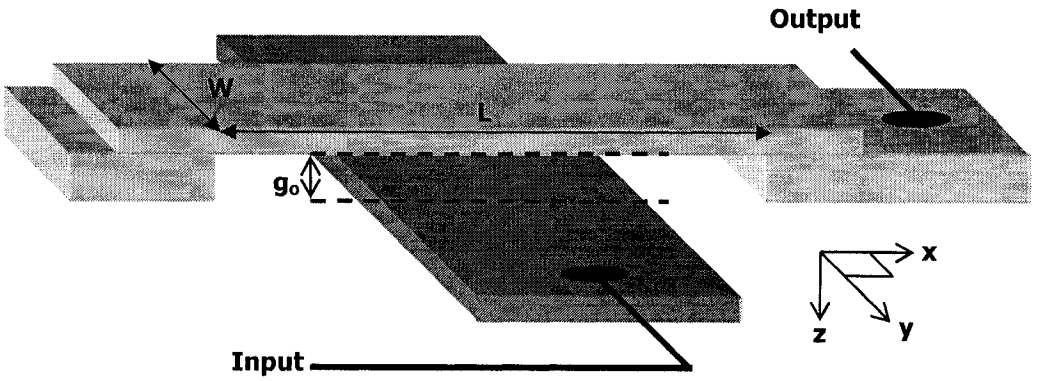

Figure 2-8: Simplified beam resonator

When a DC voltage is applied between the input electrode and the resonator, an electrostatic force is developed according to,

$$F = \frac{\delta E}{\delta g} \qquad \text{Eq. (2.42)}$$

where E is the electrostatic energy stored in the gap capacitance and g is the gap size. Neglecting fringing capacitances, this force can be expanded to,

$$F = \frac{\delta(0.5CV^2)}{\delta g} = \frac{1}{2}\frac{\delta C}{\delta g}V^2 + V\cancel{\frac{\delta V}{\delta g}}C \qquad \text{Eq. (2.43)}$$

When a small-signal voltage is superimposed on the input electrode, the driving force becomes,

$$F = \frac{1}{2}\frac{\delta C}{\delta g}\left(V_p + v_i\right)^2 = \underbrace{\frac{1}{2}\frac{\delta C}{\delta g}V_p^2}_{\text{DC Force}} + \underbrace{\frac{\delta C}{\delta g}V_p v_i + \frac{1}{2}\frac{\delta C}{\delta g}v_i^2}_{\text{AC Force}}. \qquad \text{Eq. (2.44)}$$

where V_p is the DC voltage across the gap and v_i is the small-signal input voltage. Thus, the total force on the beam will consist of a DC term that depends only on the bias voltage, and an AC term that depends on the amplitude of excitation. Assuming a sinusoidal input signal of $|v_i|\cos(\omega_i t)$, the force becomes,

$$F = \underbrace{\frac{1}{2}\frac{\delta C}{\delta g}V_p^{\,2} + \frac{1}{4}\frac{\delta C}{\delta g}|v_i|^2}_{\text{DC Force}} + \underbrace{\frac{\delta C}{\delta g}V_p|v_i|\cos(\omega_i t) + \frac{1}{4}\frac{\delta C}{\delta g}|v_i|^2\cos(2\omega_i t)}_{\text{AC Force}} \qquad \text{Eq. (2.45)}$$

Note that, because of the second-order non-linearity, there is now an AC term at twice the input frequency. Since the signal input amplitude is small, however, the last term in both the AC and DC signals in this equation can be neglected. Furthermore, since the Q factor of the mechanical resonance is high, and thus the resonant peak is very narrow, the signal at twice the input frequency will have very little effect on the output. Therefore, the input signal voltage will be converted into a mechanical force that is proportional to the input signal magnitude and at the same frequency:

$$F_i \cong V_p \frac{\delta C}{\delta g} v_i \,. \qquad \text{Eq. (2.46)}$$

This force will cause the mechanical structure to vibrate, which will in turn modulate the size of the gap between the two electrodes. Since the resonator is designed to have a specific dominant resonant mode, the structure will only vibrate with significant amplitude if the input signal frequency matches this mode. If a DC voltage is placed across the gap, the time varying capacitance will generate an output current. This current is proportional to the speed of vibration and has a magnitude of,

$$i = \frac{\delta Q}{\delta t} = \frac{\delta(CV_p)}{\delta t} = V_p \frac{\delta C}{\delta t} = V_p \frac{\delta C}{\delta g}\frac{\delta g}{\delta t} \qquad \text{Eq. (2.47)}$$

where Q here denotes the electrical charge (not the Q-factor). By convention, a positive current is defined as flowing out of the resonator.

The mechanisms described above form the basis of capacitive transduction in MEM resonators. The original input electrical signal first creates a proportional time-varying force on the beam. If this force is at the same frequency of one of the beam's natural modes, it will begin to vibrate. As a result of the vibration, the size of the gap is modulated at the input frequency, which in turn creates an output electrical current. Thus, the input signal is converted from the electrical domain to the mechanical domain where it is filtered by the

high-Q resonator, and then back to the electrical domain where it can be processed by other circuitry.

The amount of modulation of the capacitive gap depends on the amplitude of vibration and is given by

$$g(t) = g_o + W_{\max} \sin(\omega_i t) \qquad \text{Eq. (2.48)}$$

where W_{max} is the maximum amplitude of vibration, and g_o is the mean gap size. The magnitude of the output current can therefore be related to the maximum vibration amplitude as,

$$i = V_p \frac{\delta C}{\delta g} \omega |W_{\max}| \cos(\omega_i t) \qquad \text{Eq. (2.49)}$$

This important result indicates that the magnitude of the output current is directly related to the amplitude of vibration, and thus the latter must be made as large as possible to increase the power of the output signal. This is extremely important when MEM resonators are used in reference oscillators, since the phase-noise of the system is inversely related to the output power [15][22].

2.3.3 Small-signal electrical model

In order to derive a suitable small signal model that takes into account both the mechanical and electrical properties of the resonator described thus far, first we consider the complete transfer function of the resonator rewritten in the frequency domain,

$$\frac{I_o(\omega)}{V_i(\omega)} = \frac{F(\omega)}{V_i(\omega)} \frac{W(\omega)}{F(\omega)} \frac{I_o(\omega)}{W(\omega)} = Y_r(\omega) \qquad \text{Eq. (2.50)}$$

where $Y_r(\omega)$ is the effective electrical admittance of the resonator. Note that it depends on three separate transfer functions: 1) the capacitive transduction of the resonator input voltage to an applied force, $F(\omega)/V_i(\omega)$, 2) the conversion of the force to mechanical vibration,

$W(\omega)/F_i(\omega)$ and lastly, 3) the generation of the output current by modulation of the gap size, $I_o(\omega)/W(\omega)$.

The middle term in Eq. (2.50) is dependent on the geometric dimensions of the resonator and can be designed using the techniques summarized in section 2.1. The other two terms involve the conversion of electrical and mechanical signals, and depend on both the shape of the electrode and the mode-shape of resonance. As discussed in section 2.3.2, the conversion of a small-signal input voltage to a mechanical force can be approximated as,

$$F_i \cong V_p \frac{\delta C}{\delta g} v_i \,. \qquad \text{Eq. (2.51)}$$

Since the beam has a static deflection due to the applied DC bias, the gap distance cannot be considered constant across the length of the beam. Thus, the differential force per unit length of the beam is given by,

$$dF(x) = V_p \cdot \frac{\varepsilon W_e(x) dx}{g(x)^2} v_i(t) \qquad \text{Eq. (2.52)}$$

where $g(x)$ is the input gap distance at location x, $W_e(x)$ is the electrode width which is now assumed to be a function of the location on the beam, $v_i(t)$ is the small signal input voltage and $dF(x)$ is the differential force per unit length. This differential force along with all other differential parameters, are illustrated in Figure 2-9.

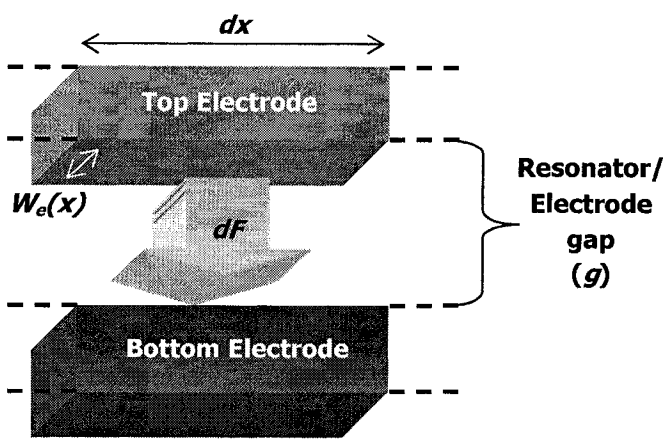

Figure 2-9: Resonator differential input force

The bias voltage across the resonator/electrode gap creates a time-varying force that is approximately proportional to the input signal voltage. To find the value of the transfer-function for an input voltage to a mechanical force for a *specific mode*, the generalized modal force must be used for the small signal-model. Thus, the input force must be transformed according to Eq. (2.39), and for mode number N is given by,

$$F_N(t) = v_i(t) \cdot \int_{L_{e1}}^{L_{e2}} \varepsilon V_p \frac{X_N(x) W_e(x)}{g(x)^2} dx = \eta_i v_i(t) \qquad \text{Eq. (2.53)}$$

where L_{e1} and L_{e2} indicate the locations of the edges of the electrode, and η_i is the effective electro-mechanical coupling co-efficient at the input. The change in integration bounds takes into account the fact that $W_e(x)=0$ outside of the range $[L_{e1},L_{e2}]$.

Similarly, the value of the transfer function which describes the conversion of the mechanical vibration into an output current must also be found using integration. The differential form of the output current of a beam resonator is given by

$$di = V_p \frac{\varepsilon W_e(x) dx}{g(x)^2} \frac{\delta w(x,t)}{\delta t} . \qquad \text{Eq. (2.54)}$$

The total output current is found by integrating this equation from L_{e1} to L_{e2}. Expressed in the frequency domain, this equation becomes,

$$I_o(\omega) = \int_{L_{e1}}^{L_{e2}} di = \int_{L_{e1}}^{L_{e2}} V_p \frac{\varepsilon W_e(x) X_N(x)}{g(x)^2} j\omega T_N(\omega) dx = \eta_o j\omega T_N(\omega) \qquad \text{Eq. (2.55)}$$

where $T_N(\omega)$ is the time function in the modal expansion of the displacement response given in Eq. (2.5), and η_o is the effective electro-mechanical coupling co-efficient at the output. In the case of a beam resonator, the input and output electromechanical coupling coefficients are equal and therefore,

$$\eta_o = \eta_i = \eta = \int_{L_{e1}}^{L_{e2}} V_p \frac{\varepsilon W_e(x) X_N(x)}{g(x)^2} dx . \qquad \text{Eq. (2.56)}$$

The equivalent small-signal electrical admittance for a MEM resonator can now be found by substituting Eq. (2.53), Eq. (2.55) and Eq. (2.34) into Eq. (2.50) which yields,

$$Y_r(\omega) = \frac{I_o(\omega)}{V_i(\omega)} = \eta^2 \frac{j\omega}{m_N} \frac{1}{\left(\omega_{ni}^2 - \omega^2 + j\frac{\omega \cdot \omega_{ni}}{Q}\right)} \qquad \text{Eq. (2.57)}$$

where m_N is the *generalized* mass for mode number N, and Q is the Q-factor. Note that, at resonance the current is in phase with the input voltage. At this frequency, the electrical impedance has a magnitude of,

$$\frac{V_i}{I_o} = \frac{m_N \omega_r}{\eta^2 Q} = R_x \,. \qquad \text{Eq. (2.58)}$$

In this equation, R_x is the equivalent motional resistance of the resonator and is a very important design parameter. As was discussed earlier, the motional resistance should be as low as possible to both minimize noise and extra circuitry requirements. Neglecting static deflection of the beam, and assuming rectangular electrodes of constant width, the motional resistance of the resonator can be approximated as

$$R_{x,beam} = \frac{k_N g_0^4}{\omega_r Q V_p^2 W_r^2 \varepsilon^2 \left(\int_{L_{e1}}^{L_{e2}} X_N(x)dx\right)^2} \propto \frac{k_N g_0^4}{\varepsilon^2 \omega_r Q V_p^2 A_e^2} \qquad \text{Eq. (2.59)}$$

where k_N is the effective spring constant of the resonant mode. This equation indicates that the motional resistance of the resonator is directly related to the fourth power of the gap size, and inversely related to the square of the electrode and bias voltage. Therefore, to achieve a low R_X it is very important to make the gap size as small as possible.

For the purposes of electrical design, it is convenient to model the mechanical resonator as a series RLC circuit, where the values of the components are given in Table 2-3. From the effective resonator impedance in equation Eq. (2.57), the equivalent capacitance and inductance can be determined to be,

$$C_x = \frac{\eta^2}{k_N} \qquad \text{Eq. (2.60)}$$

$$L_x = \frac{m_N}{\eta^2} \qquad \text{Eq. (2.61)}$$

This derivation assumes that one mode can be considered dominant; however, it is easy to include several other modes by adding their corresponding *equivalent* impedances in parallel. Note that, since the applied force will be different for each one of the different mode-shapes, the input and output electromechanical transduction co-efficients (η) will be different.

With these equivalent circuit parameters, it is easy to construct an equivalent electrical circuit model. The one most commonly used for a two port resonator is shown below [24].

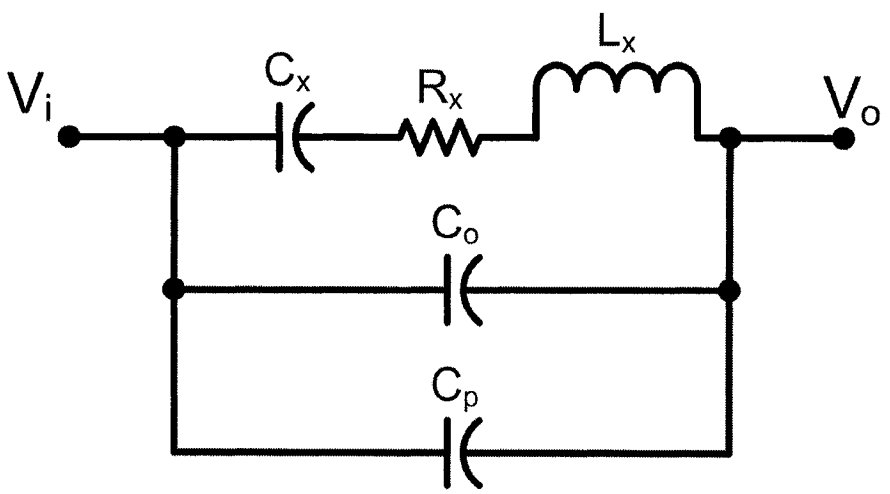

Figure 2-10: Resonator small signal electrical model

In this figure, the resonator is represented by its equivalent RLC circuit, while the overlap capacitance and parasitic feed-through capacitance are modeled with C_o and C_p, respectively. The static electrical overlap capacitance of the resonator input and output port is given by

$$C_o = \frac{\varepsilon L_e W_e}{g_0} \qquad \text{Eq. (2.62)}$$

where L_e and W_e are the length and width of the resonator's electrode, respectively. The parasitic feed-though capacitance from the input to the output port is represented by C_p and depends on the level of coupling between the two ports of the device. It is mainly a result of feed-through the substrate and coupling through the resonator's packaging and fixturing.

2.4 SELECTIVE EXCITATION OF BEAM RESONATORS

Since MEM resonators are usually designed for use at one specific frequency, higher resonant modes can be problematic; for example, if they are used as filters, these spurious peaks in the frequency response will create unwanted pass-bands at higher frequencies. As will be shown in the ensuing section, the size of these other resonant peaks can be reduced with careful design of both the drive and sense electrodes [25].

Distributed vibrating structures have an infinite number of mode-shapes that are characterized by their eigenfunctions. One important characteristic of these mode-shapes is that they form an orthogonal vector space. Thus, for any mode-shape, X_i, the following is true [7],

$$\begin{cases} \int_L X_i X_j dx = \alpha_{ij} & i = j \\ \int_L X_i X_j dx = 0 & i \neq j \end{cases} \qquad \text{Eq. (2.63)}$$

where α_{ij} is an arbitrary constant and L is the length of the resonator. Although not readily apparent, this important property can be utilized to design electrodes that excite and sense only *one* (or more) resonant mode(s).

In problems involving forced vibration, it is also often convenient to express the eigenfunctions of the system in terms of an orthonormal set. In this case, the inner product of any two functions in the set will be equal to unity. Thus, for any normalized mode-shape, X_i, the following will be true,

$$\begin{cases} \int_L X_i X_j dx = 1 & i = j \\ \int_L X_i X_j dx = 0 & i \neq j \end{cases} \qquad \text{Eq. (2.64)}$$

Normalization can be done by simply using the inverse form of Eq. (2.63). Using this technique, values for the constant A in the beam mode-shape equations given in Eq. (2.9) and Eq. (2.15) can be found; for example, consider the generalized mode-shape equation $A_i X_i$, where A_j is the arbitrary constant shown in Eq. (2.9). Substituting this function in for X_i and X_j in equation Eq. (2.64) yields,

$$A_i^2 \iint_A X_i X_i dA = A_i^2 \alpha_i = 1 \quad . \qquad \text{Eq. (2.65)}$$

Using this condition, the arbitrary constants of the mode-shape can be eliminated by substituting,

$$A_i = \sqrt{\frac{1}{\alpha_i}} \quad . \qquad \text{Eq. (2.66)}$$

If the arbitrary constants of the system's eigenfunctions are replaced with this form, the inner product between any two orthogonal functions in the set will be zero, while the inner product of any eigenfunction with itself will be unity.

To see how this property of mode-shapes can be used to selectively excite different modes, consider Eq. (2.53), which describes the electromechanical coupling factor for mode i, rewritten as

$$\eta_i = \frac{V_p \varepsilon}{g_0^2} \underbrace{\int_0^L W_e(x) X_i(x) dx}_{\text{scaling factor}} \quad . \qquad \text{Eq. (2.67)}$$

This equation indicates that the effective electromechanical coupling factor is proportional to the ***integral of the electrode shape function multiplied by the mode-shape.*** Thus, to eliminate unwanted spurious modes, the electrode shape can be chosen so that the scaling

factor in Eq. (2.67) is minimized for undesirable resonant modes. To effectively select only a single mode, the electrode thickness along the length of the resonator should be proportional to the desired mode's eigenfunction. Note that, if this is the case, these scaling factors will be zero for all modes *except* the one that is desired because of the orthogonal property of mode-shapes. Assuming that the electrode width function is proportional to the desired normalized eigenfunction with mode-number N, which can be expressed as

$$W_e(x) = W' X_N(x) \qquad \text{Eq. (2.68)}$$

where W' is an arbitrary constant, the equation for η reduces to

$$\begin{aligned} \eta_i &= \frac{V_p \varepsilon W'}{g_0^2} \int_0^L X_N^2(x)dx = \frac{V_p \varepsilon W'}{g_0^2}, && \text{desired mode, } i = N \\ \eta_i &= \frac{V_p \varepsilon W'}{g_0^2} \int_0^L X_N(x) X_i(x)dx = 0, && \text{all other modes, } i \neq N \end{aligned} \qquad \text{Eq. (2.69)}$$

Thus, if the resonator electrode width is shaped proportional to the desired mode-shape, all other spurious resonant peaks in the resonator transfer function are effectively eliminated.

Consider, for example, the simple beam resonator shown in Figure 2-11.

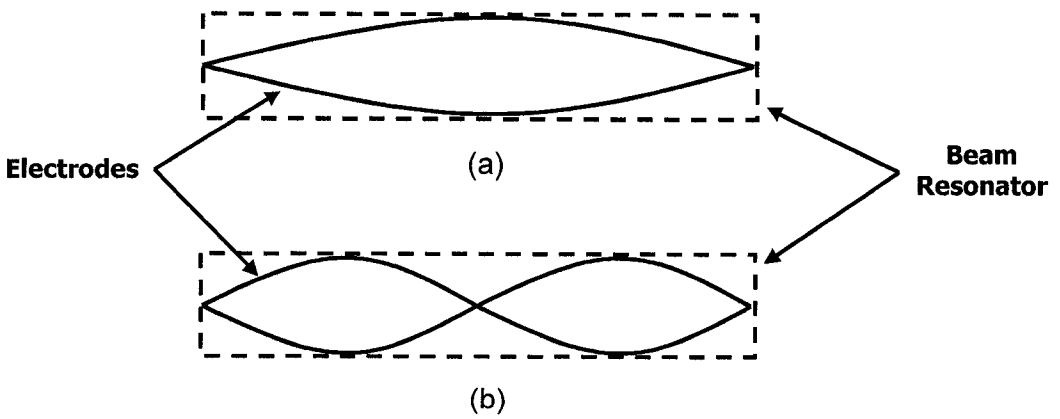

Figure 2-11: Beam resonator design for selective mode excitation; (a) first mode, (b) second mode

The thickness of the electrode in Figure 2-11a is designed to be proportional to the first mode-shape, while the electrode shape in Figure 2-11b is proportional to the second mode shape. Both of these configurations will effectively excite only the first and second mode respectively, since the value of the scaling factor in equation Eq. (2.67) will be zero for all other modes.

This important result shows that different resonant modes will be excited with forces of different magnitudes, and that the magnitude of this force is strongly dependant on the shape of the electrodes. Thus, with careful electrode design, the driving force for the desired resonant modes can be made greater than that for other undesired modes. This strategy, called selective mode excitation (SME) can be used to effectively eliminate resonant peaks at higher frequencies.

Electrode shaping can also be used at the sense electrode to only *detect* certain modes of vibration. Since the electromechanical coupling coefficient for the input and output of a beam resonator are identical, electrode shaping will also affect the output current of the resonator. This design strategy is called selective mode detection, or SMD, can be used to further filter the output current of the resonator and select only the desired modes.

2.5 NON-LINEARITY IN MEM RESONATORS

There are two main sources of non-linearity in MEM resonators: the gap capacitance used for electrostatic actuation, and material hardening. So far, all analyses reported have assumed small input signals, and thus the non-linearities could be ignored; however, as the amplitude of the input signal increases, the non-linear gap capacitance will create a significant number of harmonics in both the output current and input driving force. Not only do these non-linearities distort the output signal, but they also lead to more important effects such as resonant frequency pulling and pass-band distortion.

If the resonator electrodes have little static bending, the non-linear capacitance can be modeled using the simple parallel plate formula, which is given by,

$$C = \frac{\varepsilon A}{g_0 + x} \qquad \text{Eq. (2.70)}$$

where g_0 is the initial gap spacing, A is the electrode area, and x is the displacement of the gap. As shown previously, the input force and the output current of a resonator are directly related to the derivative of this gap capacitance which is given by,

$$\frac{\delta C}{\delta x} = -\frac{\varepsilon A}{g_o^{\,2}} \frac{1}{\left(1 + \frac{x}{g_o}\right)^2} = -\frac{C_o}{\left(1 + \frac{x}{g_o}\right)^2} \,. \qquad \text{Eq. (2.71)}$$

Note that the derivative of the capacitance has an inverse-square non-linearity that will create harmonics at multiples of the input frequency. Thus, at the output electrode, the current signal will have significant distortion when the signal amplitude becomes large. Although not readily apparent, this non-linearity is also directly responsible for the resonant frequency shift that occurs with changing the bias voltage and input amplitude. Both of these effects are described in more detail in the following sections.

2.5.1 Frequency Pulling

The frequency of a MEM resonator can be tuned to some degree by adjusting the bias voltage across both the input and output gap capacitances [26]. A positive increase in the bias voltage is accompanied by a negative shift in frequency. This effect, commonly referred to as 'spring softening,' allows the output frequency to be tuned; however, it also means that amplitude noise on the bias-voltage line will modulate the output frequency, creating close to carrier noise through AM to FM conversion. The resonant frequency will also change as the input amplitude grows, which can have a significant effect on the short-term, frequency stability of the resonator.

Frequency pulling is a result of the non-linear input, gap capacitance. To see this result, consider the effect of the input gap capacitance on electro-mechanical transduction [24]. As shown previously, the input force is directly related to the input voltage through the

derivative of the gap capacitance. This non-linear capacitance can be approximated using a simple series expansion as,

$$\frac{\delta C}{\delta x} = -C_o\left(1-\frac{2}{g_0}x+\frac{3}{g_0^2}x^2-\frac{4}{g_0^3}x^3+\ldots+\frac{n+1}{g_0^n}x^n\right)$$

where Eq. (2.72)

$$C_o = \frac{\varepsilon A}{g_0^2}$$

Inserting this series into the input force equation of the resonator results in,

$$F = -C_o\left(1-\frac{2}{g_0}x+\frac{3}{g_0^2}x^2-\frac{4}{g_0^3}x^3+\ldots+\frac{n+1}{g_0^n}x^n\right)\left(V_p - v_i\right)^2 \qquad \text{Eq. (2.73)}$$

At resonance, the input voltage can be replaced by $v_i = |v_i|\cos(\omega_r t)$ and the mechanical response can be replaced with $x = |x|\sin(\omega_r t)$ (quadrature shifted with respect to the input). Substituting, and keeping only the components that are at the input signal frequency, yields the force component [24],

$$F = C_o V_p |v_i|\cos(\omega_r t) + \left(\frac{C_o}{g_0}V_p{}^2 + \frac{C_o}{4g_0}|v_i|^2\right)|x_i|\sin(\omega_r t)\ . \qquad \text{Eq. (2.74)}$$

The first term is the input force due to the input voltage while the second term is proportional to the mechanical response of the system. Thus, the second term creates an effective electrical spring constant that will subtract from the mechanical spring constant. This can be seen by equating the input force with the mechanical differential equation of the system, and using Eq. (2.39) to find the effective modal force, as shown below:

$$m_N\ddot{x}(t) + c_N\dot{x}(t) + k_N x(t) = \int_{L_{e1}}^{L_{e2}} X_N(x)dx \cdot \left[\frac{\varepsilon W_r}{g_0^2}V_p|v_i|\cos(\omega_r t) + \left(\frac{\varepsilon W_r}{g_0^3}V_p{}^2 + \frac{\varepsilon W_r}{4g_0^3}|v_i|^2\right)\underbrace{|x_i|\sin(\omega_r t)}_{x(t)}\right]$$

Eq. (2.75)

Collecting like terms, and noting that $x(t) = |x|\sin(\omega_r t)$, the effective, first-order electrical spring constant can be extracted and is equal to

$$k_{e1} = \left(\frac{\varepsilon W_r}{g_0^3} V_p^{\,2} + \frac{\varepsilon W_r}{4 g_0^3} |v_i|^2 \right) \cdot \int_{L_{e1}}^{L_{e2}} X_N(x)dx \approx \frac{\varepsilon W_r}{g_0^3} V_p^{\,2} \cdot \int_{L_{e1}}^{L_{e2}} X_N(x)dx . \qquad \text{Eq. (2.76)}$$

Note that the electrical spring constant is proportional to the square of the bias voltage and inversely proportional to the cube of the gap capacitance. This dependence on the bias voltage can be used to tune the frequency of the resonator. Note that the electrical spring constant will subtract from the mechanical spring constant of the system and will therefore lower the resonant frequency according to,

$$f_r' = \sqrt{\frac{k_m - k_e}{m}} = f_r \sqrt{1 - \frac{1}{k_N} \frac{\varepsilon W_r V_p^{\,2}}{g_0^3} \int_{L_{e1}}^{L_{e2}} X_N(x)dx} . \qquad \text{Eq. (2.77)}$$

The above equation shows that the sensitivity of the resonator frequency to changes in the bias voltage can be increased by increasing the electrode area, decreasing the gap spacing and decreasing the mechanical spring constant. This indicates that for high-frequency resonators, where the spring constant is *very high*, the tuning range will be inherently small.

2.5.2 Material Hardening and higher-order spring constants

Another source of non-linearity is the material itself. When the vibration amplitude is large, the deformation of the resonator can no longer be described using Hooke's law. In the case of high-frequency resonators which have a very high mechanical stiffness, the capacitive non-linearity may no longer be dominant and the material non-linearity must be included. This material non-linearity can be described in terms of its stress-strain relationship [27],

$$T = E_1 S + E_3 S^3 + E_5 S^5 + \ldots \qquad \text{Eq. (2.78)}$$

where T is the stress in the material and S is the engineering strain. The stress is only composed of odd-ordered terms since, for most practical cases, the load-displacement curve is symmetric about the origin. Depending on the signs of the coefficients, the material can

begin to stiffen or soften as the strain increases; in these cases, it can no longer be considered linear. Including higher-order effects, the lumped-element stiffness of the mechanical system becomes,

$$k(x) = k_{m1} + k_{m3}x^2 + k_{m5}x^4 + .. \qquad \text{Eq. (2.79)}$$

Thus, the stiffness is now described with several coefficients that indicate the level of non-linearity. As the deformation increases, the effective spring constant will also change. The effect of spring softening and hardening are shown below on the corresponding force-displacement graphs.

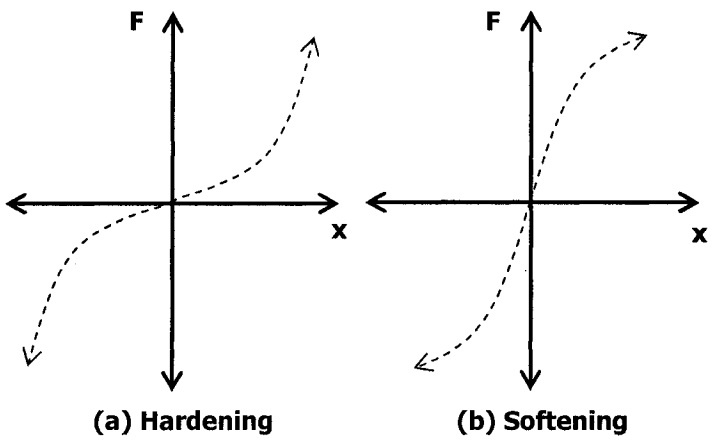

Figure 2-12: Material hardening and softening

Using a similar analysis to that done in the previous section, higher-order *electrical* spring constants (k_e) can also be shown to exist and are given by,

$$k_{e2} = -\frac{3}{2}\frac{\varepsilon A}{g_0^4}V_p^2 - \frac{3}{8}\frac{\varepsilon A}{g_0^4}|v_i|^2 \approx -\frac{3}{2}\frac{\varepsilon A}{g_0^4}V_p^2$$
$$k_{e3} = 2\frac{\varepsilon A}{g_0^5}V_p^2 - \frac{1}{2}\frac{\varepsilon A}{g_0^5}|v_i|^2 \approx 2\frac{\varepsilon A}{g_0^5}V_p^2 \qquad \text{Eq. (2.80)}$$
$$k_{e4} = -\frac{5}{2}\frac{\varepsilon A}{g_0^6}V_p^2 - \frac{5}{8}\frac{\varepsilon A}{g_0^6}|v_i|^2 \approx -\frac{5}{2}\frac{\varepsilon A}{g_0^6}V_p^2$$

These constants create a restoring force that is proportional to $x(t)$, $x(t)^2$, $x(t)^3$ etc., which subtracts from the mechanical spring constants and thus create a spring-softening effect. The total restoring force is therefore the sum of the mechanical spring hardening and electrical spring softening, and is given by

$$f_r = (k_{m1} - k_{e1})x + (-k_{e2})x^2 + (k_{m3} - k_{e3})x^3 + \ldots \qquad \text{Eq. (2.81)}$$

Using this form for stiffness, the equation of motion for the resonator in the case of free vibration becomes,

$$m\ddot{x} + c\dot{x} + k_1 x + k_2 x^2 + k_3 x^3 + \ldots = f_i$$

where,

$$\begin{aligned} k_1 &= k_{m1} - k_{e1} \\ k_2 &= -k_{e2} \\ k_3 &= k_{m3} - k_{e3} \\ k_4 &= -k_{e4} \\ &\ldots \end{aligned} \qquad \text{Eq. (2.82)}$$

This particular type of nonlinearity in the spring constant leads to the *"Duffing"* behavior [7][28] which results in a distortion of the resonator pass-band, and under extreme cases can result in erratic, unstable vibrations. The pass-band distortion that occurs with increasing vibration amplitude is shown below.

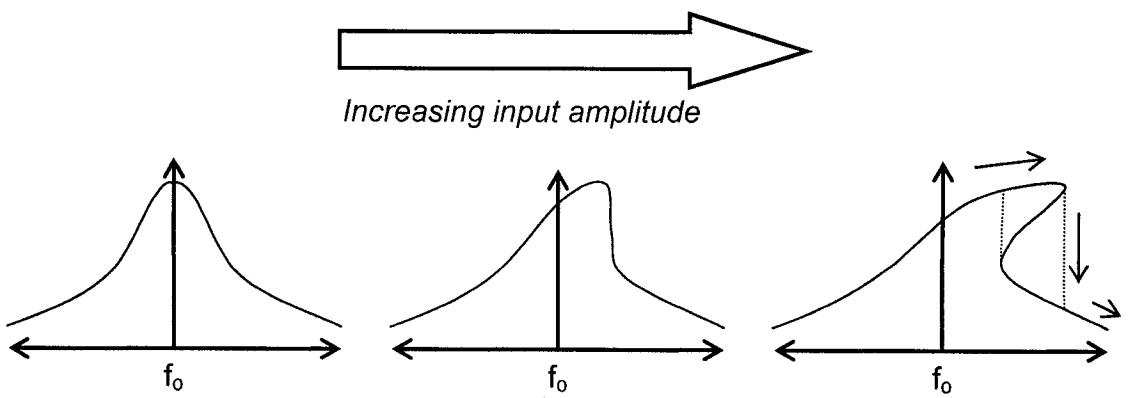

Figure 2-13: Duffing behavior

With this type of non-linearity, as the input amplitude increases the pass-band gets pulled to one side. The direction of the frequency spectrum distortion is dependant on whether spring-softening (electrical) or spring-hardening (mechanical) is the dominant non-linearity. If electrical spring softening is dominant, the resonance will shift to a lower frequency, and if spring-hardening is dominant the resonant frequency will increase. As shown in the last plot in Figure 2-13 where the oscillation amplitude is large, as the frequency increases a critical point is reached where there are ***three states*** at which the resonator can oscillate [28]. This phenomenon can lead to unstable vibrations where the amplitude can instantaneously jump-up or drop-down, resulting in an increase in the overall phase-noise of the system [29]. As the frequency is further increased, the signal amplitude will follow the lower part of the curve. As shown by Bogoliubov [30], the middle portion of this curve corresponds to an unstable mode of vibration, where any perturbation will cause the amplitude to jump to either the lower or upper portion of the frequency response. Conversely, if the frequency is swept from a higher frequency to a lower frequency, the amplitude response will first follow the lower part of the curve and then jump to the higher section.

In order to examine the effect of these higher-order capacitive and material non-linearities on the resonant frequency, first consider a more general form for the equation of motion for a second order mechanical system:

$$\ddot{x} + \frac{\dot{x}}{Qm} + \omega_r^2 f(x) = 0 \qquad \text{Eq. (2.83)}$$

where *f(x)* is the equation for the non-linear restoring force. Unfortunately, a general closed form expression for this differential equation does not exist; however, using some simplifications, the response of the system can be estimated using the *method of successive approximations* [7]. If the non-linearities in the system are comparatively small and the damping is low, the non-linear differential equation can be simplified to [7]

$$\ddot{x} + \omega_r^2 x + \frac{k_3}{m} x^3 = 0 \ . \qquad \text{Eq. (2.84)}$$

Using the method of successive approximations it can be shown that the resonant frequency of this system can be expressed as [7]

$$\omega'^2 = \omega_0^2 + \frac{3k_3}{4m} x_m^2 \qquad \text{Eq. (2.85)}$$

where ω' is the resonant frequency of the non-linear system, ω_0 is the resonant frequency of the system with all non-linearities ignored, and x_m is the amplitude of oscillation. This important result indicates that the resonant frequency is directly related to the square of the amplitude of vibration. Also, it is evident that the third order spring constant has an effect on the resonant frequency. Thus, if the MEM resonator is used in an oscillator, the resonant frequency will slowly increase as the output builds up.

2.6 TEMPERATURE STABILITY

The temperature stability of micro-resonators is another important performance metric that must be addressed. Of all the possible applications for MEM resonators, the reference oscillator is probably the hardest to realize because of its strict performance requirements, specifically the allowable frequency drift with temperature. In communications applications, oscillators have traditionally been implemented with quartz crystals which have excellent short and long-term stability; for example, a typical uncompensated AT-cut quartz crystal has a typical frequency drift of up to ±50ppm [31], over the temperature range -20°C to 100°C. Thus, in order to compete with these devices, the frequency drift of micro-resonators should be in the same order of magnitude.

The temperature dependence of the resonator frequency can be attributed to the temperature coefficient of the Young's modulus and the coefficients of thermal expansion of both the substrate and the resonator materials [32]. As the temperature increases, the Young's modulus decreases and thus, the resonant frequency goes down [33]. Similarly, changes in temperature also lead to thermal expansion. This increase in volume changes the dimensions of the device and therefore the resonant frequency. Also, when the rate of expansion of the

substrate is significantly different from that of the resonator material, large stresses can be generated. Whether this effect decreases or increases the frequency will depend on the resonator design.

Little work has been done on quantifying the temperature dependence of MEM resonators; however, some values are available. Recent publications have experimentally determined the frequency drift for a poly-silicon resonator to be -10ppm/°C [26], while other experiments of a poly-silicon resonator on Si have yielded a temperature co-efficient of -25ppm/°C [34]. Another experiment with SiC lateral resonators quoted a frequency dependence of -10ppm/°C [35]. Thus, in the worst case, there will be a frequency drift on the order of -2000ppm over the temperature range 20°C-80°C. It is difficult to generalize what the frequency drift will be, since different resonator designs will be affected differently; however, changes in resonance for most designs will still have the same order of magnitude.

For beam resonators, the resonant frequency is directly related to the acoustic velocity of the material and the characteristic dimension as

$$f_r \propto \frac{1}{L^2}\sqrt{\frac{E}{\rho}} \quad . \qquad \text{Eq. (2.86)}$$

By differentiating with respect to temperature, the fractional frequency shift can be shown to be,

$$\frac{(\delta f_r)/f_r}{\delta T} = TC_f = \frac{\alpha_E}{2} - 2\alpha_L \qquad \text{Eq. (2.87)}$$

where, α_E is the fractional change in Young's modulus per degree Celsius and α_L is the coefficient of thermal expansion.

Several approaches have been investigated in the literature to reduce the thermal dependence of MEM resonators and can be subdivided into three different techniques: geometrical stiffening, electrical stiffening, and the use of micro-ovens. Geometrical stiffening uses the thermal expansion of the material to generate tensile stresses in the material as the

temperature increases. These tensile forces counteract the decrease in Young's modulus and keep the resonant frequency constant [36]. Using this method, the dependence of the resonant frequency on temperature for a lateral, poly-silicon beam resonator was reduced from over -17ppm/°C, down to -2.5ppm/°C; a reduction of over 7X.

Electrical stiffening uses the tunable electrical spring constant to counteract the change in resonant frequency. By changing the bias voltage of the device the resonant frequency can also be changed to some degree. This method has been successfully applied in conjunction with a novel flexural-mode design to create a resonator with a temperature constant of less than -0.25ppm/°C [31].

Lastly, micro-ovens have been extensively used with quartz crystals to create ultra-stable reference oscillators that only vary from ±10ppm to ±0.5ppm over the entire -20°C to 80°C temperature range. The major disadvantage with this technique is the warm-up time required to reach the nominal operating temperature and the extra power required to run the heater [24]. This technique uses a temperature sensor to monitor the temperature inside the resonator package, and to adjust the power to a built-in heater to regulate the temperature. Using this method, Nguyen's designed a lateral resonator that had a frequency variation of less than 200ppm over the temperature range of 20°C to 100°C, while using less than 5mW of power [24].

2.7 REFERENCES

[1] *Ansys*, Ansys Inc., http://www.ansys.com/

[2] *Intellisuite*, Intellisense Software, http://intellisensesoftware.com/

[3] *MemsPro*, MemsCap, http://www.memscap.com/cad-memspro-ds.html/

[4] *Coventor Ware,* Coventer Inc., http://www.coventor.com/

[5] *Cadence,* Cadence Design Systems, http://www.cadence.com/

[6] E. Quevy *et. al.*, "Ultimate technology for micromachining of nanometric gap HF micromechanical resonators," *IEEE 16th Annual Conference on Micro Electro Mechanical Systems, 2003 (MEMS '03)*, pp. 157-160, Jan. 2003.

[7] S. P. Timoshenko *et. al.* Vibration Problems in Engineering, 5th ed. Wiley-Interscience, 1990.

[8] D. Herman *et al.*, "MEMS test structure for mechanical characterization of VLSI thin films," *Proceedings of the SEM Annual Conference & Exposition*, Portland Oregon, June 2001.

[9] A. C. Ugural *et. al.*, Advanced Strength and Applied Elasticity, 3rd ed., Prentice Hall, 1994.

[10] D. J. Inman, Engineering Vibration, 2nd ed., Prentice Hall, 2000.

[11] H. A. C. Tilmans *et. al.*, "Micro resonant force gauges," *Sensors and Actuators A*, no. 30, pp. 35-53, 1992.

[12] F. D. Bannon *et. al.*, "High-Q HF microelectromechanical filters," *IEEE Journal of Solid-State Circuits*, vol. 35, no. 4, pp. 512-526, April 2000.

[13] M. U. Demirci *et. al.*, "Higher-mode free-free beam micromechanical resonators," *2003 IEEE International Frequency Control Symposium*, pp. 810-818, May 2003.

[14] K. Wang *et. al.*, "VHF free-free beam high-Q micromechanical resonators," *IEEE Journal of Microelectromechanical Systems*, vol. 9, no. 3, pp. 347-360, Sept. 2000.

[15] S. Lee *et. al.*, "Mechanically-coupled micromechanical arrays for improved phase noise," *Proceedings, IEEE Int. Ultrasonics, Ferroelectrics and Frequency Control,* Montreal, Canada, pp. 280-286, Aug. 2004.

[16] V. Kaajakari *et. al.*, "Square-extensional mode single-crystal silicon micromechanical resonator for low-phase-noise oscillator applications," *IEEE Electron Device Letters*, vol. 25, no. 4, pp.173-175, April 2004.

[17] Y. T. Cheng *et. al.*, "Vacuum packaging technology using localized aluminum/silicon-to-glass bonding," *The 14th IEEE International Conference on Micro Electro Mechanical Systems, (MEMS 2001),* pp. 18-21, 21-25 Jan 2001.

[18] V. T. Srikar *et. al.*, "Thermoelastic damping in fine-grained polysilicon flexural beam resonators," *Journal of Microelectromechanical Systems*, vol. 11, no. 5, pp. 499-504, Oct. 2002.

[19] B. H. Houston *et. al.*, "Loss due to transverse thermoelastic currents in microscale resonators," *Materials Science and Engineering A,* vol. 370, pp. 407-411, 2004.

[20] *Hexoloy SG Silicon Carbide Datasheet*, Saint-Gobain Advanced Ceramics, http://www.hexoloy.com.

[21] R. A. Johnson. *Mechanical Filters in Electronics.* Wiley and Sons, 1983.

[22] D. B. Leeson, "A simple model of feedback oscillator noise spectrum," *Proc. IEEE,* vol. 54, pp.329-330, Feb. 1966.

[23] Y.-W. Lin *et. al.*, "Series resonant VHF micromechanical resonator reference oscillators," *IEEE Journal of Solid-State Circuits,* vol. 39, no. 12, pp. 2477-2491, Dec. 2004.

[24] T.-C. Nguyens. *Micromechanical Signal Processesors.* Ph. D. Thesis Dissertation, Berkely, 1994.

[25] A. Prak *et. al.,* "Selective mode excitation and detection of micromachined resonators," *Proceededing of the Conference on Micro Electro Mechanical Systems, 1992 (MEMS '92)*, pp. 220-225, Feb. 1992.

[26] C. T.-C. Nguyens *et. al.*, "An integrated CMOS micromechanical resonator high-Q oscillator," *IEEE Journal of Solid-State Circuits*, vol. 34, no. 4, pp. 440-455, April 1999.

[27] V. Kaajakari *et. al.*, "Non-linearities in single-crystal silicon micromechanical resonators," *The 12th International Conference on Solid State Sensors, Actuators and Microsystems (Transducers '03),* pp. 1574-1577, June 2003.

[28] L. D. Landau and E. M. Lifshitz. *Mechanics Vol. 1.* Butterworth-Heinemann, 1976.

[29] S. Lee. *et. al.,* "Phase noise amplitude dependence in self-limiting wine-glass disk oscillators," *Tech. Digest, 2002 Solid State Sensor, Actuator, and Microsystems Workshop,* Hilton Head, South Carolina, pp. 33-26, June 2004.

[30] N.N. Bogoliubov. Asymptotic Methods in the Theory of Non-Linear Oscillations. Gordon & Breach Science, 1961.

[31] W.-T. Hsu *et. al.*, "Stiffness-compensated temperature-insensitive micromechanical resonators," *IEEE 15th Annual Conference on Micro Electro Mechanical Systems, 2002 (MEMS '02)*, pp. 731-734, Jan. 2002.

[32] R. G. DeAnna *et. al.*, "Modeling of SiC lateral resonant devices over a broad temperature range," *Technical Proceedings of the 1999 International Conference on Modeling and Simulation of Microsystems,* pp.644-647, 1999.

[33] J.-H. Jeong *et. al.*, "Evaluation of elastic properties and temperature effects in Si thin films using an electrostatic microresonator," *IEEE Journal of Microelectromechanical Systems*, vol. 12, no. 4, pp. 524-530, Aug. 2003.

[34] A. J. Fleischman *et. al.*, "Behavior of polycrystalline SiC and Si surface-micromachined lateral resonator structures at elevated temperatures," *IEEE International Conference on Silicon Carbide, III-Nitrides and Related Materials, ICSCIII-N 97,* pp. 889-892, 1998.

[35] A. J. Fleischman *et. al.*, "Surface micromachining of polycrystalline SiC deposited on SiO_2 by APCVD," *IEEE International Conference on Silicon Carbide, III-Nitrides and Related Materials, ICSCIII-N 97,* pp. 885-888, 1998.

[36] Q.-T. Hsu *et. al.*, "Mechanically temperature-compensated flexural-mode micromechanical resonators," *International Electron Devices Meeting, IEDM 2000,* pp. 399-402, Dec. 2000.

Chapter 3 Fabrication Technology

Although many MEMS fabrication processes have been developed in the past [1]-[8], most require temperatures in excess of 400°C, which precludes post-processing of most CMOS/bipolar wafers [9]-[10]. Most semiconductor processes use aluminum interconnects, and thus, elevated temperatures must be avoided to prevent damage, since the melting temperature of aluminum is relatively low (~660°C). This restriction greatly limits the number of fabrication processes and materials that can be used to integrate MEM devices with pre-fabricated circuitry. Unfortunately, many of the materials with superior mechanical properties that are of interest to MEMS designers are also difficult to deposit at low-temperatures. Silicon carbide (SiC), for example, has gained popularity in recent years due to its chemical stability and good mechanical properties; however, most chemical vapor deposition (CVD) processes require temperatures in excess of 800°C. Similarly, there is also a lack of available standard MEMS fabrication processes that are geared specifically toward RF applications, which require highly conductive interconnects and also the ability to make small vertical gaps.

In an attempt to address these issues, this work details the development of a low-temperature (<300°C), silicon carbide MEMS fabrication process, especially optimized for radio-frequency (RF) applications, through careful material selection and process development. This chapter outlines the rational for each material used in the fabrication process, along with a description of the low-temperature deposition and etching techniques that have been developed. The chapter concludes with a discussion of some of the problems that were encountered during fabrication and the solutions that were implemented.

3.1 PROCESS REQUIREMENTS

Many factors warrant the use of MEM devices in RF applications. These devices allow for better integration of entire systems, and also have the potential of improving performance; however, current MEMS processes are generally not geared towards RF applications. The following sections briefly describe some of the functional requirements of a RF-MEMS process, and discuss how it can be integrated with active electronics to form a complete, single-die, standalone system.

3.1.1 MEM Resonator Requirements

Specifically, this work is focused on the fabrication of RF-MEM resonators, which have four main requirements: 1) a structural layer with high intrinsic stiffness and low intrinsic-stress, 2) highly-conductive interconnects, 3) good electrical isolation between the input and output ports, and lastly, 4) narrow vertical gaps on the order of about 100nm. A stiff structural layer allows small resonators to be fabricated with high resonant frequencies, since the resonant frequency of a beam is directly related to the acoustic velocity of the material. Low intrinsic stress for this layer is also required in order to prevent the buckling or fracture of the released structures; for example, if there is a large compressive stress in the material, the resonator beam would buckle and prevent the device from resonating. Conductive interconnects are also required in order to efficiently transmit RF signals between the MEM resonator and external circuitry. As previously discussed, any resistive losses in these interconnects will directly add to the series resistance of the MEM resonator, and lower its effective quality factor. Input and output feedthough should also be reduced by providing adequate isolation from the substrate and across packaging - both can provide parasitic signal paths bypassing the device. Also, coupling to the substrate can result in resistive losses, which will degrade the Q-factor of the resonator. Lastly, to reduce the motional resistance of the resonator, the gap of the resonator should be made as small as possible, resulting in an increase of the electro-mechanical transduction coefficient (η). The motional impedance at resonance is inversely proportional to the fourth power of the gap distance. Minimizing the gap width reduces the insertion loss and therefore greatly reduces the gain requirements of the external circuitry when the MEM resonator is used to implement oscillators.

3.1.2 CMOS/Bipolar Integration

Another practical requirement of a RF-MEMS oriented fabrication process is that it must be able to integrate with available semiconductor technologies. Since most RF-MEM devices are designed to work with active electronics, integration in some way with semiconductor devices must be possible. Although this can be accomplished by using two separate fabrication streams, and then wire-bonding the MEM die to a separate die containing the active electronics, this is not an optimal solution. Ideally, to obtain the cost and performance benefits associated with IC technologies, the MEM devices should be integrated directly on-top of the CMOS/bipolar circuitry.

Although there are many different approaches that the MEMS fabrication process can be integrated with the semiconductor fabrication process, the easiest and most flexible one is to *post-process* complete CMOS/bipolar wafers (referred to as *post-CMOS* hereafter). This can be accomplished by adding a standalone MEMS fabrication module to the finished electronic wafers, with a direct interface between the two; however, it must be ensured that this extra process does not degrade the electrical properties of the active devices. The advantage of this method of integration is that it does not require the semiconductor foundries to modify their standard processes, and still allows them to add MEM devices to their products.

The main disadvantage of post-CMOS MEMS processing is that it imposes stringent requirements on the processing steps used to fabricate the MEM devices. Deterioration of interconnect performance due to diffusion, agglomeration, and spiking along with dopant deactivation becomes a serious problem at elevated temperatures. This is especially true in sub-micron CMOS technologies where the junction depths and interconnects are very small [11]. Since aluminum interconnects cannot be processed at temperatures much above 400°C, subsequent step must be very carefully selected to respect this limit.

3.1.3 A Simplified Surface Micromachining Process Flow

Shown in Figure 3-1 is a simplified generic micromachining process that can be used to make a MEM device. It consists of two main components: a structural layer, which is the core of the MEM device, and a sacrificial layer that is used as a spacer. The substrate will be

different depending on the application; however, in most cases, this will be plain silicon. As shown in Figure 3-1a, the substrate is first coated with a sacrificial material. This layer acts only as a temporary spacer and thus, its mechanical and electrical properties are not important. After patterning the anchors in the sacrificial material, the structural layer is deposited conformally overtop (Figure 3-1b). The shape of the MEM device is then defined by patterning the structural material. The final device is released by etching away the sacrificial material, which leaves a free-standing structure (Figure 3-1c).

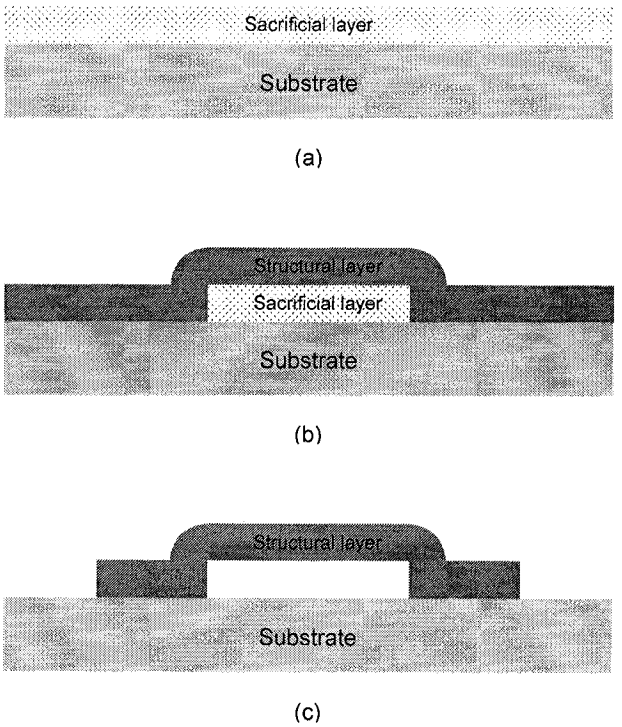

Figure 3-1: Simplified MEMS process flow

In reality, there will be many other steps and extra layers of materials used to optimize the performance of the device; for example, for RF-MEM devices, layers for metal interconnects and dielectrics for signal isolation are needed.

The following sections describe the development of a CMOS compatible, RF-MEMS micro-machining process. Each one of the main component layers in the process are addressed in sequence: structural, interconnect, sacrificial, and dielectric. For each layer, the development

of a low-temperature deposition and etching method are described in detail, along with measured characterization results from fabricated specimens.

3.2 STRUCTURAL LAYER

The structural layer forms the core of the MEM device, and its mechanical properties will have a strong impact on its performance. In recent years, a large amount of research has gone into the development of micromachining processes and, as a result, many different types of materials are beginning to emerge as viable options for micro-system designs. In the early stages of development, MEMS materials were typically limited to those that were commonly used in the microelectronics industry such as silicon, silicon oxide, silicon nitride, and common metals, such as aluminum. Now, however, MEM systems commonly employ a range of different metals, alloys, ceramics, and polymers. With the availability of such a wide range of materials to choose from, it is imperative to approach the problem of material selection with a systematic method tailored to meet a set of specific design criteria.

3.2.1 Material Selection

A useful method that is gaining popularity to compare different potential materials in microsystems design is the Ashby approach [12]: the main performance parameters of the system under consideration are first expressed as a function of some fundamental material properties, such as the Young's modulus, density, heat capacity, intrinsic loss coefficient, along with other parameters such as device geometry. By grouping the material parameters in these equations, specific material 'indices' that need to be optimized can then be isolated. A wide range of materials can be easily compared by plotting their location on a *material selection chart* which has the important material parameters or indices on each axis. For RF-MEM resonators, one of the most important characteristics is the acoustic velocity of the structural material, which is expressed as

$$\upsilon = \sqrt{\frac{E}{\rho}} \qquad \text{Eq. (3.1)}$$

where, E is the Young's modulus and ρ is the density. As shown previously, the resonant frequency is directly related to the acoustic velocity of the structural material, and thus one of the goals is to make it as large as possible. Conventional MEMS fabrication processes have generally used silicon structural layers because of the availability of mature deposition and etching methods, however, a recent trend to push RF-MEM filters into the ultra-high frequency (UHF) range has spurred a flurry of research into alternatives. Shown in Figure 3-2 is a material selection chart with density on one axis and Young's modulus on the other [12]. The parallel lines on the graph indicate constant values of acoustic velocities. Note that different types of materials tend to be grouped together. Ceramic materials appear in the top left, metals appear in the middle-right, while polymers and elastomers are grouped together in the bottom-left. From this chart, it is clear that the better alternatives to Si would be silicon carbide (SiC), alumina (Al_2O_3) or diamond (C). Of these three, SiC is the most interesting choice, since the processing technology it requires is relatively mature. Although great strides are being made in developing nano-crystalline diamond for microsystem design [3], the technology is still not widely available. Note that all metals and polymers would be poor choices for a structural layer, as they lie very far from the top of the chart.

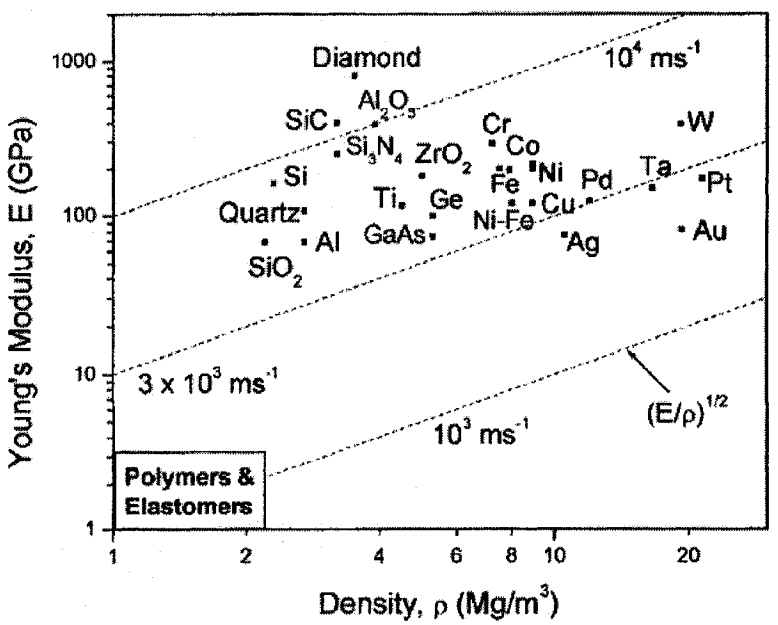

Figure 3-2: Young's modulus - density material selection chart for various MEMS materials [12]

Silicon carbide is a material that is polymorphic and thus, depending on the deposition method and temperature, can take on a number of different crystal structures. It has three main polytypes: cubic (3C), hexagonal (4H) and rhombehedral (6H). Each one is characterized by a different atomic arrangement, but all have the same silicon to carbon ratio. High crystal quality can be obtained by growing SiC epitaxially on substrates of like crystal type; however, these methods utilize temperatures in excess of 1500°C [13] and are not suitable for low-temperature fabrication processes. Crystalline SiC is typically used as a substrate in advanced high-power microelectronics. Since single crystal SiC needs to be epitaxially grown on a base substrate, it is not suitable for use in micromachined structures where the underlying sacrificial layer is not silicon. As a result, the most common form of SiC used in the fabrication of microsystems is polycrystalline (β) or amorphous (α). Both can both be deposited using low-temperature techniques. The major advantage of poly-crystalline and amorphous SiC is that it can be deposited on a wide range of substrates and materials, which makes it ideal for surface-micromachining.

3.2.2 Deposition of SiC

Thin films of silicon carbide have traditionally been deposited using one of four different methods: 1) low-pressure chemical vapor deposition (LPCVD) [14][15], 2) atmospheric-pressure chemical vapor deposition (APCVD) [16], 3) plasma-enhanced chemical vapor deposition (PECVD) [17]-[20] or 4) magnetron enhanced sputtering [21]-[25].

Both LPCVD and APCVD have been used to successfully deposit SiC films; however, these reactions are usually highly endothermic, and hence require temperatures in the order of 800°C to 1280°C. To deposit the film, one or more precursors in gaseous form are introduced into a furnace at elevated temperatures where they react with the surface to form SiC. Good films have been deposited using this technique with a single precursor such as 1,3-disilabutane (DSB) [14] or tetramethylsilane (TMS) [15], both of which contain carbon and silicon. The resulting film structure is polycrystalline and will typically depend on the underlying substrate. For amorphous substrates, such as silicon oxide and silicon nitride the SiC films tend to have randomly oriented grains [13]. At elevated temperatures, fully

crystalline 3C-SiC can be grown heteroepitaxially on Si substrates due to the similar crystal structure; however, typical process temperatures are in excess of 1500 °C [13].

APCVD has also been used to successfully deposit polycrystalline SiC using a two step process that first involved the carbonization of a silicon (or poly-silicon) substrate, and then the deposition step using a combination of several reactive gases [8]. SiC films deposited using this process have been used for the fabrication of MEM resonators; however, the process temperature is still well in excess of 1000°C. As a result of these high temperatures, no method to date has allowed for *post-CMOS* integration using APCVD or LPCVD of SiC. Furthermore, the deposition rate is typically very low since the overall reaction is limited by the surface reaction rate (as opposed to mass transfer to the substrate).

The process temperature of CVD may be significantly reduced if extra energy is supplied in the form of a plasma. PECVD uses a RF-induced plasma to transfer energy to the reactant gases, which allows the substrate to remain at a much lower temperature. Using this technique, room temperature deposition is possible. The composition of SiC deposited at these relatively low temperatures is amorphous or polycrystalline with crystal grains present in more quantity when the deposition temperature is increased [17]. Residual stresses in deposited films, however, are typically very high, and therefore a post-deposition anneal is required [18],[20].

For the SiC deposition in this work, magnetron enhanced sputtering was used, since it can be performed at room temperature and no special CVD processes are required. Sputtering is performed by bombarding a SiC target with positive argon ions created in a plasma. These incident ions sputter away material by physical momentum transfer, which then condenses onto the substrate. Since this is a purely physical process, no external heat source is required and the process can be performed at room temperature; however, the substrate temperature will rise marginally due to bombardment by secondary electrons, and neutral atoms. The maximum temperature of the substrate measured in this work was 170°C, which is considerably lower that most CVD processes. Another advantage of physical sputtering is that deposited films are conformal and adhere well to the substrate. It has a relatively high deposition rate, and residual stresses can be nearly eliminated by careful selection of the

process parameters [21],[25]. Also, the sputtering process is relatively simple, and can be performed using only argon gas and a sintered SiC target.

Because of the lower deposition temperatures used in sputtering, the silicon carbide will be amorphous in structure; however, most of the attractive properties such as the high elastic modulus, hardness and inertness still remain [24]. Amorphous films, unlike crystalline or poly-crystalline ones, posses a random arrangement of atoms, and therefore, its material properties are isotropic. Another potential advantage of amorphous SiC is that it is not conductive, which increases design flexibility since RF signals can be routed on both the top and bottom surfaces of the structural layer. This requires an extra metal layer to form electrodes on the underside of the structural layer. It should be noted here that, unlike other SiC micromachining processes that use high temperatures, in this work metal can be deposited *before* the structural layer. To the best of the author's knowledge, this is the first time that amorphous silicon carbide has been used to build RF-MEM resonators.

Typically, sputtered SiC is deposited using a RF-plasma based system due to its insulating nature. For this work, however, sputtering is performed using a DC sputtering system, in conjunction with a specially designed, conductive SiC target (Hexoloy SG). Hexoloy SG was first patented in 1985 by the Kennecott Corporation and is now provided through Saint-Gobain Advanced Ceramics [26]. It is composed of alpha-SiC, with carbon in the amorphous and graphite forms dispersed throughout the matrix. This allows SiC to be easily deposited with the equipment that is readily available to us at the McGill micro-fabrication facility. Similarly, it also reduces the hardware requirements to fabricate devices since this DC-sputtering system is also used for the deposition of all other metal layers. This allows for a low-cost and simple low-temperature solution to SiC deposition.

The following sections describe the development of a low-stress and low-temperature DC sputtering process for SiC using Hexalloy SG. Measurements of the deposition rate, intrinsic stress, and surface roughness for different values of the sputtering pressure and power are provided. The process parameters are optimized to obtain films with low-stress with a reasonably high deposition rate.

3.2.2.1 Deposition Rate

SiC was deposited using a MRC 603 DC sputtering system onto six-inch silicon substrates, while varying several different process parameters. The resulting film thickness was determined by selectively masking parts of the substrate with Kapton™ tape, and then measuring the step height with a Tencor P1 surface profilometer. Similar in operation to an atomic force microscope, the profilometer drags a highly sensitive stylus over the surface of the film and is capable of measuring the surface roughness and changes in the film thickness to within 1nm.

To eliminate moisture from the surface of the substrates and improve film adhesion, the wafers were baked for 30mins at 150°C before sputtering. The substrates were also allowed to outgas for 5 minutes in the system's load-lock chamber kept at a very low base-pressure. This further helps to remove any residual surface moisture.

Films were deposited at powers ranging from 300W to 2kW, and chamber pressures from 3mTorr to 25mTorr. Higher powers were not investigated because of the possibility of de-laminating the SiC target from its backing plate through excess bombardment heating. Since this sputtering system linearly scans the wafers back and forth across the target, the film thickness could be adjusted by changing the number of passes and scan rate. This helps to improve both the film uniformity and step coverage.

Since one of the goals was to achieve a high deposition rate, all subsequent optimizations were done with a DC source power of 2000W. Figure 3-3 shows the measured deposition rate of SiC versus process pressure. As expected, the deposition rate decreases slightly with increasing pressure due the reduction in the mean free path length in the plasma [9]. In order to compare the deposition rate obtained in this work with other reported values, an *effective* deposition rate was calculated that takes into account the time for one pass of the wafer across the target. The average measured deposition rate at 2000W was about 75nm/min, and is calculated based on the amount of time it takes to scan a 6 inch wafer across the SiC target. This rate is superior to the RF sputtering of SiC done elsewhere [21],[23], and also to the DC sputtering reported in [22]. Table 3-1 provides a brief comparison of the published deposition rates using a number of different methods.

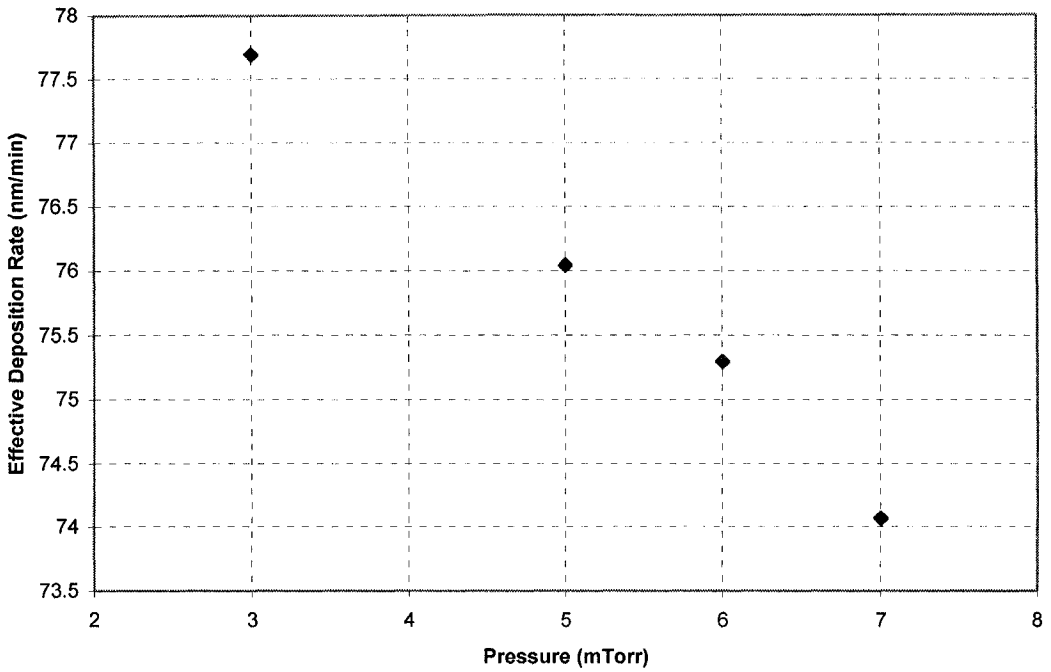

Figure 3-3: SiC deposition rate vs. pressure for a DC source power of 2000W

Table 3-1: Comparison of published SiC deposition rates

Reference	Deposition Method	Maximum Reported Deposition Rate (nm/min)
[22]	DC Sputtering	30
[23]	RF Sputtering	30
[21]	RF Sputtering	18
[24]	RF Sputtering	30
[20]	PECVD	100
[16]	APCVD	17
[27]	LPCVD	50
This work	DC Sputtering	75

When the DC power is decreased to 1000W, the deposition rate drops down to about 40nm/mn; however, since we desire the highest deposition rate possible, values of the source power lower than 2000W were not further investigated.

For this work, the SiC structural layer was selected to be 2μm thick, which is a compromise between resonator frequency and deposition time. With a source power of 2000W and chamber pressure of 6mTorr, 2μm±0.05 of SiC was deposited using 9 scans at 5cm/min. At this relatively high power significant substrate heating occurs due to both bombardment by secondary electrons and neutral atoms. The maximum substrate temperature reached during deposition was measured to be ~175°C, which is still much lower than that of most CVD processes.

3.2.2.2 Material Study Results

The surface morphology of the deposited films was first examined using scanning electron microscopy (SEM). Figure 3-4 shows an SEM picture of the surface of a 0.7μm SiC film, deposited at a process pressure of 6mTorr, and a source power of 2000W. At a magnification of 2000x (Figure 3-4a), the SiC film appears smooth except for the presence of large nodules that are uniformly distributed across the surface. These nodules protrude from the film and vary in length from a few hundred nanometers to as much a 1 to 2 micrometers.

The maximum height of the nodules primarily depends on the thickness of the film, with measured peaks as large as 1000nm on a 2μm thick film. In most samples, the maximum nodule height was less than 50% of the film thickness. A magnified picture of one of these protrusions is shown in Figure 3-4b, where the nodule surface appears to be highly textured and made of multiple large clusters. Between nodules, however, the film surface is very smooth and uniform. At a magnification of 100 000x (Figure 3-4c), the surface between these protrusions appears to be composed of regular grain-like nucleations with an average diameter of about 50nm.

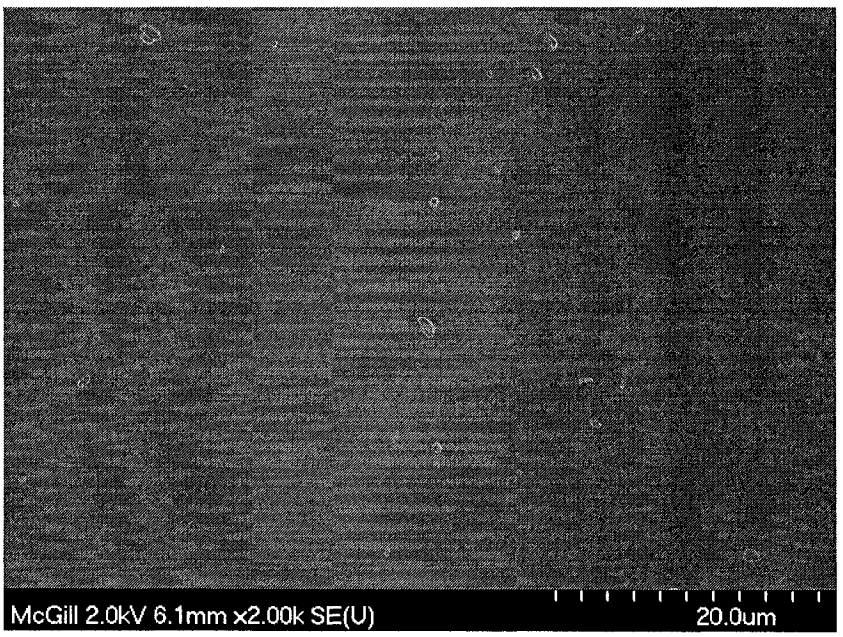

(a)

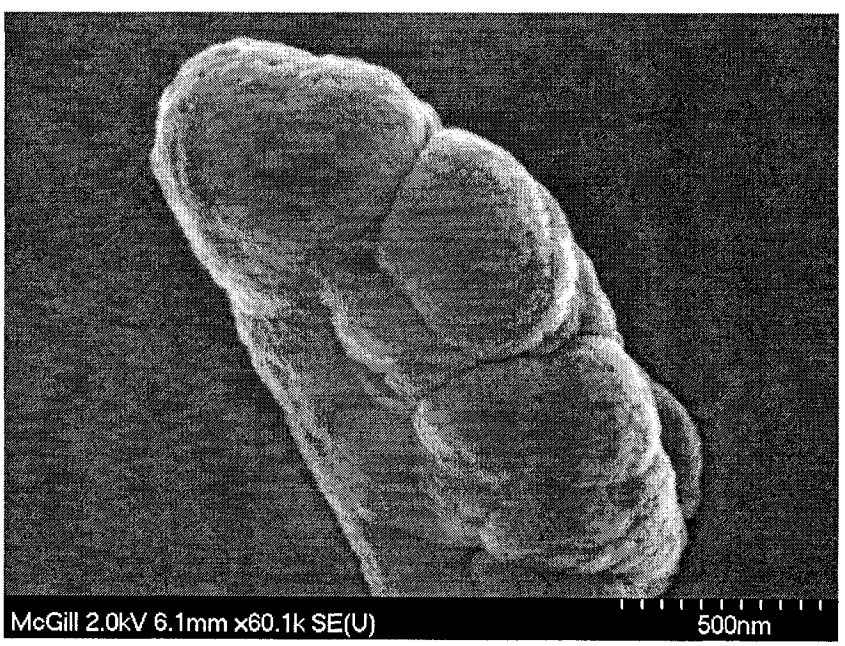

(b)

Figure 3.4: Continued on next page

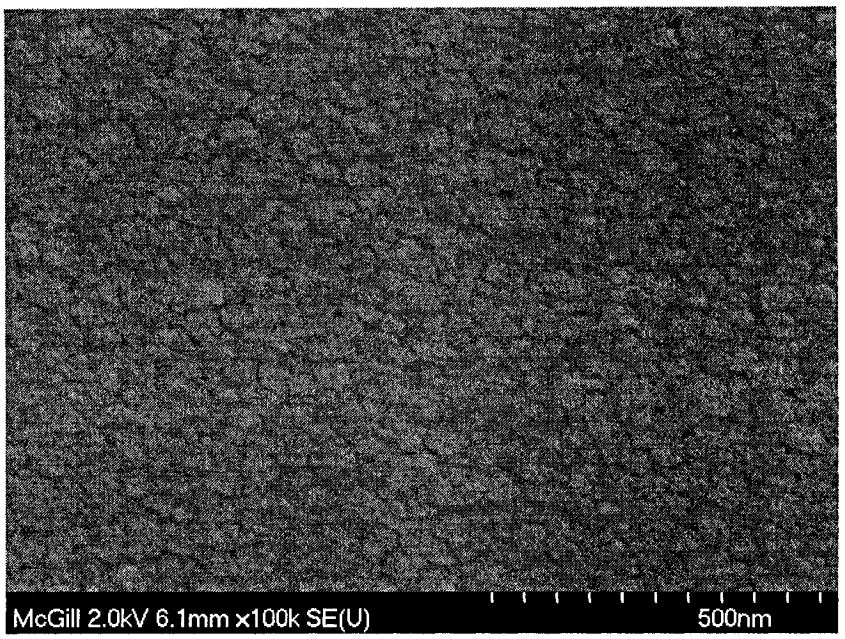

(c)

Figure 3-4: (a) SEM picture of the surface of a deposited SiC film (2000x), (b) Magnified picture of a surface nodule (60 000x), (c) magnified portion of the flat film surface between nodules (100 000x)

The root-mean square surface roughness (R_{rms}) was obtained using a Tencor stylus profilometer. The average R_{rms} of the sample in Figure 3-4 is 52nm, which corresponds well with the average size of the SiC clusters shown in Figure 3-4c. For thicker films, the measured roughness was larger due to the larger size of the surface nodules. The R_{rms} of a 2μm thick SiC film deposited under the same process conditions was found to be approximately 70nm. This value is an average calculated from numerous measurements done on four different wafers. The minimum and maximum R_{rms} in this case was 43nm, and 103nm, respectively.

No correlation could be found between the size and distribution of these nodules to either the deposition pressure or power. In general, the maximum size and height of these protrusions were only observed to depend on the film thickness.

One possible source of these formations is the unintentional sputtering of large clusters of material from the SiC target, as a result of micro-arcing. To allow the DC sputtering of SiC, the Hexoloy SiC target includes graphite to increase its conductivity; however, as a result of

graphite's unique microstructure, its electrical properties are directionally dependent (anisotropic) [28]. During sputtering, this non-uniform conductivity can result in an uneven charge buildup in certain areas of the target, depending on the spatial orientation of the graphite grains with respect to the applied electric field. Similarly, since the target is also composed of grains of relatively non-conductive SiC, this may further aggravate this charging problem. This non-uniform electrical potential (field gradient) across the target surface can lead to micro-arcing between adjacent grains which eject large particles that are subsequently deposited onto the substrate [29]. A known solution to this phenomenon is to use pulsed-DC sputtering which does not allow for charge build-ups to occur because of the constant charging and discharging of the target [30].

Another possible source of these particles may be from the growth and destruction of micro-filaments on the target surface. A common problem encountered when using magnetron enhanced sputtering is the growth of filaments due to the accumulation of the extremely fine "dust" found on the surface of sputter targets during operation [31]. This dust preferentially accumulates at charged areas of the target which creates filaments oriented in the direction of the electric field. These filaments eventually grow long enough so that they short the target with the plasma sheath, at which point they arc and explode, depositing particles on the substrate surface.

Although the exact cause of the growth of these nodules on the substrate surface is presently unknown, they do not present a significant problem since they are relatively small in relation to the typical size of a micromachined resonator; however, if future applications of this technology require smooth surfaces, chemical-mechanical polishing (CMP) may be needed [32].

The film composition was studied using energy dispersive X-ray (EDX) composition analysis. EDX uses measurements of the characteristic X-rays emitted from a sample in a scanning electron microscope to obtain an approximate value for the atomic composition. In order to measure the ratio of silicon to carbon in the DC sputtered films, 2μm SiC films were first deposited onto aluminum substrates (2000W, 6mTorr). Since the electron beam of the SEM has an effective volume of interaction which is typically on the order of the film

thicknesses used in this work, the SiC was deposited on a non-silicon substrate to prevent an unwanted increase in the measured silicon peak.

Calibrated EDX measurements were made of both large areas, to get an average value for the silicon to carbon ratio of the film, as well as measurements of just the nodules. The averages for the measured atomic composition of the SiC film and nodules are summarized in Table 3-2.

Table 3-2- EDX measurements of a SiC film to determine atomic composition

Measurement	Silicon (%)	Carbon (%)	Oxygen (%)
Film Average	47.7	51.6	0.7
Nodule Average	35.6	62.8	1.6

The traces of oxygen are most likely a result of oxidation of stray silicon, which is not critical to film composition in these trace amounts. Measurements indicate that the deposited films have a carbon to silicon ratio of about 1.08. The slight excess of carbon present in measurements is believed to be a result of the uneven sputter yield of the graphite and sintered SiC in the target. The composition analysis of the nodules reveals that the average carbon content of these bumps is in fact about 11% higher than the film average. This gives further evidence which suggests that the nodules may be the result of particulates created by arcing between graphite gains.

The film crystalinity of the sputtered SiC was also studied using X-ray diffraction (XRD) analysis. The following two plots show XRD analysis results of a 2μm SiC sample deposited on a {1,0,0} Si substrate. The crystal structure of the film can be determined by looking at the location of the peaks in this graph. These may be used to determine the nature of the SiC deposited, since X-ray diffraction at different incidence angles is characteristic of different crystalline and material structures.

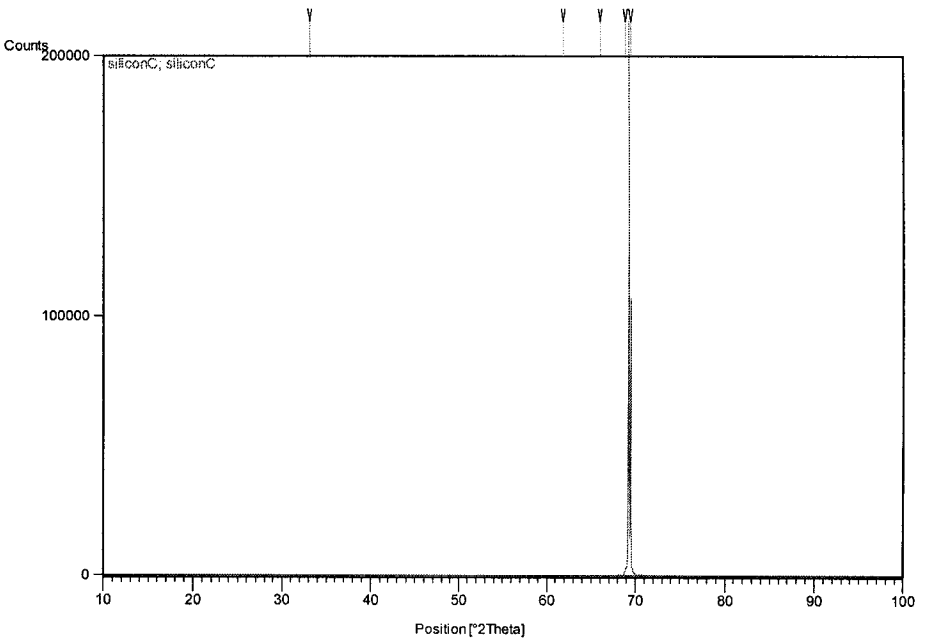

(a)

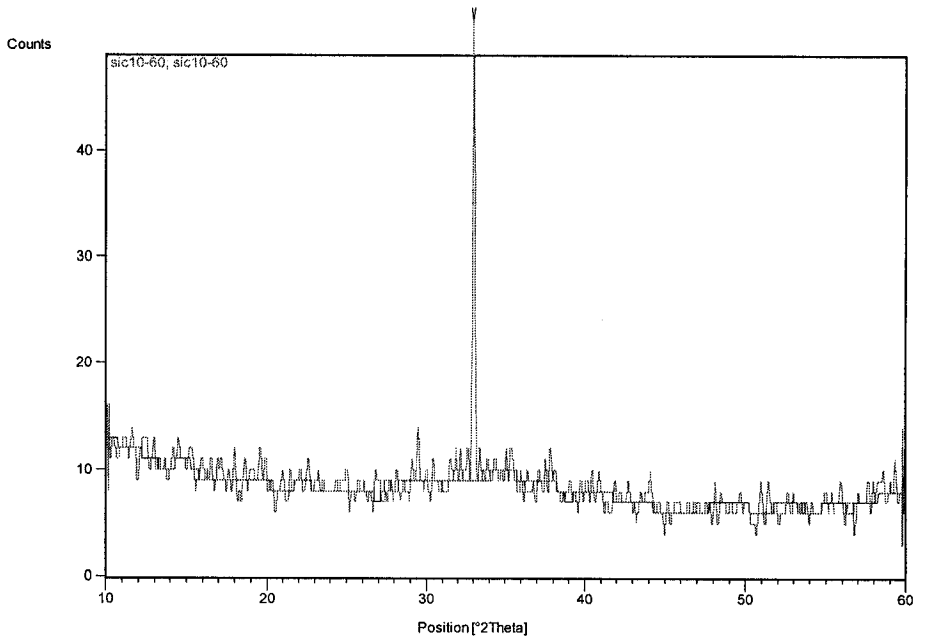

(b)

Figure 3-5- XRD scans from (a) 10°-100° showing the single crystal Si peak at 69° (b) 10°-60° showing low-intensity single-crystal Si satellite peaks at 33°

Figure 3-5 (a) shows a scan from 10 to 100°. The large peak at 69° corresponds to the (4,0,0) reflection of the single-crystal silicon substrate [15]. Evidently, there is no other peak, suggesting that SiC is amorphous. Figure 3-5 (b) shows a second scan from 10 to 60°, to ensure that the large silicon peak is not masking any smaller peaks from SiC. This scan shows a low-intensity satellite peak at 33°, which is always seen with single-crystal silicon, but no other peak corresponding to crystalline or polycrystalline SiC. This then confirms the amorphous nature of the deposited film as would be expected from the deposition temperature.

The conductivity of the SiC was determined by probing isolated micro-striplines using DC needles and a Fluke multi-meter; however, the measured resistivity was beyond the equipment's measurement range of 40MΩ. Using this measured value, a lower bound of the films bulk resistivity was calculated to be about 550 Ω·cm. This value corresponds with the measured value of ~2000 Ω·cm reported in [25].

3.2.2.3 Stress Control

Regardless of the deposition technique, residual stresses are almost always present in thin films and can cause micro-machined devices to either buckle or fracture if not sufficiently controlled [33]. These stresses can be either compressive or tensile, and can cause significant geometric distortion of released devices. Consider the two cases shown in Figure 3-6. If a film is deposited with a large tensile stress, it will tend to create a force pulling inward on underlying layers (Figure 3-6a), while a compressive stress will push outward (Figure 3-6b). Under sufficient tensile stress, films may crack and fracture, whereas under large enough compressive stress, constrained, MEM devices may buckle. In the case of MEM beam resonators, these stresses can cause the structural layer to deform enough so that an electrical short-circuit forms between the top and bottom electrode, rendering the device inoperable. Stress control is especially important in this case, since the typical gap spacing between these two layers is usually less than 200nm.

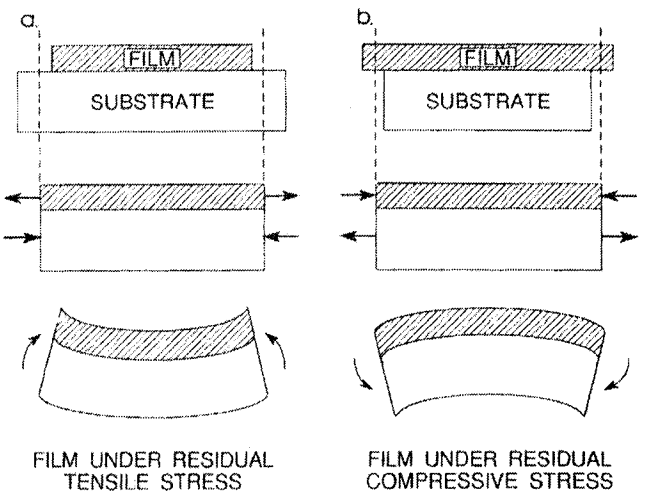

Figure 3-6- Different stress polarities in deposited films (a) Tensile (b) Compressive [33]

There are two main types of stresses: intrinsic and thermal stress [34]. Intrinsic stresses, also known as growth stress, develop during film nucleation and are primarily a result of the non-equilibrium nature of deposition processes [9]. In some processes, poor atom surface mobility and relatively high growth rates do not allow the film to relax during deposition, which yields an atomic structure that is not in its lowest energy state. Other sources of intrinsic stress include volume changes during phase transformation; lattice mismatch between epitaxially grown films and substrate; and interstitial or substitutional impurities [9]. The magnitude of the intrinsic stress will strongly depend on the process used and parameters, such as the deposition temperature, pressure and power. Thermal stress, on the other hand, is a result of differences in thermal expansion between the substrate and film, and can develop when high-temperature processes are involved. When a film is cooled after deposition, the substrate may shrink to a lesser or greater degree which will result in significant residual stress.

One major advantage of sputtering is that the residual stress can be tuned from compressive to tensile by adjusting the pressure of the deposition process. If the deposition pressure is selected so that the stress is at (or near) the cross-over point, the deformation of released structures will be minimized. At low pressures, sputtering processes tend to yield films with compressive stresses. Due to the low mean-free path, atoms strike the substrate surface with

high energy, resulting in atomic shot-peening and densification of the film [34]. This effect is more pronounced for bombardment at normal incidence, which occurs at low pressures. At higher pressures, the average incidence angle is wider (as a result of scattering in the argon plasma) which leads to local shadowing and a porous microstructure [34]. After deposition, atoms do not have enough mobility to sufficiently fill in these microvoids which leads to a tensile film [9]. The cross-over point where compressive stresses become tensile is useful for stress control and is a great advantage of this deposition technique.

Stress measurement of deposited SiC films was performed using the wafer curvature method with a Tencor Flexus 5200 film stress measurement system. As shown in Figure 3-7, the measured stress of the deposited film goes from compressive to tensile at a working pressure of approximately 6mTorr. This value is consistent with other published work using Hexoloy DC sputtering [25]. Using this method of stress control, films have repeatedly been deposited with measured residual stresses of less than ±50MPa.

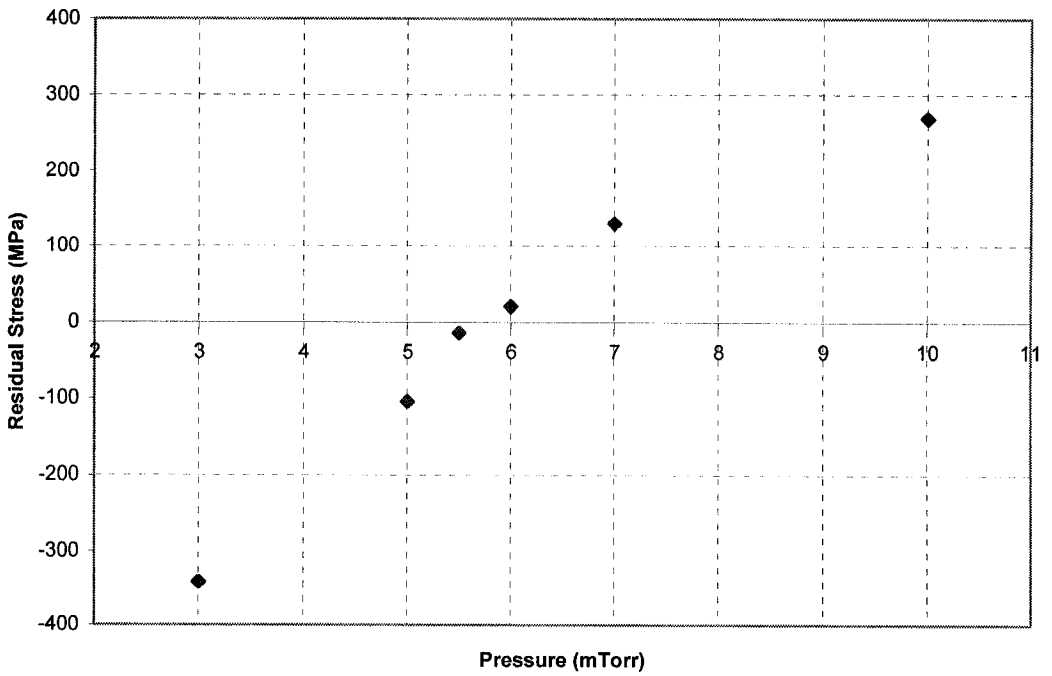

Figure 3-7: Internal stress of deposited SiC versus working pressure

3.2.3 Etching of SiC

As the popularity of silicon carbide grows for applications in both microelectronics and micromachining, significant effort is being put into developing effective patterning techniques. In general, the patterning of SiC is much more difficult than other commonly used semi-conducting materials because of its low reactivity. Due to the strong inter-atomic bond of the silicon and carbon atoms (1.34 times stronger than a Si-Si bond), etching using aqueous solutions must be performed at temperatures greater than 600°C [35], which makes wet etching impractical for low-temperature processes. As a result, most patterning of SiC is done using dry techniques such as reactive-ion-etching and lift-off. Using lift-off is an attractive method since it can be used to pattern any type of material. In this technique, SiC is first non-conformally deposited over a high-aspect ratio pre-formed mold. Next, the temporary mold is then removed using a wet etch, which lifts-off the unwanted SiC and leaves the patterned structure behind. Even though this method yields good results [2], it is still quite involved and necessitates the use of multiple steps and sacrificial materials.

By far, the simplest and most commonly used technique to pattern SiC is with dry plasma-based methods such as reactive-ion-etching (RIE). RIE etching makes use of the DC bias that is generated by a glow-discharge to accelerate reactive ions toward the substrate. Not only do these ions physically sputter material, but they also induce surface damage that enhances the reaction rate with other neutral free radicals in the plasma. The process is very similar to DC sputtering; however, in the case of RIE, the target is the wafer and is placed on the negatively charged cathode (as opposed to the anode in the case of sputtering). Also, the ions in the plasma are generated from a reactive gas as opposed to sputtering, which typically uses an inert gas such as argon. The rate of the overall etch process is dependant on many factors which include pressure, RF power, gas flow rate, DC bias, cathode temperature, and gas chemistry. As will be demonstrated, these parameters can be optimized to obtain highly anisotropic profiles in SiC and etch rates greater than 2000Å/min. To increase the etch rate further, the RIE chamber can be magnetically enhanced (ME) using large electro-magnets which set-up a transverse magnetic field to help contain electrons in the plasma and reduce recombination on the reactor walls. The result is highly-dense plasma that can be sustained at

lower pressures, with a lower self-induced DC bias [36]. ME-RIE reduces the surface damage of the substrate during etching, while increasing the overall etch rate due to the large increase in charged ions. Other techniques to increase the ion density and reduce ion surface damage include inductively-coupled plasmas (ICP) and electron cyclotron resonance (ECR), which decouple the DC bias from the power source. Magnetic containment can increase the ionization ratio for a regular parallel plate reactor from 10^{-4} to 10^{-6}, to 10^{-2} to 10^{-4} [9], or about two orders of magnitude.

The ensuing sections discuss the basics of silicon carbide RIE, including plasma chemistry, primary etch mechanisms, and the optimization of process parameters to obtain residue free, anisotropic etch profiles in SiC. Lastly, a summary for the optimized etch recipe is given along with some illustrative results.

3.2.3.1 Etch rate

In this work, the etch stop for the RIE step is the sacrifical layer which is less than 200nm thick. Thus, the etch rate of the process must be determined to a reasonable degree of accuracy, to avoid over-etching and damaging underlying layers. Ideally, the etch rate should be as high as possible, in order to minimize the etch time; however, this typically results in trade-offs with other parameters such as etch anisotropy.

Reactive ion etching of SiC can be accomplished with a variety of halogenated gases. Although some research has been done with Cl_2 [37] and HBr [1], the majority of work in the literature has focused on etching using fluorinated plasmas such as NF_3 [38][39], SF_6 [35][40][41], CHF_3 [42], CF_4 [43], and $CBrF_3$ [35] which are widely used in the microelectronics industry for etching silicon. Of all these fluorinated gases, nitrogen tri-fluoride (NF_3) was chosen to be the primary gas used in this work for several reasons. Firstly, it is the most copious producer of F ions and as a consequence has the highest etch rate of all the fluorinated gases. Second, it is also one of the few gases that can be used to etch SiC with little resulting etch field residue (see section 3.2.3.2). When SiC is patterned with metal masks, all fluorinated gases result in significant etch residue, with the exception of NF_3 and CHF_3. The drawback of CHF_3, however, is that the etch rate is very low since the added hydrogen in the plasma is a fluorine scavenger [44]. Third, high etch rates can be obtained

without using mixtures of oxygen, which can cause excessive residue formation. Lastly, NF_3 consistently produces the most anisotropic etch profile [35][44].

The etch rate was measured after varying several key process parameters to determine some general trends. By no means is this an exhaustive study, however, it is still insightful to look at the etch rate at extremes in the process parameters to gain some understanding of the etch mechanisms at work. Table 3-3 provides the etch rate of sputtered Hexalloy SiC at different values of pressure, power, magnetic field and for several different fluorinated gases. For this study, three gases were considered: nitrogen tri-fluoride (NF_3), sulfur hexafluoride (SF_6) and carbon hydro-tri-fluoride (CHF_3). All of these are commonly found in the microelectronics industry and have been used for RIE of SiC in the past with varying degrees of success. For all of these etch rate measurements the cathode was kept at 10°C using helium back-side cooling to help improve etch anisotropy.

Table 3-3: Etch rate of SiC under various process conditions

#	Gas	Gas Flow Rate (sccm)	RF Power (W)	Pressure (mTorr)	Magnetic Field (G)	Etch Rate (Å/min)
1	NF_3	20	50	8	20	**376**
2	NF_3	20	100	8	20	**850**
3	NF_3	20	100	8	0	**534**
4	NF_3	10	100	6	20	**740**
5	NF_3	25	100	50	20	**434**
6	NF_3	15	400	6	20	**856**
7	NF_3	15	400	6	65	**2079**
8	NF_3	25	400	50	20	**1373**
9	NF_3	25	400	50	65	**1768**
10	NF_3	25	400	160	20	**673**
11	SF_6	25	100	20	20	**309**
12	SF_6	25	100	50	20	**449**
13	CHF_3	25	400	50	20	**70**

In this table, the process parameters tested that yielded the highest etch rate are shown shaded in grey. NF_3 is the most copious producer of fluorine radicals and thus, has the highest etch rate of the three gases. CHF_3 on the other hand is the lowest due to the presence of hydrogen in the plasma, which acts as a fluorine scavenger. Hydrogen reacts with fluorine radicals to form HF, which reduces the available reactive species and thus lowers the etch rate.

Two main etch regimes can be identified which depend mainly on the ionization power and ion flux. At low ion energy (high pressure and low power) the etch is primarily dominated by chemical etching by free radicals as the sputter efficiency and ion-enhanced neutral chemical etching efficiency are low. This results in a lower overall etch rate. At high ion energy (low pressure and high power) the etch process is dominated by both the sputter removal of material and by ion-damage etch-enhancement. Note that with the added ion-induced surface damage, the etch rate is much higher. As will be shown later, the higher ion energy also helps to remove non-volatile etch residue that can cause significant roughness in the etch field.

To improve the etch rate, the plasma density can be increased by using electro-magnets to create a magnetic field in the etch chamber and by increasing the RF power. The magnetic field helps to contain electrons in the plasma and reduce losses to the reactor walls. Using this addition, dense plasmas can be created at lower pressures. As shown in Table 3-3, the magnetic field can be used to greatly increase the etch rate; for example, the etch rate at 65G (sample #7) is almost three times that at 20G (sample #6).

Increasing the power also increases the etch rate almost linearly. The increase in power increases the DC bias, and also the plasma density, which results in a higher concentration of free radicals. The extra bombardment of the surface creates more damage and, therefore, the etch rate is greater. The highest etch rate obtained was ***2079 Å/min*** at a power of 400W, a magnetic field strength of 65G and a low pressure of 6mTorr. Due to the high power and low pressure, however, sputtering of the mask was also increased which necessitated the use of a thick mask with a relatively low sputter yield. SiC is commonly etched using metallic masking materials, since the etch rate of even hard-backed resists under these etch conditions is very high. Although the selectivity was not measured explicitly, hard-baked photo-resist masks were observed to only last a few minutes before being completely removed. Not only

does this limit the thickness of SiC that can be etched, but it also results in a poor anisotropy ratio since the mask edges are quickly eroded away. Metallic masks patterned from aluminum and chromium were found to last much longer and had measured etch selectivities in the range of 4:1 to 11:1. Table 3-4 compares the measured etch rates of chromium, aluminum and SiC under the conditions which yielded the highest SiC etch rate.

Table 3-4: Etch rate of masking materials

Process Parameter	Value
Etch Gas	NF_3
Gas Flow Rate (sccm)	15
RF Power (W)	400
Pressure (mTorr)	6
Magnetic Field (G)	65
SiC Etch Rate (Å/min)	2079
Al Etch Rate (Å/min)	438
Cr Etch Rate (Å/min)	199

Interestingly, even though the sputter yield for chromium is higher than for aluminum [9], the overall etch rate under these conditions is about half. This is most likely the result of a weak chemical reaction that exists between aluminum and fluorine. Evidence suggests that during the etch Al and F form aluminum fluoride which is non-volatile, but is still sputter etched away (potentially at a faster rate than pure Al). Thus, using a chromium mask is much more advantageous, since it allows the use of a thinner mask which helps improve the side-wall profile. As will be discussed later, it also does not result in micro-masking of the etch field, unlike when etching with aluminum masks.

3.2.3.2 Residue

One of the main difficulties encountered when etching SiC is the presence of residue in the etch field which results from a phenomenon called "micro-masking." As described previously, when a material is etched using RIE it forms both volatile and non-volatile etch

products. Ideally, the gas chemistry should be chosen so that the target material is removed through a reaction that results in volatile products, which can subsequently be pumped out of the chamber; however, the metallic masking materials commonly used to etch SiC do not form volatile etch products with fluorine. This is in fact desired, since the etch selectivity of the mask should be high, and the mask should persist as long as possible. In the case of aluminum, it weakly reacts with fluorine to form non-volatile AlF_x which does not get removed in the gas phase. The masking material and its non-volatile reaction products, however, are still slowly removed by physical sputtering by charged ions, albeit at a much slower rate. Since these materials are not removed in the gas phase, when they are sputtered away they get re-deposited on the wafer surface and chamber walls. If the re-deposited material lands in the etch field, it creates small localized masks. Since the RIE of SiC is typically highly anisotropic, this results in long columnar structures that tend to remain in the etch field. A more problematic issue arises when these non-volatile materials are re-deposited on the actual sidewall of the etched material. This can occur by direct sputtering of the mask or by re-deposition from non-volatile etch products in the etch field. Since the etched profiles are typically very anisotropic (>2:1), this residue is not easily removed [9] and creates a discontinuity in the etch profile.

Another problem encountered when reactive-ion etching SiC is the slow carbon removal rate. The reaction efficiency of fluorine with carbon is typically much lower than with silicon. Many researchers have reported a high carbon density near the SiC etch surface, which has been attributed to the preferential removal of silicon [45][46]. This effectively results in another source of micro-masking. Since silicon is removed very efficiently through the chemical reaction with fluorine radicals, a high density of carbon from the SiC is left on the surface during the etch which tends to mask the material below.

There has been a significant amount of research done on ways to eliminate this residue by using different mixtures of fluorinated gases. A good review of the effect of gas chemistry on the RIE of SiC is given in [44]. Almost all fluorinated gases have been shown to produce etch residue when using metallic etch masks, with the problem being aggravated further with the addition of oxygen. Oxygen is commonly added to increase the etch rate, however, it also

forms non-volatile aluminum oxide which makes the micro-masking problem worse. Of all the commonly used fluorinated gases used for RIE of SiC, only NF_3 and CHF_3 result in low residue when used in their pure forms [44]. Of these two, NF_3 is again the most suitable, since its etch rate is nearly an order of magnitude higher. A comparison of the measured etch rate of NF_3 and CHF_3 are shown in Table 3-3. CHF_3 is known to be a non-aggressive etch gas due to the presence of hydrogen in the plasma which acts as a fluorine scavenger. The etch rate can be improved by mixing it with oxygen, however, micro-masking then begins to appear in the etch field.

Another way to eliminate residue is to add hydrogen to the fluorinated gas and oxygen mixture to increase the volatility of aluminum etch products. As shown in [44], residue can be completely eliminated for all common fluorinated gas and oxygen mixtures by adding hydrogen to the chamber. Evidence suggests that the hydrogen in the plasma reacts with the aluminum to form alane gas (AlH_3) which is volatile. This helps to remove re-deposited aluminum from the etch field and prevent micro-masking. Using this technique, a residue free surface has been successfully obtained for several different fluorinated gases in the presence of oxygen. The main drawback of this method is that the mixture of H_2 and O_2 in a closed chamber creates safety concerns. Under specific conditions, this combination can be explosive. Thus, pure NF_3 was chosen as the primary etch gas for all subsequent tests, since it still has a very high etch rate and low tendency to produce residues, even without the addition of other gases.

Initial etch tests performed with aluminum masks and NF_3 were largely unsuccessful. To obtain good anisotropy these etches were performed at a low RF power (100W or $0.3W/cm^2$) and at several different pressures. At this low power, however, there was significant residue left in the etch field. Figure 3-8 shows the etch field and test structures etched using 0.2um aluminum masks, under a process pressure of 50mTorr. In this case, the layer under SiC is a 2000Å thick chromium film that acts as an etch stop. As shown in Figure 3-8, the residue in the etch field is highly 'grassy'. This is most likely a result of the preferential removal of Si over C, and of micro-masking caused by re-deposited aluminum compounds. Note, however, that the side-walls of the etched structures are smooth and almost vertical with a measured

anisotropy ratio of >20:1. Since the pressure is relatively high, sputtering in the etch field is reduced and thus, re-deposition of non-volatile etch products on the sidewalls of the SiC is minimal, yielding a nice regular profile.

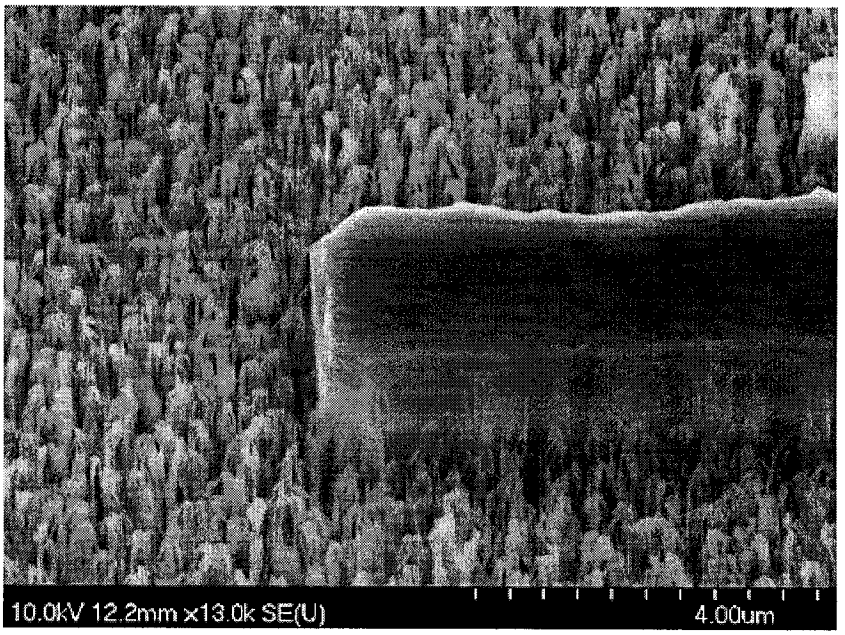

Figure 3-8: SiC test structure etched at 50mTorr

This residue left in the etch field was found to significantly reduce the measured contact quality to the underlying metal layers. Since these deposits are non-reactive and are not etched away with the neutral free radicals in the plasma, the only way to accelerate their removal was to increase the sputter rate. This was accomplished by reducing the pressure, and increasing the RF power. Increasing the RIE power increases the density of the plasma and also increases the DC self-bias, which is responsible for accelerating charged ions to the surface. At a higher DC bias, these ions strike the surface with more energy, which improves the physical sputtering rate of the non-volatile etch products. The only drawback is that physical sputtering is for the most part material independent and, therefore, *all* materials will be sputtered away at a greater rate. This includes the mask used to pattern the SiC, resulting in a reduction of the selectivity between the mask and the SiC, which tends to reduce the anisotropy ratio.

SiC samples etched at a power of 400W (1.25W/cm^2) and a pressure of 6mTorr are shown in Figure 3-9.

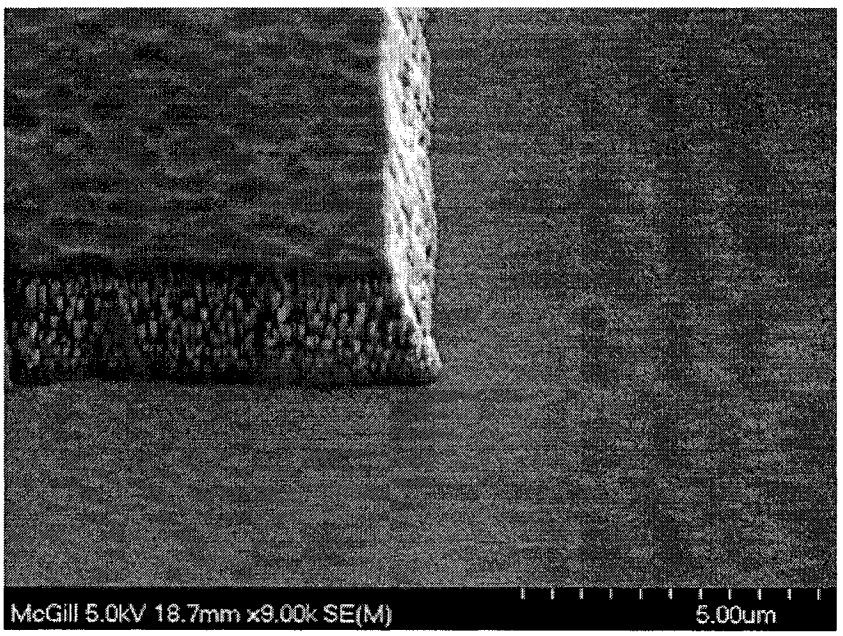

(a)

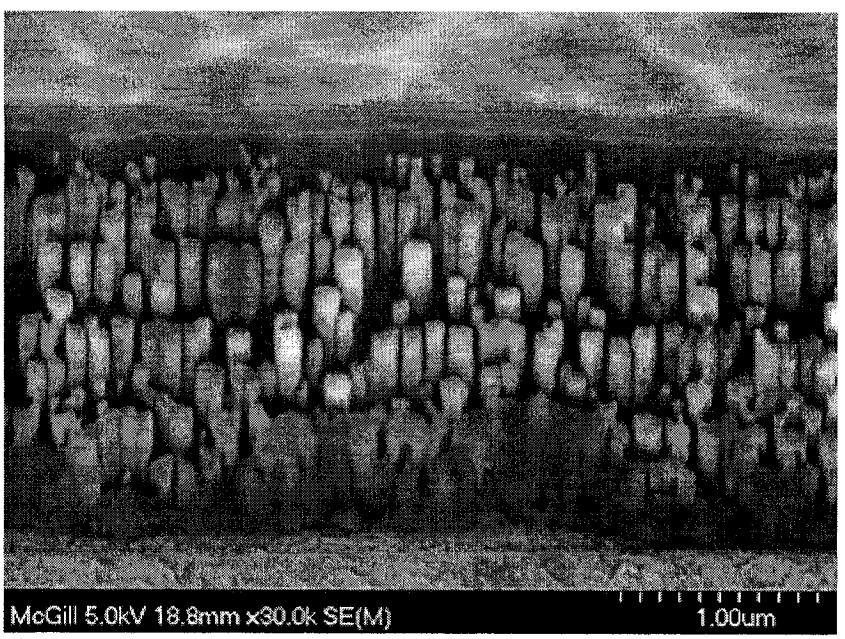

(b)

Figure 3-9: SiC etched at 6mTorr and 400W with an aluminum mask

For these tests, a 2000Å layer of chromium is used under the SiC as an etch stop. As shown in Figure 3-9a, the etch field is now free of residue. Although the higher RIE power helps to mitigate the problem of etch field residue, the devices still possess poor profiles, since the higher power increases the rate of re-deposition on the sidewalls. Figure 3-9b shows a close-up of the etch profile where micro-masking is still clearly visible.

A significant observation, which helped to fix this problem, was that using a chromium etch mask instead of aluminum significantly improved the sidewall quality and reduced the effect of micro-masking. It is believed that this is a result of the lower tendency of chromium to form in-volatile etch products with fluorine. This is supported by the fact that the etch rate of chromium is less than half the etch rate of aluminum in NF_3, even though the sputter yield is higher, indicating that aluminum reacts with fluorine at a much higher rate. The same SiC sample, etched under the same process conditions but with different mask materials, is shown in Figure 3-10.

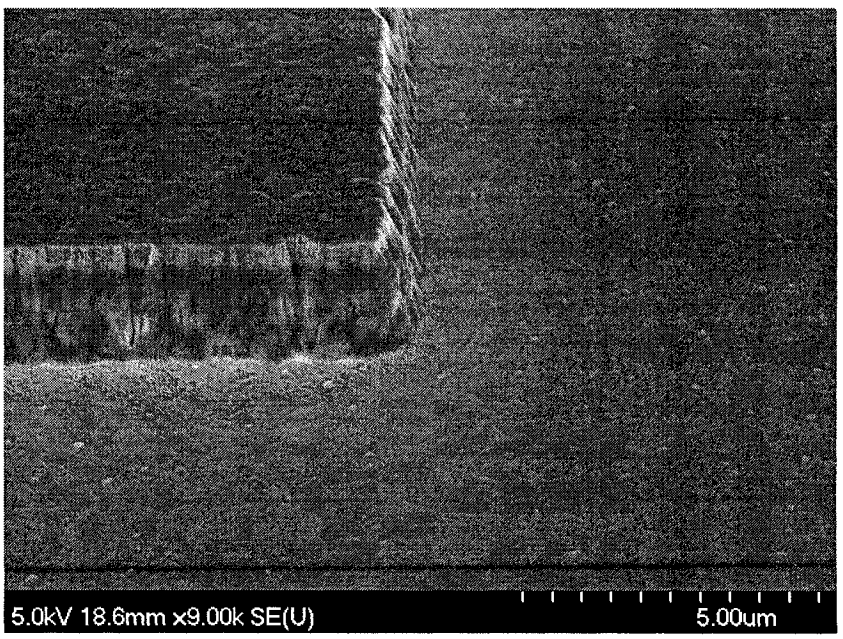

(a)

Figure 3-10: SiC etched at 6mTorr and 400W with a chromium mask

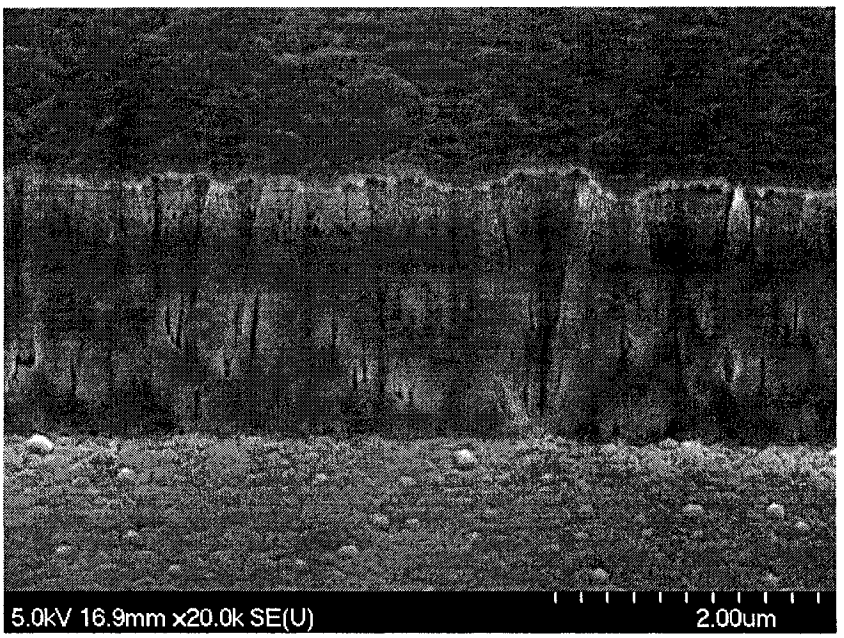

(b)

Figure 3-10: SiC etched at 6mTorr and 400W with a chromium mask (cont.)

In this case there is no residue in the etch field nor on the sidewalls of the device. Compare this to the results obtained with an aluminum mask (Figure 3-9).

To take advantage of this property of chromium, while still enabling the creation of a self-aligned upper metal layer, a novel two-layer metallic mask is proposed. As shown in Figure 3-11, after the deposition of the SiC structural layer, a 2000Å layer of aluminum is deposited followed by a 5000Å layer of chromium.

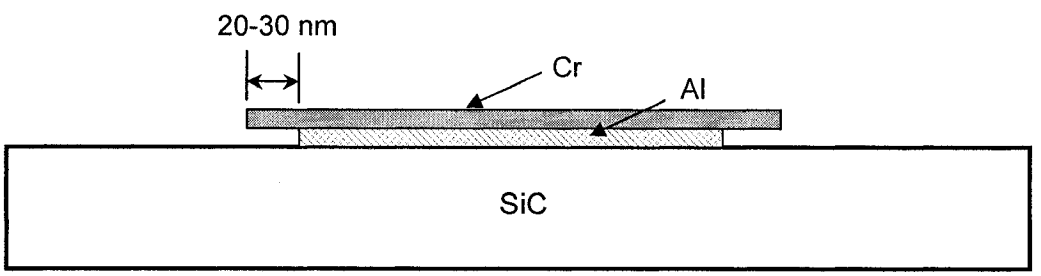

Figure 3-11: Novel bi-metallic masking technique

The chromium layer is first patterned using CR-14 and forms the RIE etch mask for the SiC device layer. The sample is then wet etched using PAN, which does not attack chromium but etches away the aluminum. By timing this process appropriately, the aluminum can be over-etched slightly to undercut the chromium, which ensures that no aluminum is sputtered during RIE. An SEM picture of the final two-layer mask is shown in Figure 3-12. SEM pictures of a SiC sample etched at 400W and 6mTorr using this bi-metallic mask are shown in Figure 3-13 and Figure 3-14. Note that the residue on the sidewall and in the etch-field is completely eliminated. Since no aluminum is exposed to the RIE beam, aluminum micro-masking no longer occurs.

As shown in Figure 3-14, after the RIE etch there typically is a taper in the sidewall profile that leads to a loss of fidelity in the transferred pattern. Ideally, the anisotropy ratio (slope of the taper) should be as high as possible in order to ensure that the device layer has the same dimensions as the mask. This loss in fidelity is primarily due to the erosion of the etch mask, since the SiC etch is performed at a high power. Using the etch recipe developed in this process, the average measured anisotropy ratio was about 4-5:1. Under these conditions, there will be a difference of about 500nm between the dimensions of the top and bottom of the sacrificial layer. For the RF devices in this work, however, this does not pose a significant problem since the typical critical device dimensions are on the order of 10's of micrometers.

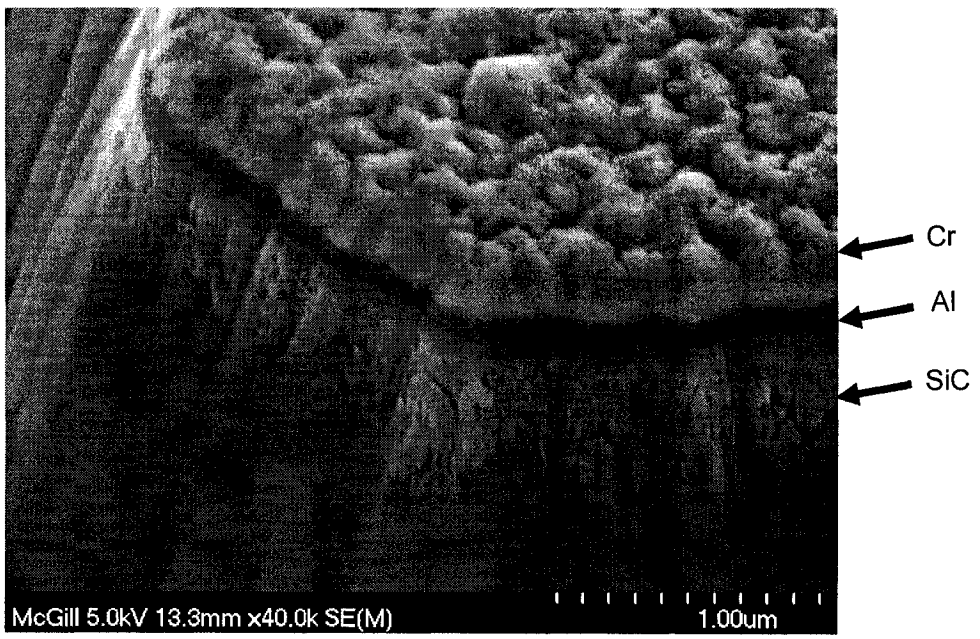

Figure 3-12: Novel bi-metallic mask composed of aluminum and chromium

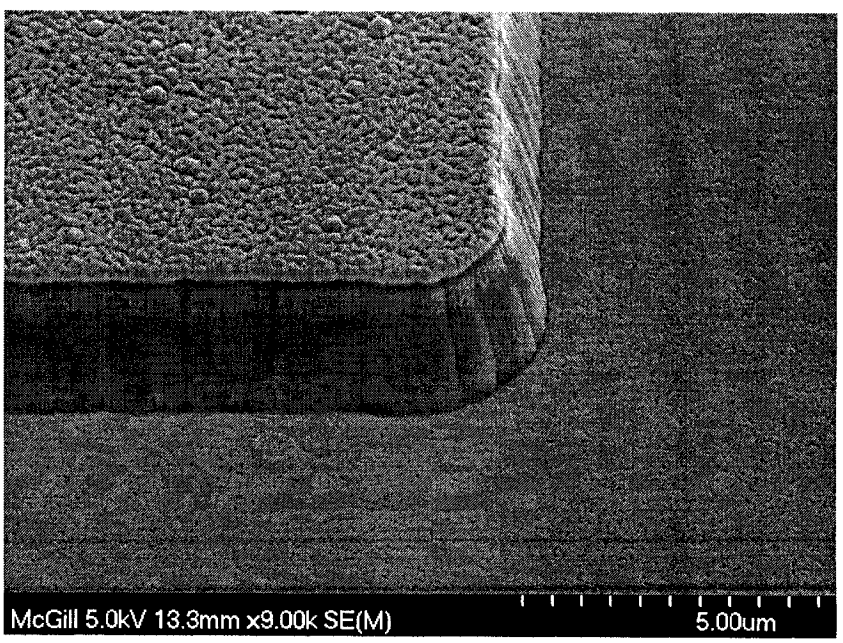

Figure 3-13: SiC sample etched with bi-metallic mask

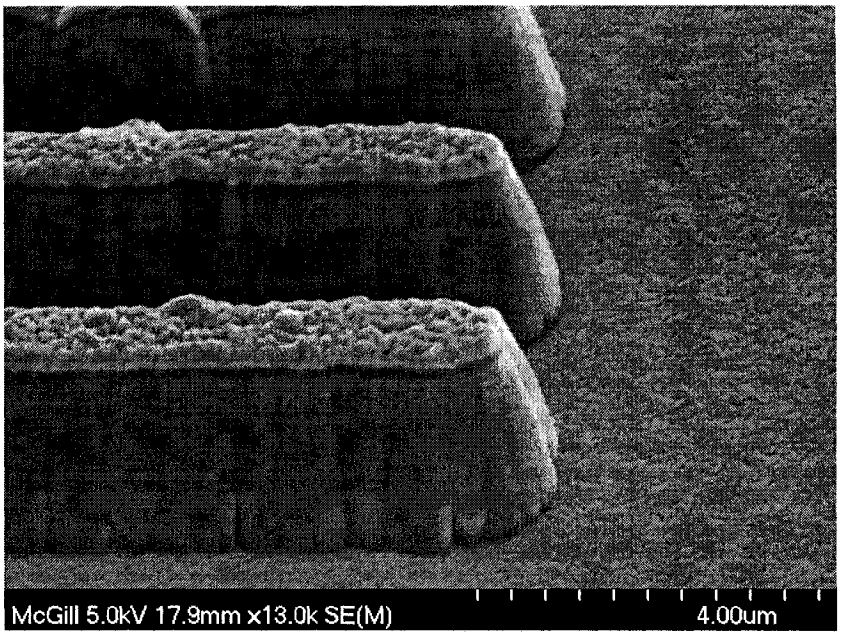

Figure 3-14: 1μm wide SiC lines etched with bi-metallic mask

3.3 INTERCONNECT LAYER

The conducting layers in this process are used to route both RF and DC signals to the MEM devices and thus, must have a low resistivity. Aluminum was selected as the primary conductor for this application since it is widely available, low cost, and is commonly used in IC fabrication. Although materials with a higher conductivity are available such as gold, other factors preclude their use such as a prohibitively high cost, poor adhesion to Si, and the unavailability of simple patterning techniques. Another advantage of aluminum is that it has good adhesion to both silicon and silicon oxide which is crucial to prevent de-lamination during wire-bonding. Moreover, etching of aluminum can be performed using both wet and dry techniques at very low temperatures.

3.3.1 Deposition of Al

Aluminum was deposited using DC sputtering with the same system used to deposit SiC. DC sputtering of metals is commonly used as it has a high deposition rate and stress can be controlled by adjusting the working pressure. The thickness of the conducting layers was

chosen to be 0.25μm to minimize the degradation in the effective stiffness of the resonator as a result of the low Young's modulus of aluminum. This was also the smallest value that would still allow for reliable wire-bonding to the pads of the device. In early fabrication attempts that used thinner metal layers (<0.2μm), wire-bonds to pads was extremely unreliable and would sometimes un-bond during handling of the devices.

Similar to SiC, the residual stress in the deposited films were minimized by varying the working pressure. Since these metal layers are used as electrodes on the SiC structural layer, any significant residual stress will induce warping in the released structures. A plot of the measured stress in 0.2μm DC sputtered aluminum films vs. pressure is shown in Figure 3-15. All tests were performed at a deposition power of 1100W. The measured stress of the aluminum film was tensile for all of the tested deposition pressures, which is typical of most thin metal films [34]. Another observation was that the stress in the metal film tended to reduce slowly even after deposition. Aluminum is a soft metal with a low melting point and thus, the metal film tends to relax even after deposition is over. The minimum stress of about 20MPa was obtained at the highest deposition pressure of 22.5mTorr, which is sufficient to minimize stress-related post-release problems.

The sheet resistance of a 0.25μm aluminum film was measured to be about 150 mΩ/□ using a Tencor M-Gage 300 resistance measurement system. This yields an approximate bulk-resistivity of 3.8 μΩ·cm which is in relative agreement with the well documented bulk value of 2.7 μΩ·cm.

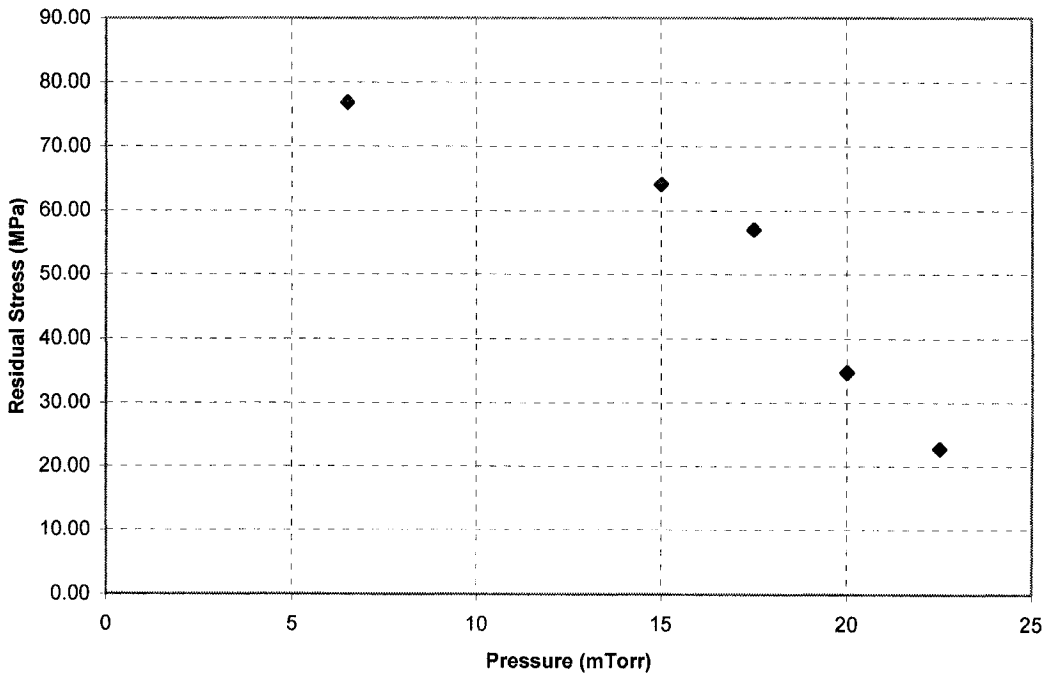

Figure 3-15: Internal stress of deposited aluminum versus working pressure

3.3.2 Etching of Al

Etching of aluminum was performed using a commercially available etchant from Transene, which contains a combination of phosphoric, acetic and nitric acid (PAN). The aluminum was first masked with photo-resist and then etched with PAN at 30°C. At this relatively low temperature, the measured aluminum etch rate was ~100nm/min and under-cut of the resist could be accurately controlled. In general, wet etching cannot be used for small feature sizes, since wet etches are isotropic. With 0.25μm thick films, the measured undercut was about 0.35μm, and thus very small features are removed with this method. In this work, the smallest aluminum features present are about 1.4μm in width (on reticle), which results in an on-wafer size of about 0.7μm. Although sufficient for this work, if high-fidelity pattern transfer is required, a dry RIE using chlorine plasma chemistry should be used instead of wet etching [9].

3.4 SACRIFICIAL LAYER

The sacrificial material is used to create the gap between the structural layer and the actuation electrodes on the substrate. Since different types of RF MEM devices have different requirements, the thickness of this layer should be easily adjusted; for example, resonators require a very tightly-controlled thin gap on the order of 100nm, while inductors ideally require a large gap (>5μm) to reduce coupling to the substrate. Thus, the deposition rate must be accurately controlled, while still being relatively large to reduce processing time. Secondly, this layer must be easily removed using isotropic etching techniques that do not adversely affect the other materials in the device. Wet etchants are commonly used to release MEM devices as they are cost effective and multiple wafers can be easily batch processed. The main drawback is that capillary forces can pull free-standing structures down to the substrate after the wafer is dried. This effect, called *stiction*, can render a large portion of devices inoperable. Another more attractive release method is to use a dry, plasma based etch. Since the etch takes place in a vacuum, no special rinsing and drying procedures to prevent stiction are required after release. In both cases, however, the release step must be highly selective to the sacrificial material and thus, in this work, should not etch either aluminum or silicon carbide. SiC does not etch easily in aqueous solutions and is relatively inert, however, aluminum is readily etched by many commonly used etchants such has hydrofluoric acid (HF). Also, since this process is intended for integration with CMOS, ideally the etchant should be 'oxide compatible' to ensure that the underlying electronics are not damaged by the release step. Thirdly, in this work the sacrificial layer also doubles as the etch stop for the SiC layer and thus must have a low etch rate in fluorine-based plasmas. One of the main difficulties when using SiC, is the lack of a robust etch stop in most processes; for example, the etch rate of SiC when using reactive-ion-etching is usually about the same order of magnitude as for silicon oxide, silicon nitride and poly-silicon. Thus, the etch rate must be tightly controlled in order to prevent damage to underlying layers.

For this work, two different sacrificial layers were investigated: *chromium* and *polyimide*. Chromium is a hard metal that is not readily etched in fluorine plasma (see section 3.2.3.1), and can be removed using wet etching. Polyimide, on the other hand, is a spin-on based

polymer that cures into a hard film, that can be easily removed with a dry etch in oxygen plasma. The development of deposition and etching processes for both of these materials is described in the ensuing section.

3.4.1 Chromium

A chromium sacrificial layer is used as it can satisfy all of the above requirements. First, it can be easily deposited by DC sputtering which is a low temperature process (<100°C) and is commonly used in the IC industry. Using this deposition method, the thickness and deposition rate can be controlled by adjusting available parameters such as power and pressure. Very thin, conformal layers can be created, along with very thick layers. Second, a highly-selective etchant for chromium exists that does not readily etch aluminum, silicon, silicon oxide or silicon carbide. Chromium etchant CR-14s, from Cyantek Co. is a combination of ceric ammonium nitrate and acetic acid, that readily etches chromium, however, etches aluminum at an extremely low rate (unlike many other available chromium etchants). Lastly, chromium is etched very slowly in fluorine-based plasmas and thus, forms a highly resistant etch stop during the RIE of the SiC structural layer.

3.4.1.1 Deposition

The chromium sacrificial layer was deposited using the same DC sputtering system used to deposit SiC. With a source power of 750W, and at a pressure of 25mTorr, both 100nm and 200nm layers were successfully deposited at an effective rate of about ~90nm/min. Since chromium is a hard metal with a high melting point, the residual film stress was measured to be in the order of 300MPa (tensile). Although significant, this layer is only a sacrificial spacer and thus, its material properties are not important to device performance. Similar to aluminum, the film stress was observed to increase with decreasing pressure. With a deposition pressure of 3mTorr the residual stress was measured to be ~1.2GPa.

3.4.1.2 Etching

Wet-etching is used to pattern and remove the sacrificial chrome layer which acts as a spacer between the substrate and the MEM device. For this work, the chrome layer was etched using CR-14 at room temperature.

When used to release fabricated devices, however, the etch rate of the chrome in the narrow gap of the resonator was found to be much too slow. Even after several hours in CR-14, the chrome sacrificial layer would not be completely removed from under the structural layer. After such a long time in the etchant, the aluminum interconnects were also observed to degrade to the point that they became open circuits.

3.4.2 Polyimide

The other sacrificial material investigated was polyimide. Polyimides are special types of polymers that have both excellent chemical resistance and thermal stability. Usually deposited in a spin coating process, the initial solution is composed of a high-molecular weight, polyamic acid precursor dissolved in an NMP solvent system [48]. The spun film is then cured at elevated temperatures, which evaporates any remaining solvent and converts the polyamic acid into its insoluble and highly chemically resistant form. After imidization is complete, these films are mechanically tough and can withstand a number of common solvents and acids, including acetone, isopropyl alcohol, PAN, and CR-14. Thus, this material is suitable for the process described in this work, which contains both aluminum and chrome layers. When used as a sacrificial material, it has many advantages. First, since it is deposited in a spin coating process, the deposition temperature is only limited by the curing step, which can be as low as 200°C [48]. This makes it suitable for a low-temperature, CMOS-compatible MEMS fabrication processes. Second, polyimide films are readily etched in oxygen plasma and thus, devices can be released in a completely dry process which eliminates the need for complex drying procedures. Lastly, the thickness of the layer can be easily adjusted from a few microns all the way down to 100nm by diluting with an appropriate solvent and by changing the spin speed. This allows for great design flexibility, since different types of RF-MEM devices require different gap sizes.

The polyimide used for this work was PI-2555, manufactured by H D Microsystems. This particular type of polyimide has a low imidization temperature (<200°C) and can be readily removed using oxygen plasma. Furthermore, since it is filtered down to 0.2μm, it is ideal for this application, where thin gaps are required.

3.4.2.1 Deposition

A spin-coating process was developed to deposit both ~100nm and ~200nm polyimide films. In order to obtain such thin layers, the PI-2555 was first diluted with T-9039 which is an NMP based solvent available from H D Microsystems. Since most polyimides are not designed to be deposited this thinly (<1μm), the viscosity must be lowered to obtain the desired thickness. A dilution ratio of 4:1 was used to obtain a thickness of 100nm, while 2.5:1 was used to obtain 200nm films. Solutions were typically mixed several days in advance to allow the polyimide to stabilize. Before deposition, wafers were baked at 150°C for 30 minutes to remove any surface moisture which can cause poor adhesion to the substrate. After cooling, 4mL of the polyimide/solvent mixture was dispensed onto a static wafer using a 5mL syringe, and spun at ~2000rpm with low-acceleration (2000rpm/s) for 30s. Slow acceleration of the wafer is important as it allows the film to fully and uniformly cover the surface. Higher ramp rates were observed to severely degrade the uniformity of the coating. After spin-coating, the films were soft-baked at 135°C for 5 minutes to evaporate most of the remaining solvent. This partially cures the film and increases its resistance to both acetone and TMAH based developers. To fully imidize the film, the wafers were then cured in an oven at 300°C. To reduce the chance of cracking, the wafers were first ramped from room temperature up to 200°C at a rate of 4°C/s, and baked for 30 minutes. The temperature was then increased to the final curing temperature of 300°C at 2.5°C/s, and held for one hour. Wafers were then cooled back to room temperature at a controlled rate of 4°C/s. After curing, the polyimide films were observed to be impervious to both acetone and IPA. Also, there was no noticeable etching of the polyimide film after several minutes in both PAN and CR-14 etchants.

Qualification of the polyimide deposition recipe was originally performed on virgin silicon wafers and film thickness measured using a Prometrix SM-150 film thickness mapper. Spin-coating at a speed of 2500rpm with the 4:1 polyimide mixture yielded a cured film thickness of 100±5nm, while spin coating at 1800rpm with the 2.5:1 polyimide mixture yielded a film thickness of 200±5nm. When spin-coating over patterned aluminum features, however, the film tended to planarize the surface and thus the film thickness on the metal electrodes tended to be thinner as shown in Figure 3-16.

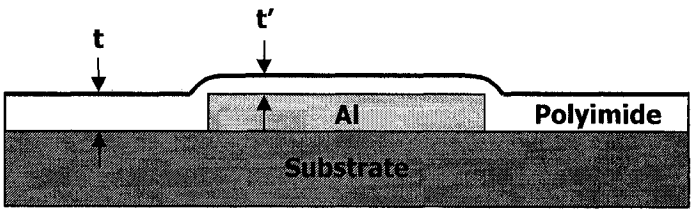

Figure 3-16: Thin layer of polyimide over aluminum electrodes

As a result, multiple coats were required to obtain resonator gap thicknesses in the range of 100-300nm.

3.4.2.2 Etching

Both wet and dry etching techniques for polyimide were explored. After soft-baking, the polyimide film can be patterned using a standard TMAH based photo-resist developer. Thus, after exposure, the photo-resist mask can be developed and the polyimide can be etched in a single step; however, the etch rate of the polyimide is strongly dependent on both the temperature and time of the soft-bake step. This bake is used to partially imidize the films and stabilize the etch rate. After numerous attempts, the etch rate could not be sufficiently controlled to accurately pattern the small features required for this work. Excessive undercut of the resist limited the feature size to greater than a few micrometers.

To improve the etch anisotropy, the sacrificial layer was patterned using a 1.4μm hard-baked photo-resist mask in an oxygen RIE. With a source power of 150W, and a pressure of 100mTorr, the etch rate of the polyimide and resist mask was measured to be about ~300nm/min, and ~400nm/min respectively. Although the etch rate ratio is less than one, the polyimide films are very thin and are removed in less than one minute.

The final release step was also performed using an oxygen plasma; however, instead of RIE the polyimide was isotropically etched using a microwave oxygen plasma asher. Etching was performed at 750mTorr with a source power of 400W for ~ 5 hours. Under these conditions, beams as wide as 40μm could be fully released.

3.5 SUBSTRATE

For RF MEM devices, the substrate should be as insulating as possible to reduce cross-talk between ports of the MEM devices. For the resonators in this work, high resistivity silicon 6" wafers were used (>150Ω·cm), with 2.5μm of thermally grown silicon-oxide. This extra layer helps to reduce the parasitic paths from the input to the output of the device.

3.6 COMPLETE PROCESS OVERVIEW

The complete fabrication sequence is illustrated in Figure 3-17. The core of the process is a sputtered SiC structural layer with multi-layer aluminum metallization for routing electrical signals. Since all steps of this fabrication process are performed at low-temperatures, aluminum interconnects can be deposited and patterned before the structural layer is formed. In total, three separate metal layers are available for routing both RF and DC signals.

All lithography is carried out using 1.4μm of 1813 positive photo-resist which is applied in a spin-coating process similar to that used for polyimide and SOG. Before depositing photo-resist, wafers are baked at 150°C for 30 minutes to remove any moisture from the surface and improve adhesion. This greatly improves the minimum feature size which can be resolved, especially during wet-etching where small patterns were observed to delaminate from the surface. Spin-coating is performed using an automated system at ~4000rpm for 30s. Wafers are then subsequently soft-baked at 115°C for 60s to remove any residual solvent from the resist. All lithographic patterning is carried out using manual alignment with a Canon MIII 5:1 projection mask aligner. After exposure, a bake at 115°C for 60s is used to reduce the standing-wave pattern that is commonly found in the resist profile when using a non-broadband exposure source. The final resist pattern is then developed using a TMAH based developer (MF-319) at room temperature for 60s. Lastly, to improve adhesion during wet etching, the resist is finally hard-baked for 5 minutes at 90°C.

The resonator fabrication process begins with a 150mm high resistivity silicon wafer with 2.5μm of thermally grown oxide (Figure 3-17a). To form the first interconnect layer and the

bottom electrode of the resonator, a 0.25μm aluminum layer is then deposited by DC sputtering at room temperature, and patterned using a PAN wet etch (Figure 3-17b). Next, a thin (~0.1-0.3μm) polyimide layer is deposited which acts as a sacrificial spacer and forms the small gap necessary for the resonator (Figure 3-17c). To provide mechanical support for the suspended structure after release, anchor holes are patterned in the polyimide to expose the underlying substrate. Following the sacrificial layer, the second aluminum metallization is deposited using DC sputtering. This 0.25μm aluminum layer acts as the top electrode of the resonator as shown in Figure 3-17d. The core of the MEM resonator is then formed by DC sputtering 2μm of SiC, followed by 0.25μm of aluminum and 0.6μm of chromium (Figure 3-17f). The aluminum layer is the third level of metallization and is used as a heater for modulating the resonator frequency (this will be described in more detail in Chapter 4). The thicker chrome layer on top acts as a mask during the RIE process that is used to etch the SiC. After etching the structural layer, the chrome etch mask is removed in CR-14 and the MEM resonator is then released using an isotropic O_2 plasma etch leaving the freestanding beam shown in Figure 3-17g.

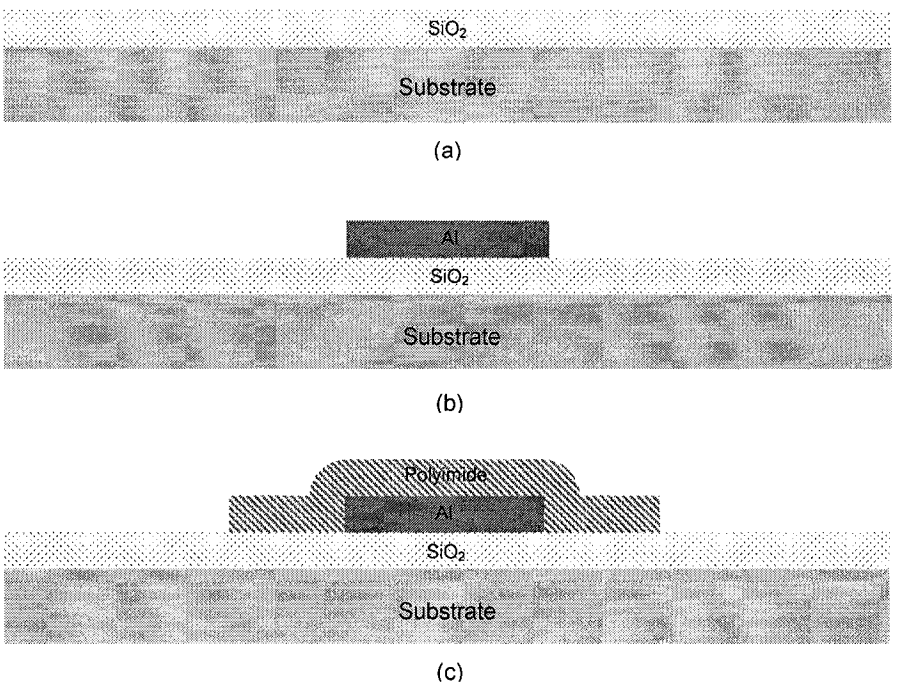

Figure 3-17: Complete process overview

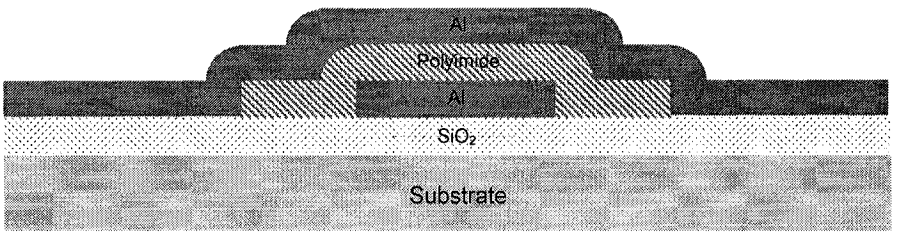

(d)

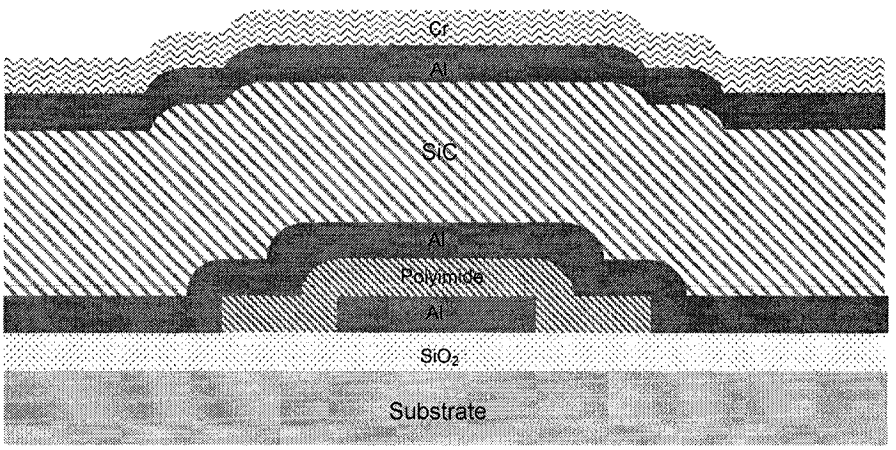

(e)

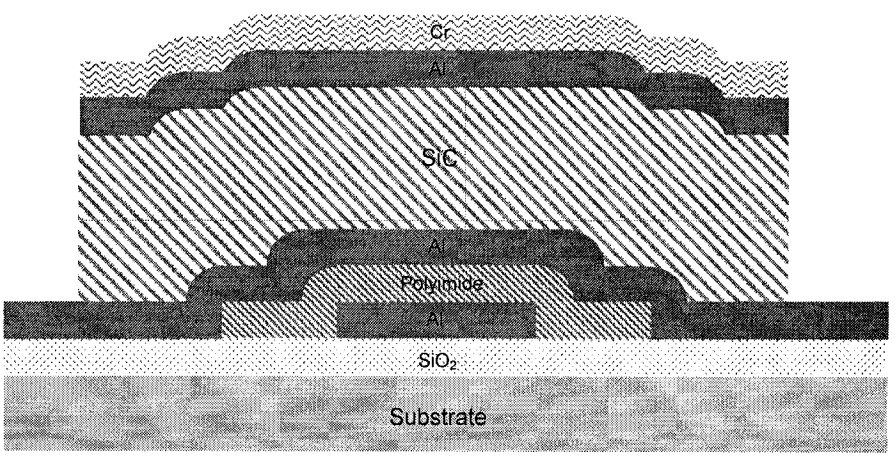

(f)

Figure 3-17: Complete process overview (cont.)

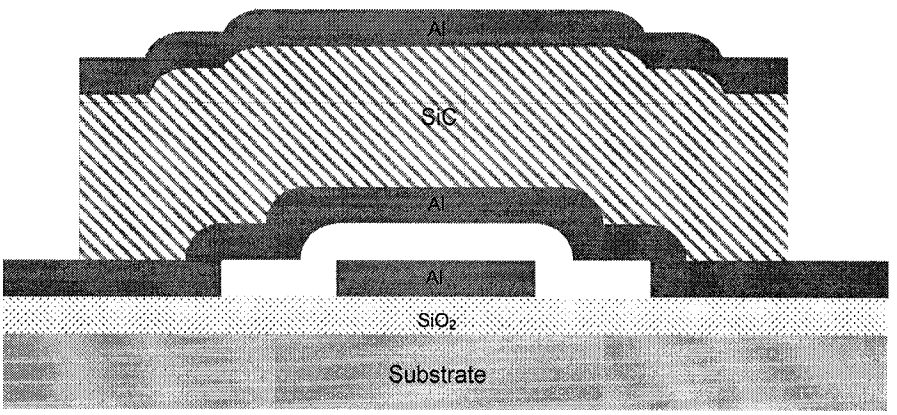

(g)

Figure 3-17: Complete process overview (cont.)

3.7 REFERENCES

[1] D. Gao *et. al,*"Recent progress toward a manufacturable polycrystalline SiC surface micromachining technology," *IEEE Sensors Journal*, vol. 4 (4), pp. 441-448, Aug. 2004.

[2] R. F. Wiser *et. al,* "Polycrystalline silicon-carbide surface-micromachined vertical resonators – Part I: Growth study and device fabrication," *Journal of Microelectromechanical Systems*, vol. 14 (3), pp. 567-578, June 2005.

[3] J. Wang *et. al.*, "1.51-GHz nanocrystalline diamond micromechanical disk resonator with material-mismatched isolating support," *IEEE 17th Annual Conference on Micro Electro Mechanical Systems, 2004 (MEMS '04)*, pp. 641-644, Jan. 2004.

[4] S. Pourkamali *et. al.*, "VHF single crystal silicon capacitive elliptic bulk-mode disk resonators – Part II: Implementation and Characterization," *IEEE Journal of Microelectromechanical Systems*, vol. 13 (6), pp. 1054-1062, Dec. 2004.

[5] E. Quevy *et. al.*, "Ultimate technology for micromachining of nanometric gap HF micromechanical resonators," *IEEE 16th Annual Conference on Micro Electro Mechanical Systems, 2003 (MEMS '03)*, pp. 157-160, Jan. 2003.

[6] J. Wang *et. al.*, "1.156-GHz self-aligned vibrating micromechanical disk resonator," *IEEE Transactions on Ultrasonics, Ferroelectrics, and Frequency Control,* vol. 51 (12), pp. 1607-1628, Dec. 2004.

[7] F. D. Bannon *et. al.*, "High-Q HF microelectromechanical filters," *Journal of Solid-State Circuits*, vol. 35, no. 4, pp. 512-526, April 2000.

[8] R. F. Wiser *et. al.*, "Polycrystalline silicon-carbide surface-micromachined vertical resonators – Part I: Growth study and device fabrication," *IEEE Journal of Microelectromechanical Systems*, vol. 13 (3), pp. 567-578, Jun 2005.

[9] M. J. Madou, Fundamentals of Microfabrication, 2nd ed., CRC Press, 2000.

[10] P. J. French. "Development of surface micromachining techniques compatible with on-chip electronics," *J. Micromech. Microeng.*, vol. 6, pp. 197-211, Mar. 1996.

[11] A.E. Franke, D. Bilic, D.T. Chang, P.T. Jones, T.-J. King, R.T. Howe, and G.C. Johnson, "Post-CMOS integration of germanium microstructures," *MEMS*, pp.630-37, 1999.

[12] V.T. Srikar *et. al.*, "Materials selection in micromechanical design: an application of the Ashby approach," *Journal of Microelectromechanical Systems*, vol. 12 (1), pp. 3-10, Feb 2003.

[13] M. Gad-el-Hak, The MEMS Handbook, CRC Press, 2002.

[14] C. Stoldt *et. al.*, "A low temperature CVD process for silicon carbide MEMS," *Sensors and Actuators A*, vol. 97-98, pp. 410-415, 2002.

[15] E. Hurtos, J.Rodriguez-Viejo, "Residual stress and texture in poly-SiC films grown by low-pressure organometallic chemical-vapor deposition," *J. Appl. Phys.*, vol. 87 no. 4, pages 1748-1758, 2000.

[16] S. Roy et. al., "Fabrication and characterization of polycrystalline SiC resonators," *IEEE Transactions on Electron Devices*, vol. 49 (12), pp. 2323-2332, Dec 2002.

[17] T. Rajagopalan *et. al.*, "Low temperature deposition of nanocrystalline silicon carbide films by plasma enhanced chemical vapour deposition and their structural and optical characterization," *Journal of Applied Physics*, vol. 94 (8), pp. 5252-5260, Oct. 2003.

[18] P. Sarro. "Silicon carbide as a new MEMS technology," *Sensors and Actuators A*, vol. 82, pp. 210-218, 2000.

[19] A. F. Flannery *et. al.*, "PECVD silicon carbide as a chemically resistant material for micromachined transducers," *Sensors and Actuators A*, vol. 70, pp. 48-55, 1998.

[20] P. M. Sarro *et. al.*, " Low-stress PECVD SiC thin films for IC-compatible microstructures," *Sensors and Actuators A*, vol. 67, pp. 175-180, 1998.

[21] N. Ledermann et. al., "Sputtered silicon carbide thin films as protective coating for MEMS applications," *Surface and Coatings Technology*, vol. 125, pp. 246-250, 2000.

[22] Li Gou *et. al.*, "SiC film deposition by DC magnetron sputtering," *Thin Solid Films*, vol. 345, pp. 42-44, 1999.

[23] A.K. Costa *et. al.*, "Properties of amorphous SiC coatings deposited on WC-Co substrates," *Materials Research*, vol.6 (1), pp.39-42, 2002.

[24] A. K.Costa *et. al.*, "Characterization of ultra-hard silicon carbide coatings deposited by RF magnetron sputtering," *Thin Solid Films*, vol. 377-378, pp. 243-248, 2000.

[25] M.Tenhover *et. al.*, "DC-magnetron sputtered silicon carbide," *Mat. Res. Soc. Symp.*, Vol. 356, pp. 227-232, 1995.

[26] W. Boecker *et al.*, "Sintered silicon carbide/graphite/carbon composite ceramic body having ultrafine grain microstructure," USA Patent 4525461, 1985.

[27] D. Gao *et. al.*, "High modulus polycrystalline 3C-SiC technology for RF MEMS," *Proceedings of the 12th International Conference on Solid State Sensors, Actuators and Microsystems*, Boston, pp. 1160-1163, June 2003.

[28] H. O. Pierson, Handbook of Carbon, Graphite, Diamond, and Fullereness Properties, Processing and Applications, Noyes Publications, 1993.

[29] J. Sellers, "Resolving carbon sputter issues" MKS Technical Note, http://www.mksinst.com/eni-rcsi-TN.html, 2006.

[30] J. Sellers. "Asymmetric bipolar pulsed DC: the enabling technology for reactive PVD," *Surface and Coatings Technology 98,* pp. 1245-1250, 1998.

[31] G. Selwyn *et. al.*, "Particle contamination formation in magnetron sputtering processes," *J. Vac. Sci. Technol. A,* vol. 15 (4), pp. 2023-2028, Jul./Aug. 1997.

[32] L. Zhou, V. Audurier, P. Pirouz, "Chemomechanical polishing of silicon carbide," *Journal of the Electrochemical Society*, vol. 144 (6), pp. L161-L163, 1997.

[33] M. Ohring, Materials Science of Thin Films, Academic Press, 2002.

[34] J. A. Thornton, "Stress-related effects in thin films," *Thin Solid Films*, vol. 127 (1), pp. 5-31, 1989.

[35] P. H. Yiu *et. al.* "A review of RIE reactive ion etching in fluorinated plasmas," *Physica status solidi. B*, vol. 202 (2), pp. 604-642, 1997.

[36] G. F. McLane and J. R. Flemish, "High etch rates of SiC in magnetron enhanced SF6 plasmas," *Applied Physics Letters*, vol. 68 (26), June 1996.

[37] G. McDaniel et. al, "Comparison of dry etch chemistries for SiC," *J. Vacuum Science Technology A*, vol. 15 (3), pp. 885-889, May 1997.

[38] A. Tasaka et. al.,"Plasma etching of SiC surface using NF3," *J. Vacuum Science Technology A*, vol. 20 (4), pp. 513-518, Jul/Aug 2002.

[39] J. B. Casady *et. al.*, "Etching of 6H-SiC and 4H-SiC using NF_3 in a reactive ion etching system," *J. Electrochem. Soc.*, vol. 143 (5), pp. 1750-1753, May 1996.

[40] P. Chabert et. al.,"Reactive ion etching of silicon carbide in SF6 gas: detection of CF, CF2 and SiF2 etch products," *Applied Physics Letters*, vol. 79 (7), pp. 916-919, Aug 2001.

[41] L. Jiang and R. Cheung, "Inductively coupled plasma etching of SiC in SF6/O2 and etch-induced surface chemical bonding," *Journal of Applied Physics*, vol. 93 (3), pp. 1376-1383, Feb 2003.

[42] A. Fleishman et. al.,"Etching of 3C-SiC using CHF3/O2 and CHF3/O2/He plasmas at 1.75 Torr," *Journal of Vacuum Science and Technology*, vol. 16 (2), pp. 536-539, Mar/Apr 1998.

[43] R. Padiyath, et. al.,"Reactive ion etching of monocrystalline, polycrystalline, and amorphous silicon carbide in CF4/O2 mixtures," *Applied Physics Letters,* vol. 58 (10), pp. 1053-1055, Mar 1991.

[44] P. H. Yih and A. J. Steckl, "Effects of hydrogen additive on obtaining residue-free reactive ion etching of β-SiC in fluorinated plasmas," *J. Electrochem. Soc.*, vol. 140 (6), pp. 1813-1824, June 1993.

[45] J. Sugiura et. al., "Reactive ion etching of SiC thin films using fluorinated gases," *J. Vacuum Science Technology B*, vol. 4 (1), pp. 349-354, Jan/Feb 1986.

[46] S. Tanaka *et. al,* " Deep reactive ion etching of silicon carbide," *Journal of Vacuum Science & Technology B: Microelectronics and Nanometer Structures*, vol. 19 (6), pp. 2173 -2176, Nov. 2001.

[47] Material Safety Datasheet for CR-14, Cyantek Corp., 2005.

[48] Datasheet for PI-2555, H D Microsystems, 2001.

Chapter 4 MEM Resonators Fabrication and Testing

This chapter provides a description of the RF-MEM resonator designs that have been successfully fabricated using this process, and presents both simulated and measured test results. Several common flexural-mode structures were built including clamped-clamped beams with different widths, lengths, and electrode shapes. A novel tunable resonator structure is also presented which uses the top metal layer as a simple resistor to alter the resonant frequency. This resistance acts as an integrated heater that can be used to independently tune the resonator by exploiting the temperature dependence of the Young's modulus and thermally induced stress.

To test these fabricated devices, a custom built vacuum system and electrical interface was assembled to allow measurement at pressures as low as 1mTorr. Completed wafers were first diced into separate 4mm by 4mm dies, and then bonded into 28-pin LCC ceramic packages. The S21 of the MEM resonators were then measured using a VNA to determine the Q-factor and frequency of the resonant structures.

The ensuing sections provide a detailed description of the measurement setup and devices that were fabricated using the SiC process described in Chapter 3. Both DC and RF measurements of devices are provided along with a discussion of measured results.

4.1 FABRICATED DEVICES

SiC beam resonators were fabricated with polyimide sacrificial layers, with thicknesses ranging from 100nm to 300nm. For each case, several different device geometries were evaluated with varying lengths, widths and electrode shapes. The following section provides

a summary of the beam designs that were successfully fabricated, along with theoretical performance parameters calculated using the equations given in chapter 2. To verify the analytical formulas, simulation of the mode-shape and frequency was also performed using ANSYS [1].

4.1.1 Standard clamped-clamped beam

Shown in Figure 4-1 is the generalized layout of the standard clamped-clamped (CC) beam resonators fabricated in this work.

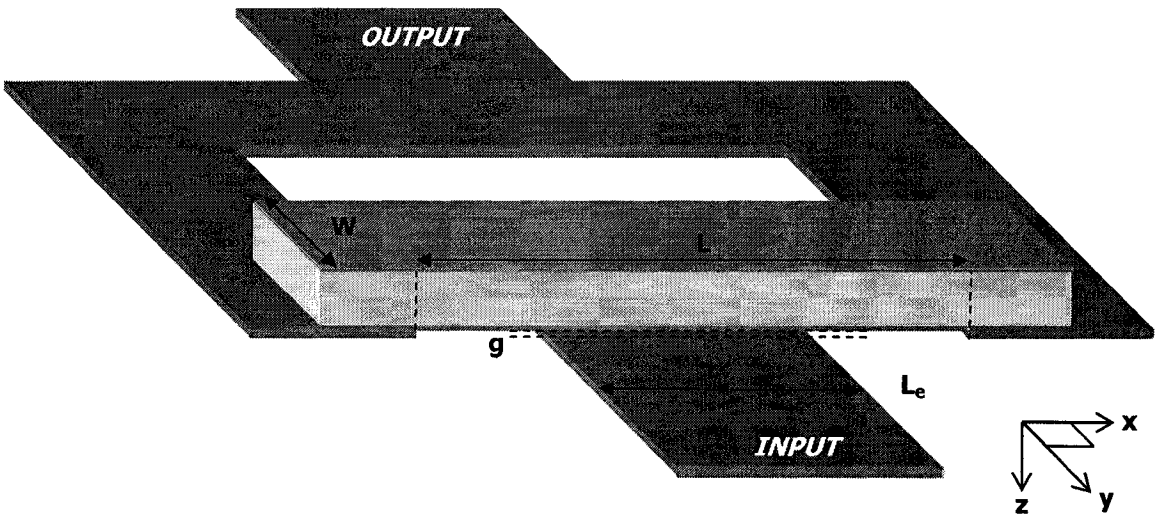

Figure 4-1: Standard clamped-clamped beam design

The device consists of two bond pads, labeled *input* and *output,* connected to the micromechanical beam which is a tri-layer composite of 2μm of SiC deposited between two 0.25μm layers of aluminum (see Figure 3-17g). The bottom aluminum layer is used to route signals from the beam to the output pad, where it is wire-bonded to the package leads. Another separate aluminum layer is used to create the input bond-pad and the bottom electrode.

These CC beams are designed to resonate in their fundamental mode with a frequency that depends on the inverse square of the beam length (*L*). Shown in Figure 4-2 is a plot of the

fundamental mode shape of a 64μm long composite SiC beam simulated with ANSYS. In this plot the displacement is normalized to unity, with the maximum occurring at the center of the beam as expected. The simulated resonant frequency of 4.95MHz corresponds well with the theoretical value of 4.93MHz calculated using the analytical formula (Eq. 2.18). For this simulation, the Poisson ratio for polycrystalline SiC was used, since the elastic properties of amorphous SiC are not readily available; however, given that the frequency of narrow beams are not strongly dependent on the Poisson ratio, these simulations are still expected to yield a good estimate of the resonant frequency.

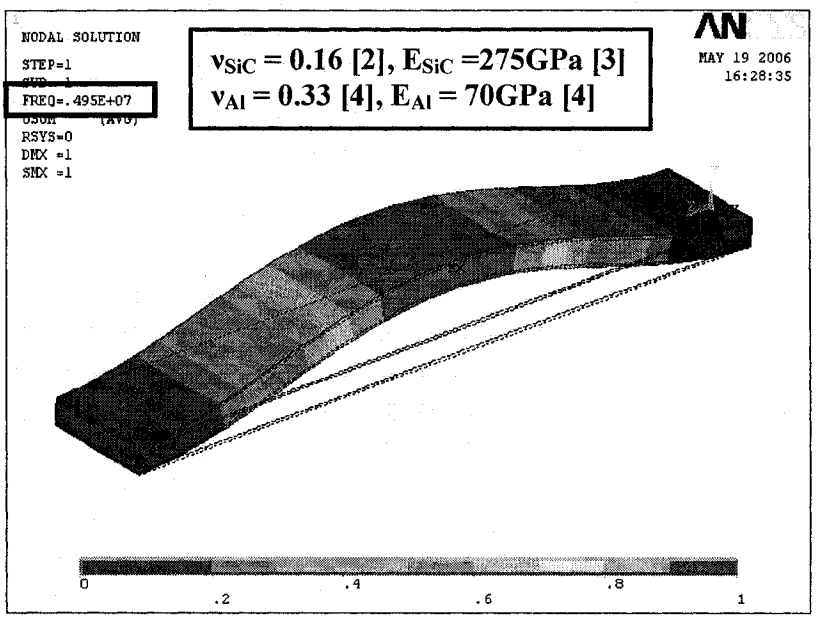

Figure 4-2: ANSYS simulation of the fundamental mode of a 5MHz SiC resonator

Standard clamped-clamped beam resonators were fabricated with a width (W) of 10μm, and lengths (L) of 64μm, 45μm, 37μm, 32μm, and 26μm, which correspond to resonant frequencies of approximately 5MHz, 10MHz, 15MHz, 20MHz, and 30MHz, respectively. The bottom electrode of the resonator was made as wide as possible (L_e) to maximize capacitive coupling between the input and output ports. In all designs, the width of this electrode was chosen to be about 10μm smaller than the beam length to ensure that possible misalignments between subsequent photolithography steps would not short circuit the input and output ports. To increase the power-handling of the devices, several other variations

were also built with beam widths of 40μm, which increases the electrode/beam overlap areas. This results in a greater total output current, and allows for higher drive voltages before the beam starts to enter its highly non-linear regime which is characterized by Duffing distortion and erratic behavior (see section 2.5). The main drawback of having such a wide beam is that the etch time for removing the sacrificial layer can exceed several hours.

Shown in Figure 4-3 are SEM pictures of several fabricated beams based on the geometry illustrated in Figure 4-1.

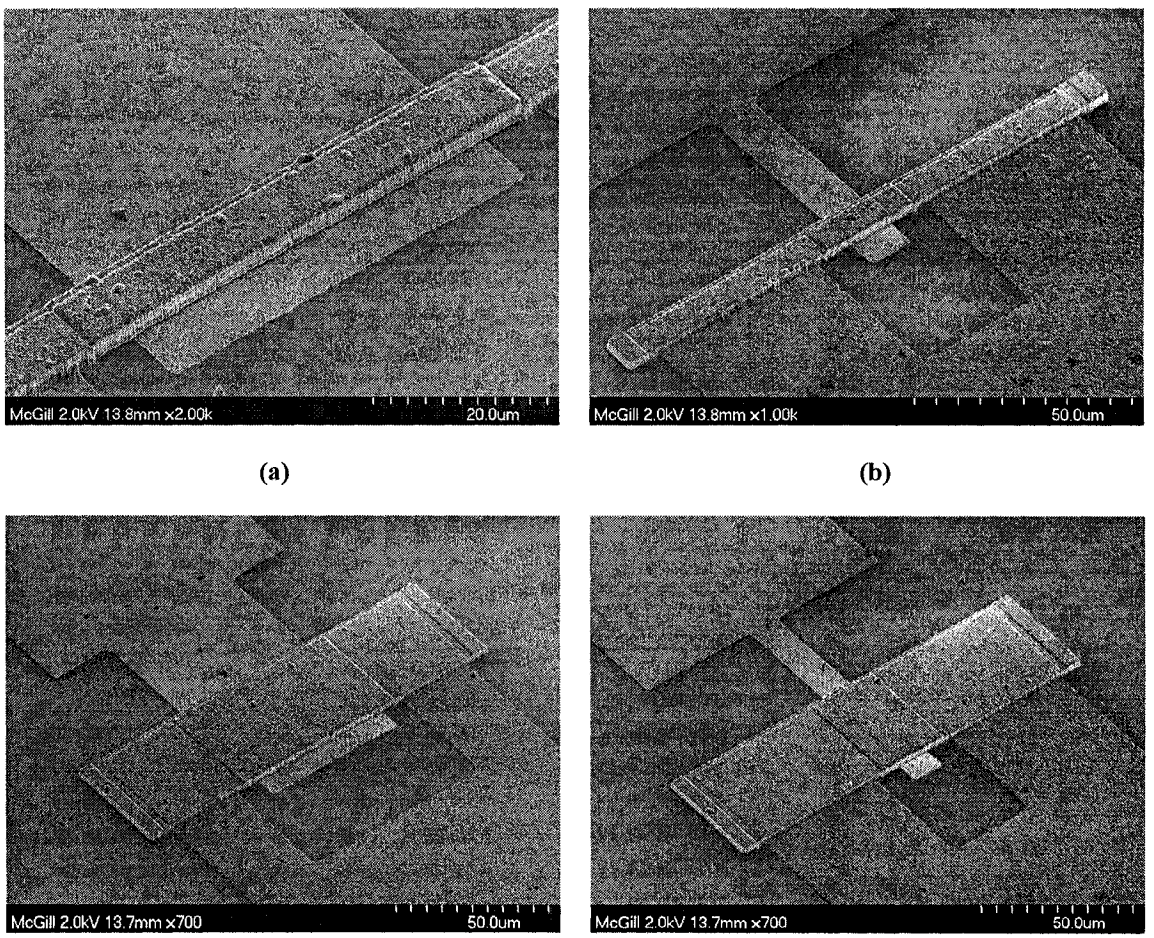

Figure 4-3: Fabricated standard CC beam resonators (a) 10μm wide, 5MHz; (b) 10μm wide, 30MHz; (c) 40μm wide, 5MHz; (d) 40μm wide, 30MHz

The visible residue on the substrate surface is from the RIE etch of the silicon carbide structural layer. As previously discussed in chapter 3, these deposits are a result of the surface nodules present on the SiC film. This residue, however, is relatively sparse and is not expected to interfere with proper operation of the MEM resonators.

4.1.2 Standard clamped-clamped beam with electrode shaping

Another variation of the standard design uses shaped electrodes to help isolate the fundamental mode of the beam, while suppressing other higher-order resonant peaks. As explained in detail is section 2.4, unwanted spurious modes can be eliminated by varying the width of the input electrode along the length of the beam. To effectively select only a single mode, the electrode thickness along the length of the resonator should be proportional to the desired mode's eigenfunction. If this is the case, the electromechanical transduction coefficient (η) will be zero for all modes *except* the one that is desired because of the orthogonal property of mode-shapes (see Eq. 2.64).

In order to selectively excite and detect the fundamental mode of the MEM resonator, both 10μm and 40μm wide beams were fabricated with electrodes that were shaped proportional to the fundamental mode shape. SEM pictures of standard CC-beam resonators with shaped electrodes are shown in Figure 4-4.

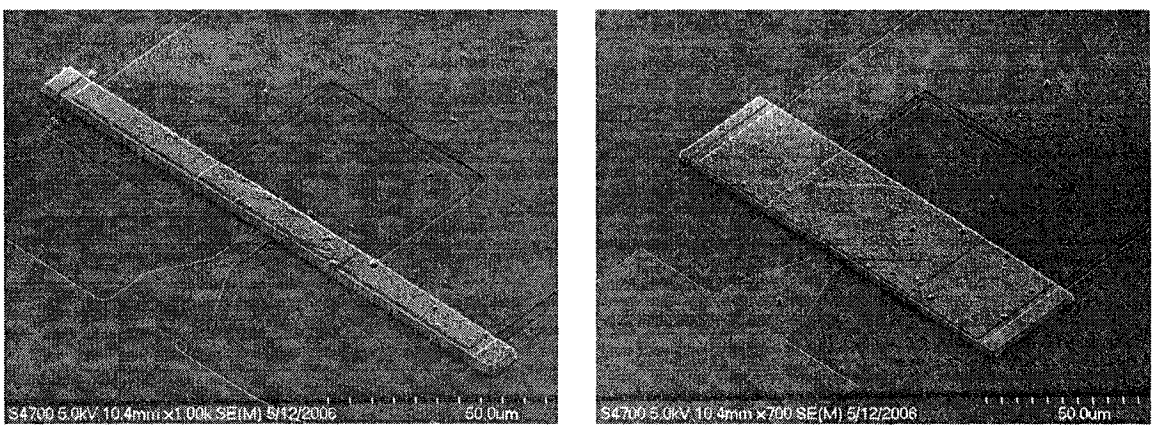

(a) (b)

Figure 4-4: SEM pictures of standard CC-beam resonators with shaped electrodes (a) 10MHz, 10μm wide; (b) 5MHz, 40μm wide

4.1.3 Standard clamped-clamped beam with integrated heaters

Standard clamped-clamped beam resonators were also fabricated with integrated heaters to tune the resonant frequency by exploiting the change in the Young's modulus with temperature. The layout for these designs is shown in Figure 4-5. The design is exactly the same as that of the standard CC-beam beam resonators except that the top metal layer is now connected to a DC voltage source (V_{HEAT}). The resulting DC current (I_{HEAT}) heats up the beam and can be used to tune the resonant frequency. Since the SiC structural layer is semi-insulating, this extra DC tuning voltage does not affect the capacitive transduction between the RF input and output ports, and can be used to independently tune the frequency.

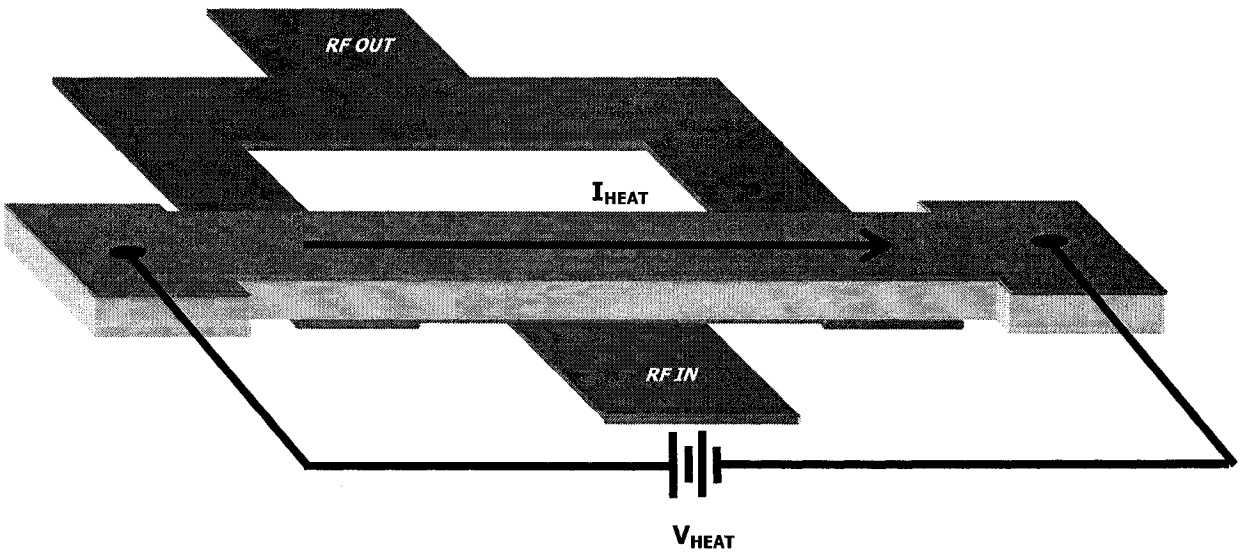

Figure 4-5: Standard clamped-clamped beam design with integrated heater

SEM pictures of fabricated devices with integrated heaters are shown in Figure 4-6.

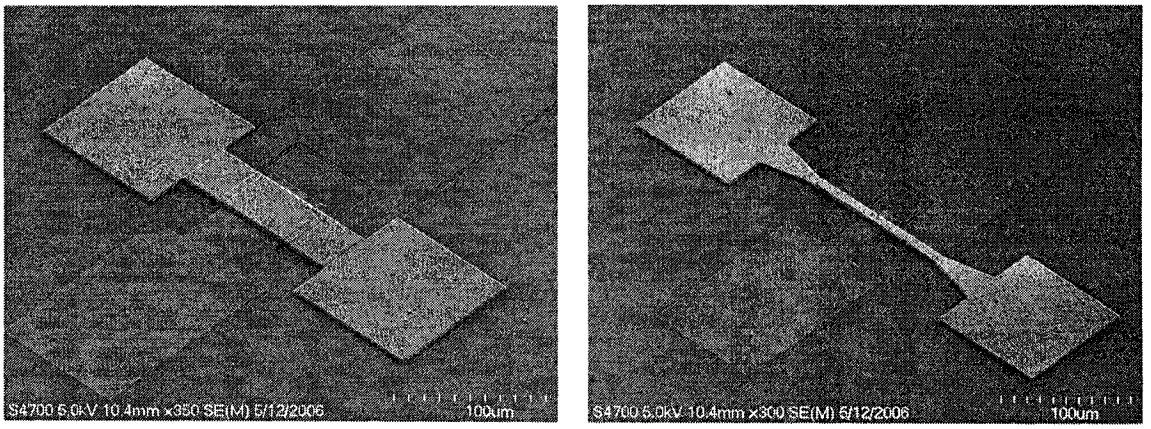

(a) (b)

Figure 4-6: SEM pictures of standard CC-beam resonators with integrated heaters (a) 5MHz, 40μm wide; (b) 30MHz, 10μm wide

The magnitude of the tuning range depends on a number of different factors, including the temperature coefficient of the Young's modulus for the SiC and aluminum layers, along with the degree of thermal expansion which will induce a compressive stress in the constrained beam. As shown in Eq. 2.18 the resonant frequency will depend on both the stiffness and residual stress, which are both a function of temperature. The frequency of the fundamental mode can therefore, be rewritten as

$$f_1(T) \approx \frac{3.56}{L^2}\sqrt{\frac{\bar{D}(T)}{\bar{m}}}\cdot\left(1+0.0246\frac{\bar{N}(T)\cdot L^2}{\bar{D}(T)}\right)^{1/2} \qquad \text{Eq. (4.1)}$$

Both the stiffness of the beam (D) and the thermally generated force (N) are a function of temperature, and therefore the resonant frequency will also be affected. Since the Young's modulus of SiC has a negative temperature coefficient [3], the resonant frequency will tend to decrease with increasing temperature.

4.2 MEASUREMENT OF RESONATOR GAP THICKNESS

Resonators were successfully fabricated with gap thicknesses of 200nm and 300nm. The thinner gap was created by initially spin-coating the wafer with 200nm of polyimide, and

then a second coat of 100nm. The first polyimide layer tended to planarize the surface and the bottom electrode, which resulted in a greater thickness on the substrate than on the aluminum pads. Since the polyimide thickness is on the same order as that of the electrode thickness, film coverage tended to be poor with only one coat. To ensure that the bottom electrode surface and edges were completely covered, a second coat of 100nm was subsequently deposited on top. From SEM photographs, the overall gap height between the top and bottom electrode was estimated to be about 200±20nm. Initial fabrication attempts without the second coat consistently yielded resonators that would short circuit at very low bias voltages, indicating that the top and bottom electrodes were in contact with each other. Similarly, for gaps smaller than 200nm, the device yield was observed to drop dramatically. Again, evidence suggests that this is a result of poor coverage of the bottom electrode. One way to reduce this effect in future fabrication attempts may be to make the electrode thinner; however, this will also increase the parasitic series resistance of the resonator. A second wafer was also fabricated with two separate 200nm coats of polyimide. In this case the measured gap thickness obtained was about 300±30nm.

Upon closer examination of the released devices, it became evident that the fluorine-based plasma used to etch the SiC structural layer was modifying the underlying polyimide sacrificial layer and making it very difficult to remove in oxygen plasma. The result was significant residue on the substrate surface and also in the gap of the resonator. Due to the variation of the etch rate across the wafer, the SiC is over-etched slightly to ensure that it is completely removed on all dies; as a result, the polyimide is also exposed to the NF_3 plasma for a short period of time. A commonly observed effect when etching polyimide with fluorinated plasmas is the formation of involatile etch residue due to the fluorination of the polyimide surface [5][6]. A consequence of this is that the sidewalls of the etched polyimide tend to become passivated. Since the reactive-ion etching process is highly directional, this vertical passivation layer remains, as it is not exposed to ion bombardment from the plasma. Shown in Figure 4-7 are SEM photographs of the gap of a released MEM resonator that has been over-etched in NF_3. Figure 4-7(a) shows an isometric view of the side of a MEM resonator, with close-in views of two select areas shown in Figure 4-7(b) and (c). Note that the resonator gap in this case is blocked by a fluorinated, polyimide 'skirt' that holds the

resonator in place. After some investigation, it was observed that the polyimide *under* the SiC was completely removed and only this thin skirt remained. This suggests that it is a passivation mechanism which modifies only the sidewall of the polyimide as it is etched down in the NF_3 plasma. Even after extended periods in oxygen plasma, this fluorinated passivation layer could not be removed.

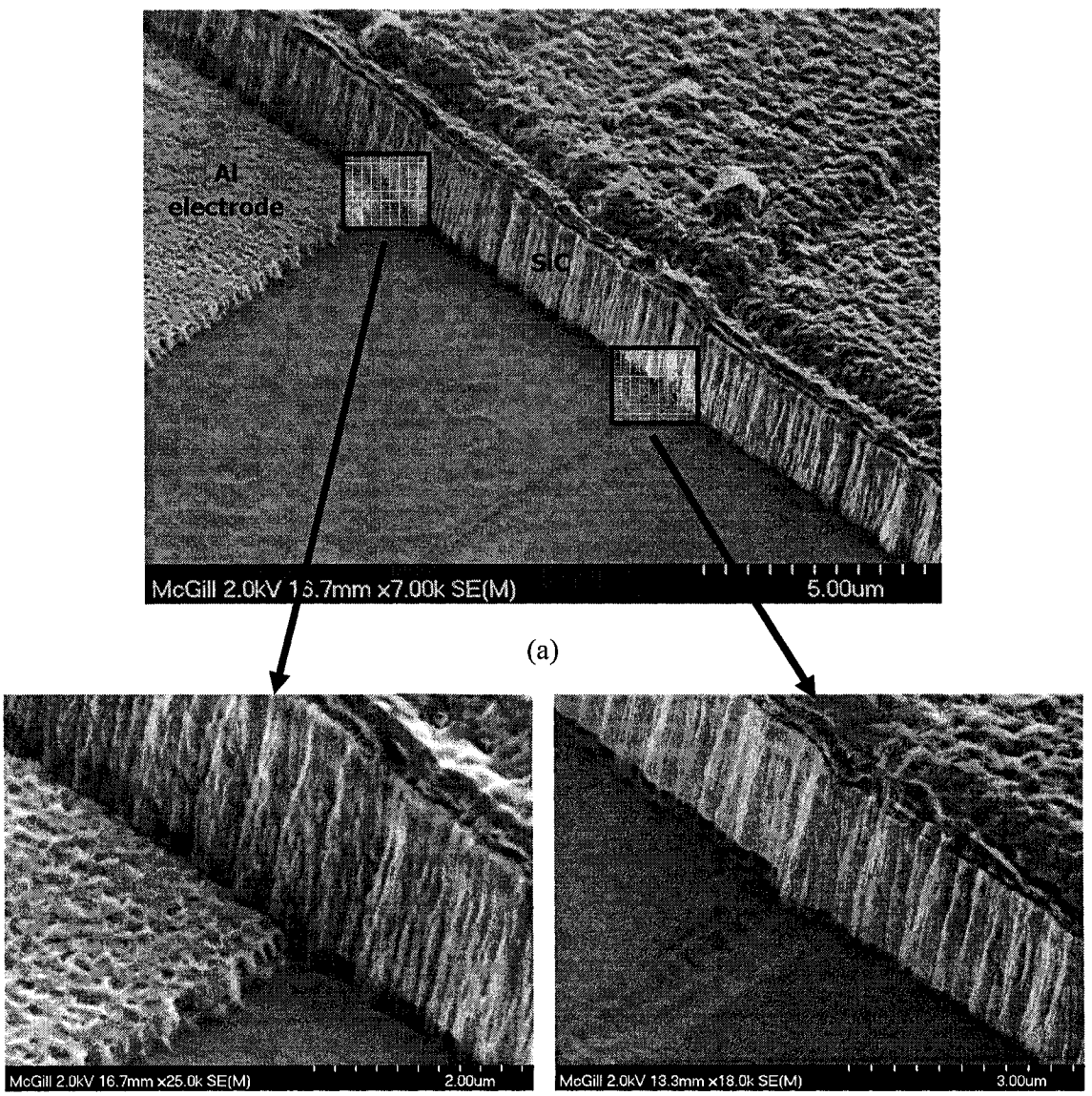

Figure 4-7: SEM pictures a released resonator gap showing the effect of polyimide fluorination

In an attempt to prevent this effect, the over-etch time of the SiC was reduced and carefully timed to limit the exposure of the polyimide to the fluorinated plasma; however, there was still significant polyimide residue on the surface which could not be removed, even after several hours in oxygen plasma. Shown in Figure 4-8 is a SEM photo of a resonator with a 300nm gap obtained by carefully timing the SiC etch. Note that, although there is no residue in the gap, there is still significant residue on the etch surface.

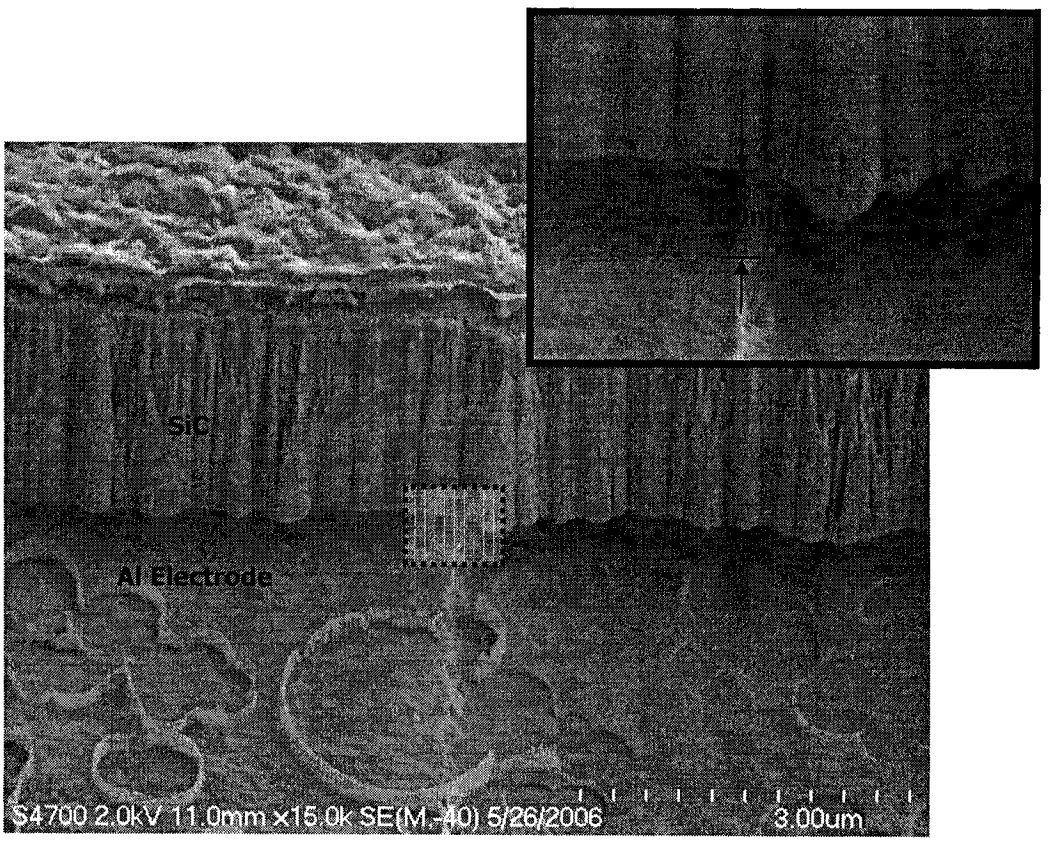

Figure 4-8: SEM of SiC resonator with a residue-free 300nm gap

Fabrication of residue-free gaps smaller than 300nm was very difficult as they became increasingly more prone to residue. The smaller polyimide thickness meant that they could tolerate limited etching in NF_3 before forming a fluorinated skirt, locking the resonator in place. Moreover, the yield of working devices was very small.

To help alleviate the problem of polyimide fluorination during the SiC etch, the fabrication process was slightly modified by depositing a thin layer of chrome (90nm) over the polyimide sacrificial layer. A cross-section of a resonator using this modified process flow is shown in Figure 4-9.

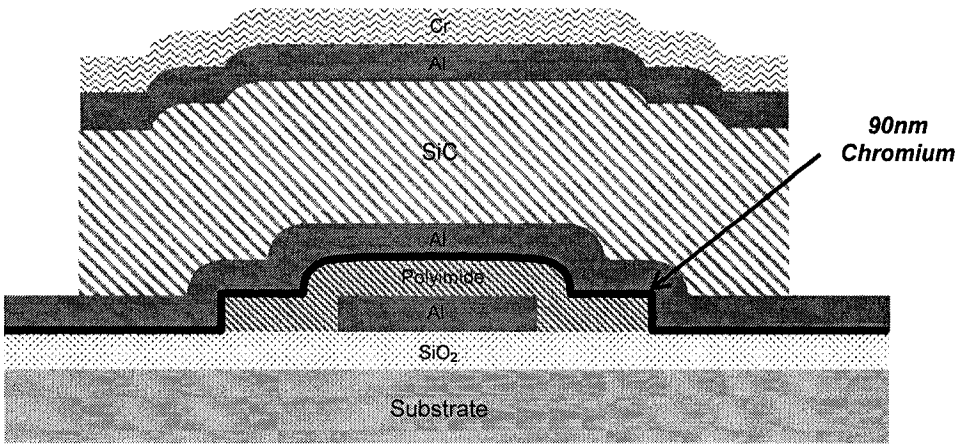

Figure 4-9: Resonator cross-section built with modified process

Since chrome is not readily etched by NF_3 it provides a robust etch stop during the RIE of the SiC structural layer, and thus no polyimide is exposed to the fluorine plasma. No other additional steps are needed since this protective chrome layer is also removed in the CR-14 wet etch used to remove the RIE mask. Moreover, since the chrome layer is very thin, the added chrome did not significantly affect the resonant frequency of the devices.

Shown in Figure 4-10 is a SEM picture of a 10MHz resonator, with 200nm gap clearly showing a residue free surface.

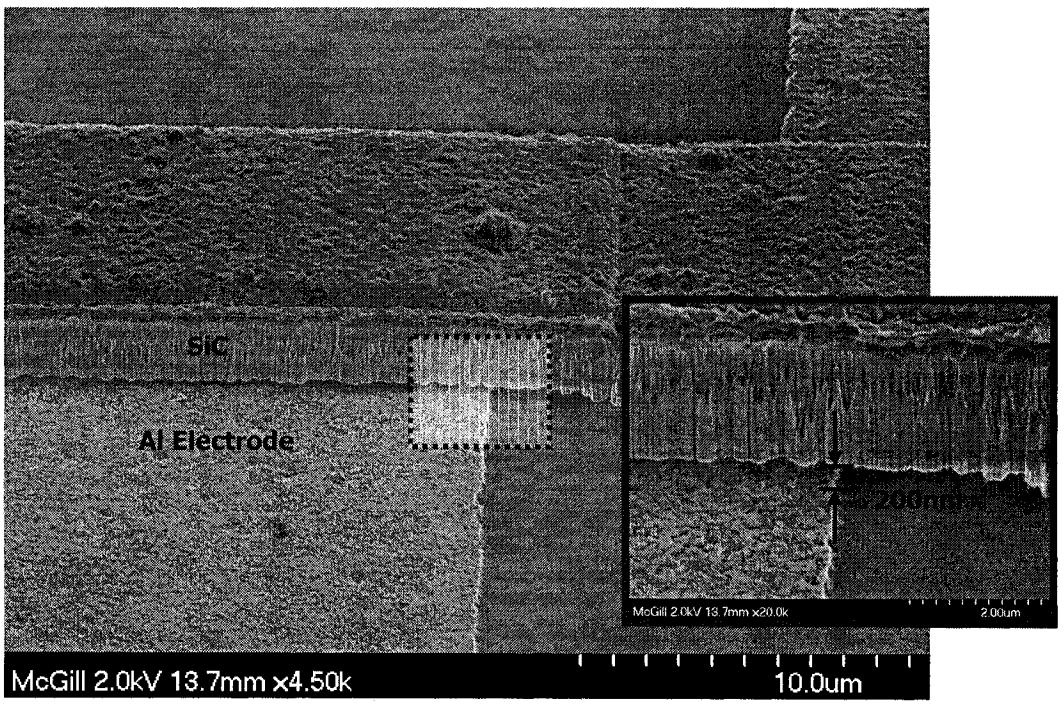

Figure 4-10: Fabricated resonator with modified process and 200nm gap

4.3 MEASUREMENT SETUP

This section provides a description of the test setup that was used to take RF measurements, along with the process of dicing and packaging finished devices.

4.3.1 Dicing and Packaging

Before the removal of the sacrificial layer, the completed wafers were diced into individual 4mm x 4mm dies using an automated dicing saw. Since this is inherently a dirty process, the wafer was first coated with a 2μm layer of photo-resist which acted as a protective coating. Without this step, the residue from the dicing process was found to accumulate on the metal surfaces of the devices and reduce the reliability of the wire-bonding process.

After dicing, the photo-resist coating was removed using acetone and IPA and the individual dies were rinsed in DI water to flush away any remaining residue. The sacrificial layer was then subsequently removed to release the finished MEM resonators.

To facilitate testing of the devices, individual dies were glued into 28-pin LCC ceramic packages using a conductive epoxy, and cured at 100°C for one hour. Each of these small dies contained 33 individual resonators arranged into three rows which were then selectively bonded to the package leads. In the case of the standard resonators which only have two pads, a total of 11 devices were bonded per package as shown in Figure 4-11. The layout of the devices and the bonding arrangement was specifically chosen to minimize the parasitic capacitive coupling between the input and output ports of the resonator. Note that each device is bonded with the input and output to adjacent sides of the package.

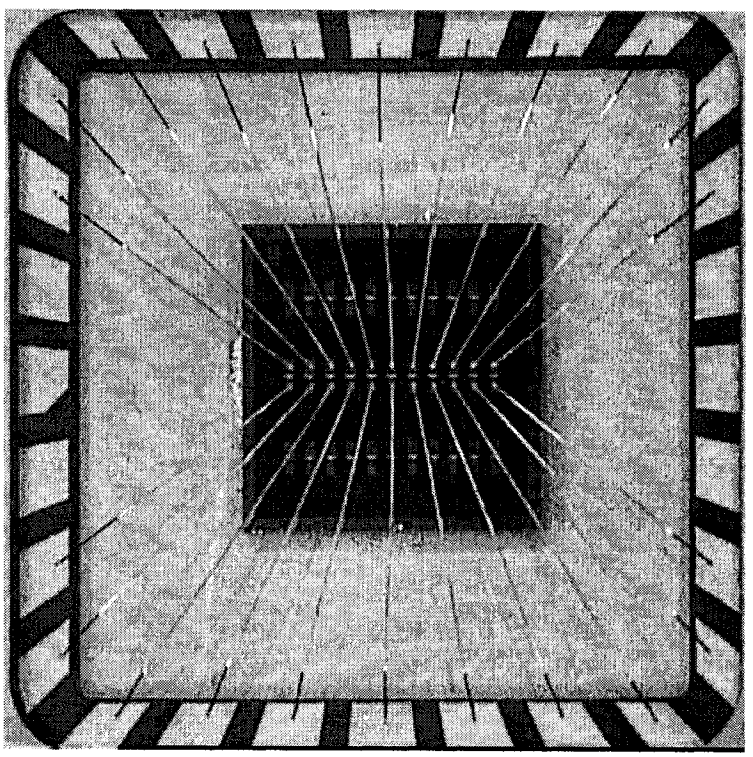

Figure 4-11: Packaged resonator die

A close-up view of a bonded device is shown in Figure 4-12.

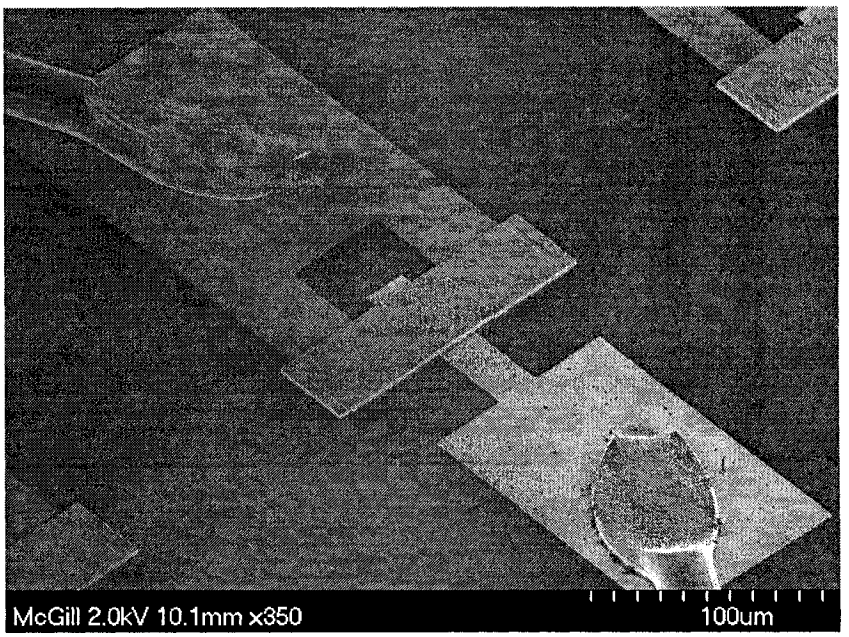

Figure 4-12: SEM photograph of a bonded MEM resonator

If the parasitic feed-through capacitance of the test setup is large, it can mask the small motional current of the resonator and make the true Q-factor difficult to extract. Consider the equivalent small-signal model of the resonator shown in Figure 4-13, with the package feed-through included.

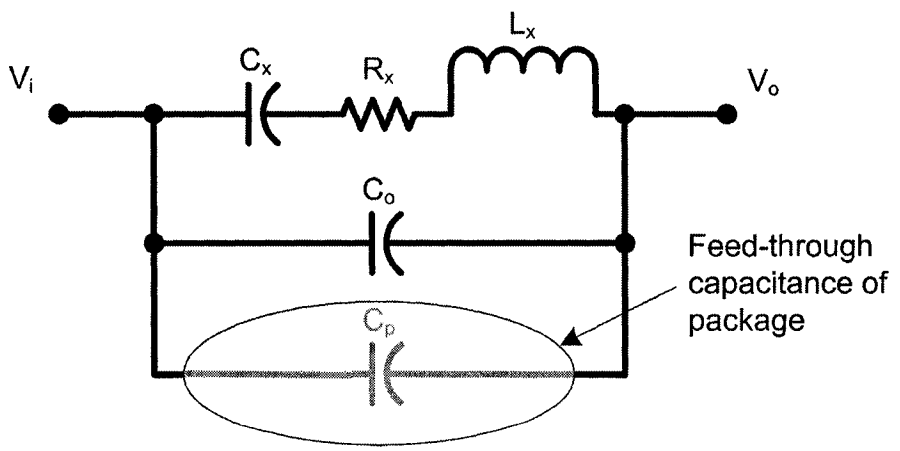

Figure 4-13: Resonator small signal model with package parasitics

The package capacitance (C_p) creates an additional parallel resonance very close to the desired series resonance of the MEM resonator. This manifests itself as an anti-resonant peak

at a frequency that is slightly higher than the natural frequency of the resonator. This parallel resonance will have a frequency of

$$\omega_a = \sqrt{\frac{(C_o + C_p) + C_x}{(C_o + C_p)C_x L_x}} \qquad \text{Eq. (4.2)}$$

and is related to the series resonant peak as

$$\frac{f_p}{f_s} = \sqrt{1 + \frac{C_x}{(C_o + C_p)}} \qquad \text{Eq. (4.3)}$$

Thus, as the parasitic package capacitance C_p increases, the anti-resonant peak will move towards the series resonant peak and can make the real Q-factor difficult (if not impossible) to measure. In order to ensure a measurable peak of 6dB, the ratio of the motional impedance to parasitic impedance should be kept below 0.5 [7], which can be expressed as

$$\frac{R_x}{1/(\omega C_o + \omega C_p)} < 0.5 \qquad \text{Eq. (4.4)}$$

Using this equation, a 10MHz resonator with a motional resistance of 10kΩ should have a total parallel capacitance of <1pF, to ensure that the Q-factor can be accurately measured.

4.3.2 Vacuum System and Test Fixture

In order to obtain the highest Q-factor possible, MEM resonators must be used in vacuum to reduce the effects of air damping. For this work, a custom designed test fixture was fabricated that included a LCC package socket that could be placed in vacuum and connected to external test equipment with 28 separately accessible electrical feed-throughs. Shown in Figure 4-14 is a cross-section of the test fixture which was designed to mate with a KF-type vacuum fitting.

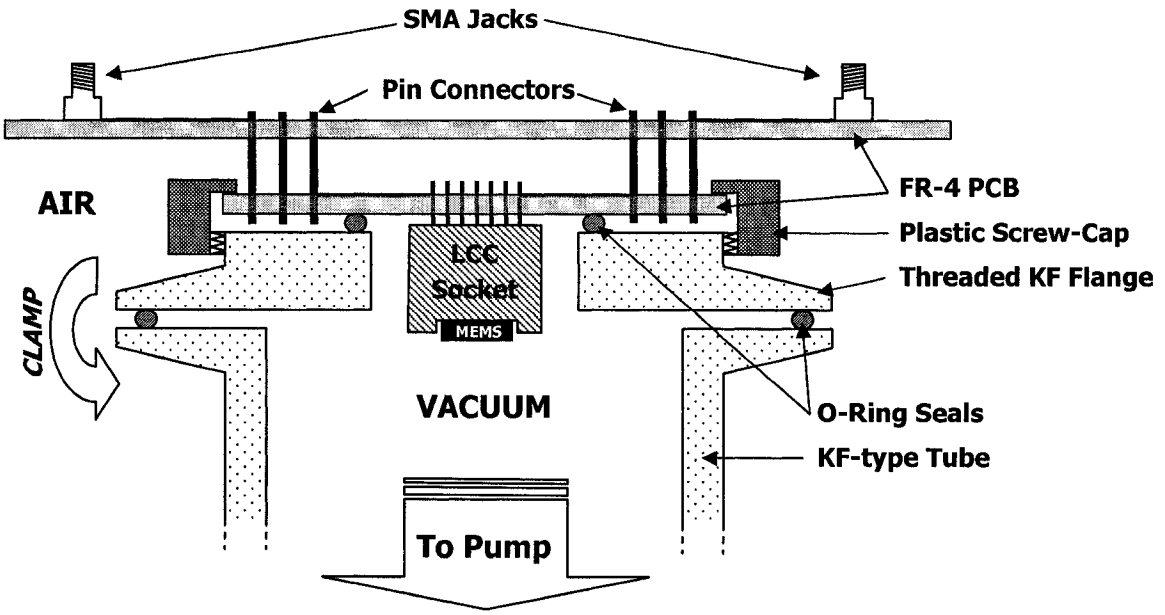

Figure 4-14: Cross-section vacuum test fixture

This fixture is comprised of two separate PCB boards that mate together through a set of 28 jumper-type pin connectors. The top board has 28 separate SMA connectors that are used to measure the RF signal from each of the pins of the LCC package. The bottom board forms the interface between the atmosphere and the vacuum chamber, and holds a through-hole type socket which contains the packaged MEM dies. Each one of the leads of the socket are connected to a separate pin connector and routed to a SMA on the top board. All seals are made with plastic O-rings and hi-vacuum grease capable of withstanding pressures up to 300psi. The connection to the vacuum pump is made via a KF-type quick connect flange which makes for easy assembly. Once the chip is seated in the socket, the entire fixture is directly mated to the input port of a vacuum pump via a KF-type fitting. Using this setup in conjunction with a mini-TASK turbo pump available from Varian Inc., MEM resonators were successfully tested at pressures <2mTorr. Photos of the assembled vacuum system are shown in Figure 4-15.

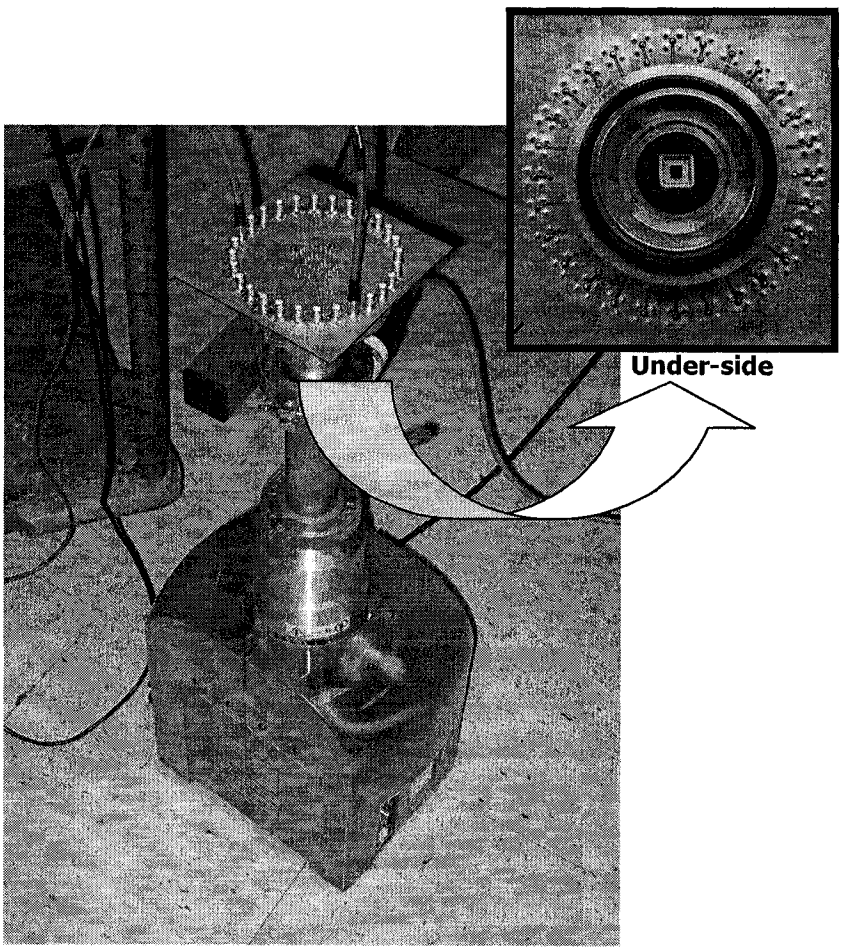

Figure 4-15: Photo of vacuum test system and under-side of vacuum fixture

4.3.3 Measurement Setup

The S-parameters of the packaged MEM devices were measured under vacuum using a HP 8753 vector-network analyzer (VNA) and a SA5211 trans-impedance amplifier. The complete test setup along with the DC biasing is shown in Figure 4-16.

Two DC voltage supplies are used for biasing and tuning. One of the supplies provides the necessary voltage for electromechanical transduction across the resonator gap (V_p), while the second supply (V_{heat}) is used to tune the frequency of devices that include an integrated heater (see section 4.1.3). Both sources are used in conjunction with a series connected resistor to limit the current through the device. The 100kΩ resistor in series with V_p limits the current in

the case of an electrical short between the input and output of the device, whereas the 120Ω resistor helps to limit the current flowing through the heater of the MEM resonator.

The SA5211 trans-impedance amplifier (TIA) provides a gain of ~14.4 kV/A and is included to amplify the motional current from the resonator which can be as small as a few nano-amps. Without this extra TIA, it is difficult to accurately measure both the Q-factor and the resonant frequency, since the resonant peak can be corrupted by noise.

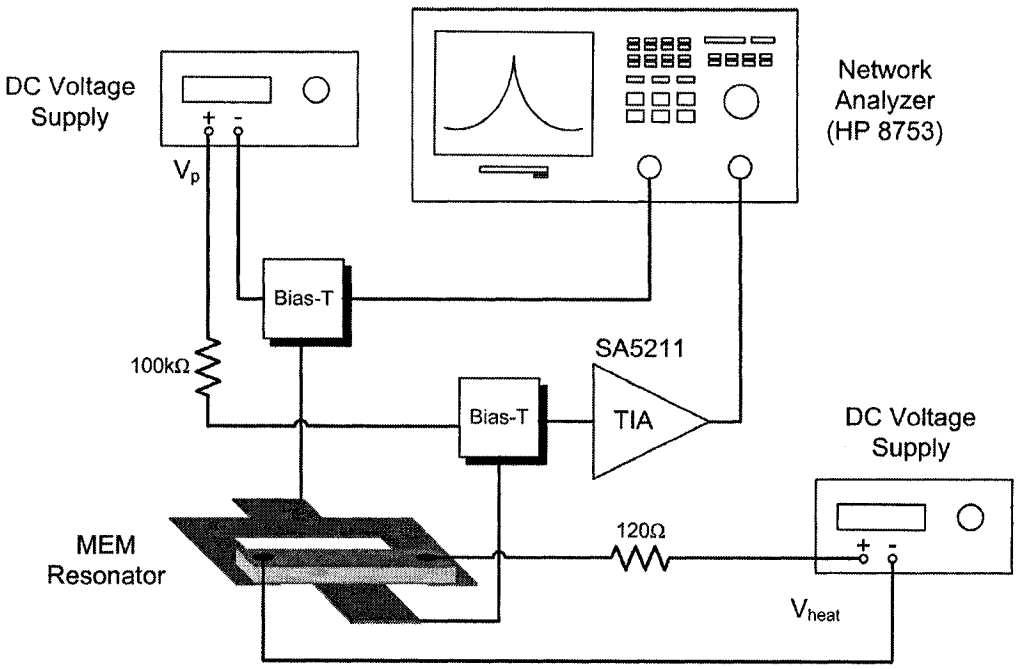

Figure 4-16: Schematic of test setup

4.4 DC TEST RESULTS

DC characterization was performed by placing a large voltage between the input and output ports of the device and recording the value at which breakdown occurs. For MEM beam resonators, the maximum bias voltage can be limited by either electrical or mechanical breakdown. When a large voltage is placed across the input and output of the device the beam deflects toward the bottom electrode. If the voltage is large enough, the beam will

collapse onto the substrate and create a short circuit, destroying the device. Using an energy balance analysis, the mechanical breakdown voltage can be shown to be equal to [8]

$$V_{pd} = \sqrt{\frac{8}{27}\frac{K_r g^3}{\varepsilon_o W_r W_e}} \qquad \text{Eq. (4.5)}$$

where g is the gap thickness, W_r is the resonator width, W_e is the electrode width. K_r is the effective stiffness for a fixed-fixed beam and can be calculated from the device geometry as

$$K_r = 32EW_r\left(\frac{h}{L_r}\right)^3 \frac{1}{2-\left[2-\left(\frac{W_e}{L_r}\right)\right]\left(\frac{W_e}{L_r}\right)^2} \qquad \text{Eq. (4.6)}$$

where L_r is the length of the resonator.

The maximum bias voltage can also be limited by electrical breakdown across the resonator gap. The voltage at breakdown in this case is strongly related to the geometry of the device (corners) and surface roughness [8].

Measurements of the breakdown voltage were made for resonators with 200nm and 300nm gaps. As previously mentioned, all devices with a 100nm gap consistently broke down at approximately 5V regardless of the beam length, suggesting that electrostatic breakdown and not mechanical breakdown is the cause. Since the gap is very thin in this case, an electrical short can easily form between the input and output if the polyimide does not uniformly cover the bottom electrode. The small measured voltage is instead most likely a result of the breakdown of the native oxide on the aluminum electrodes. Measurements with a multi-meter show that, after breakdown, these resonators become a short circuit of only a few Ohms.

In contrast to this case, almost 100% of the devices with 200nm and 300nm gaps were fully functional, suggesting that the problem is indeed caused by thin areas in the polyimide film. Figure 4-17 plots a comparison between the measured and theoretical breakdown voltages for resonators with 0.3μm gaps for three different lengths (64μm, 45μm and 37μm).

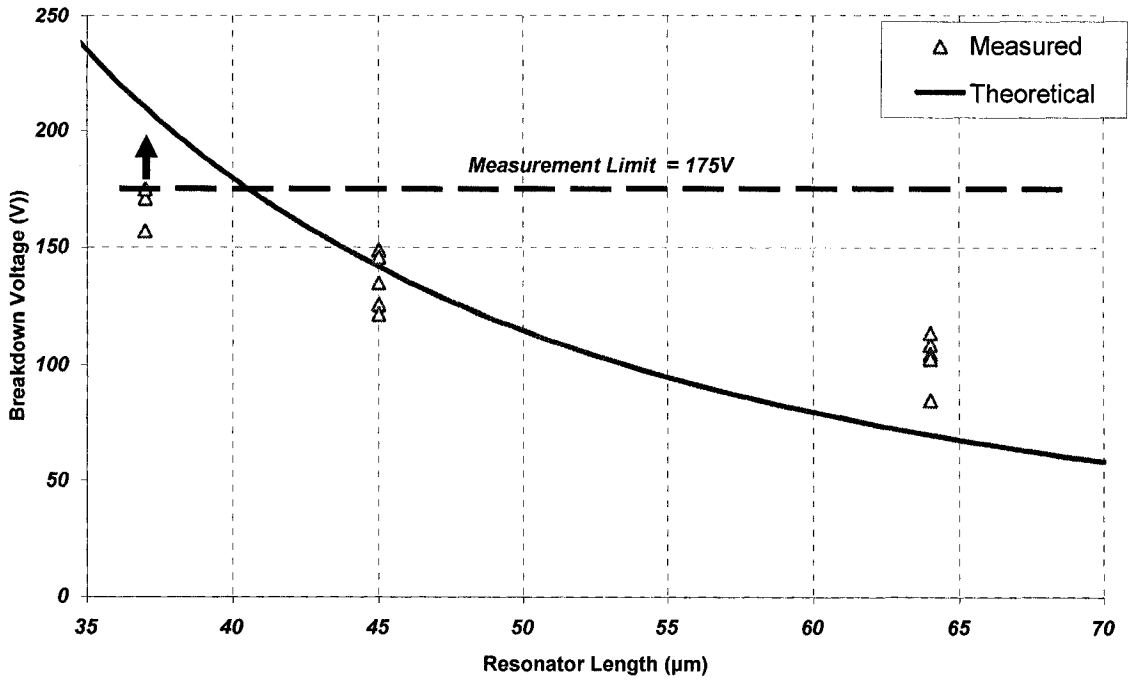

Figure 4-17: Measured vs. theoretical breakdown voltages for resonators of different lengths (300nm gap)

As expected, the shorter the beam length (higher resonator frequency), the larger the measured breakdown voltage since the effective mechanical stiffness is greater. Breakdown could not be accurately measured for beams 37μm and shorter, since it exceeded the maximum available voltage of the test setup (175V). In these cases, a lower limit of the breakdown voltage can be assumed to be about 175V as indicated by the upward arrow in Figure 4-17.

For resonators with a 200nm gap, the measured breakdown voltages were much lower, as expected. Figure 4-18 plots a comparison between the measured and theoretical breakdown voltages for resonators with 0.2μm gaps for three different lengths (64μm, 45μm and 32μm).

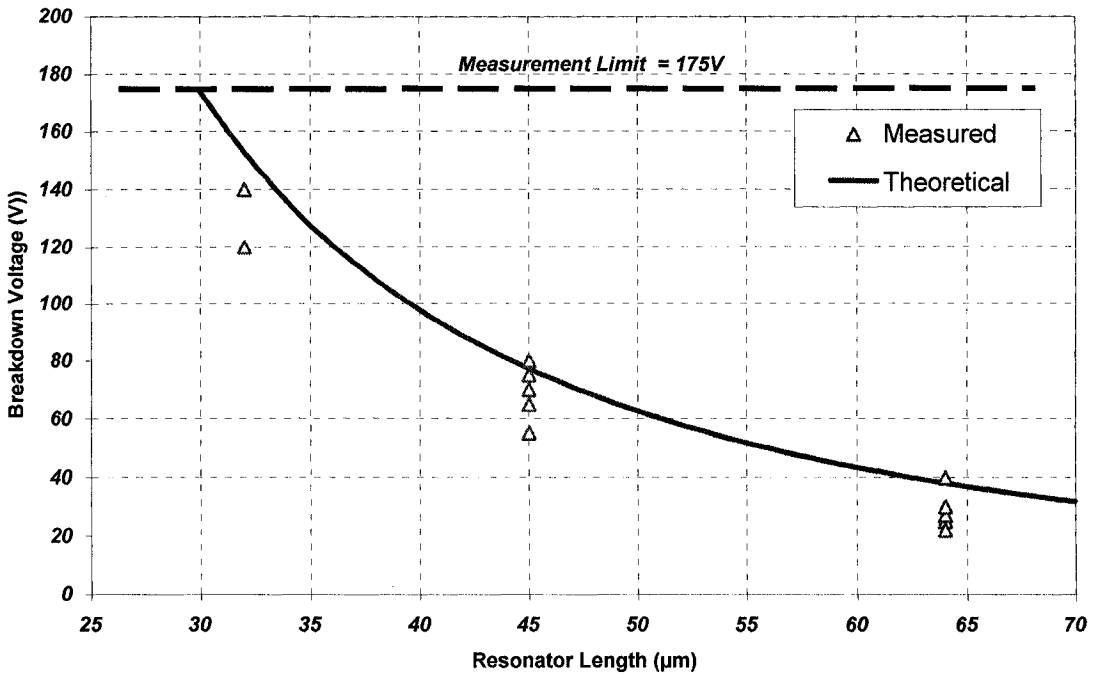

Figure 4-18: Measured vs. theoretical breakdown voltages for resonators of different lengths (300nm gap)

The measured breakdown correlates well with the theoretically predicted trend; however, the spread in the measurements is quite large. Pre-mature breakdown is most likely due to electrical breakdown and not due to the collapse of the beam onto the bottom electrode. Any particles or residue in the gap, or non-uniform coverage of the thin polyimide structural layer will cause the beam to collapse at lower voltages.

4.5 AC MEASUREMENTS

The following section presents the measured AC characteristics of several different resonator designs with both 200nm and 300nm gaps. Characterization was performed using the custom-built vacuum system described in sections 4.3.2 and 4.3.3, at a base pressure of approximately 10mTorr. The effects of resonator geometry on the resonant frequency and Q-factor are investigated, along with the tuning range obtained by varying both the bias voltage

and the temperature of the device. Lastly, the effect of the input power on the resonator's characteristics is also presented.

4.5.1 Q-factor

The measured Q-factor ranged from approximately 250 to 500. Of all of the measured devices, the 40μm wide resonators were consistently observed to perform the best. Figure 4-19 shows the measured S21 of a 40μm wide, 5MHz resonator with rectangular electrodes. All of the following measurements were performed using a source power of -20dBm.

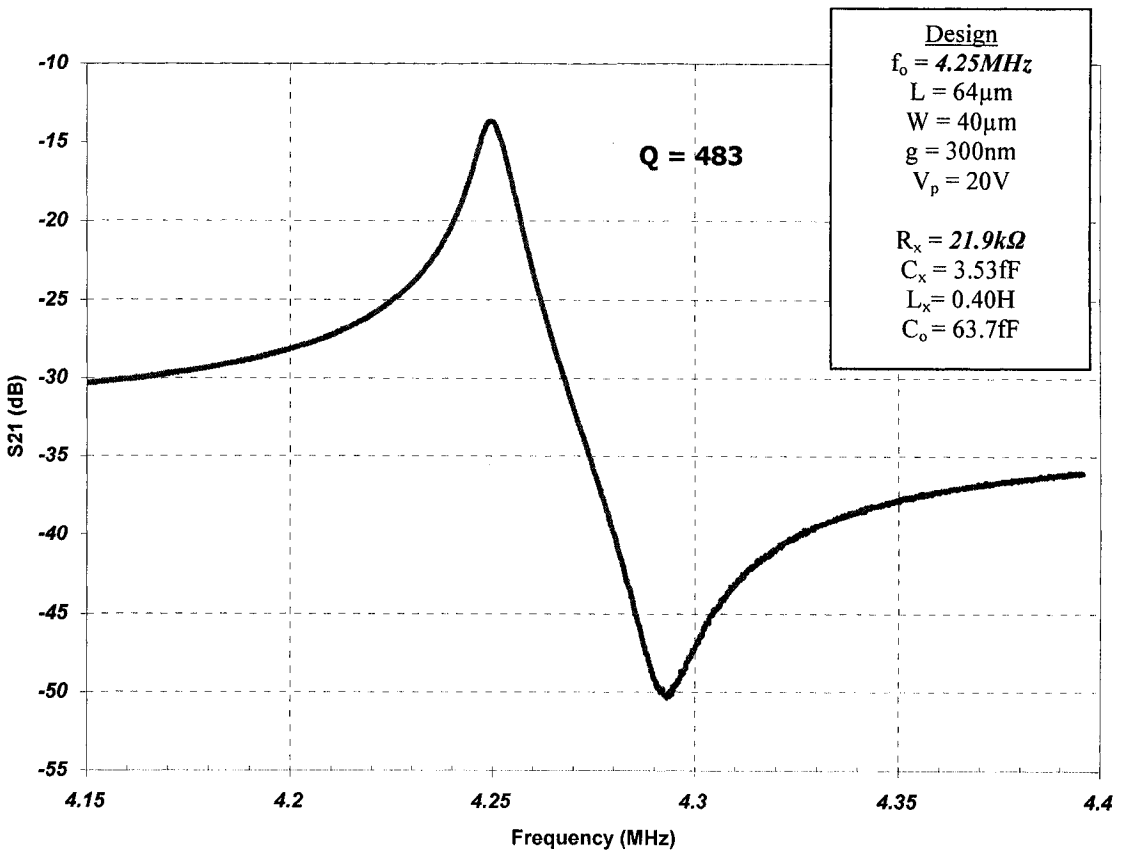

Figure 4-19: Measured S21 of a 5MHz, 40um wide resonator with rectangular electrodes (300nm gap)

This device had a measured frequency of 4.25MHz at a bias voltage of 20V, and a Q-factor of 483. Using the formulas presented in Chapter 2, the motional resistance for this device is calculated to be about 21.9kΩ. One of the advantageous of such a wide beam is that the electrode area is very large, and therefore the motional resistance is still small even with a

relatively low Q-factor. In this plot, the anti-resonant peak is clearly visible, and occurs at a frequency of 4.29MHz. Using Eq. (4.3), the parasitic capacitance due to the package and test fixture can be estimated to be about 140fF.

The size of the resonator gap was not observed to have a significant effect on the resonator Q-factor. Figure 4-20 plots the measured S21 of a similar 10MHz resonator design, except with a 200nm gap.

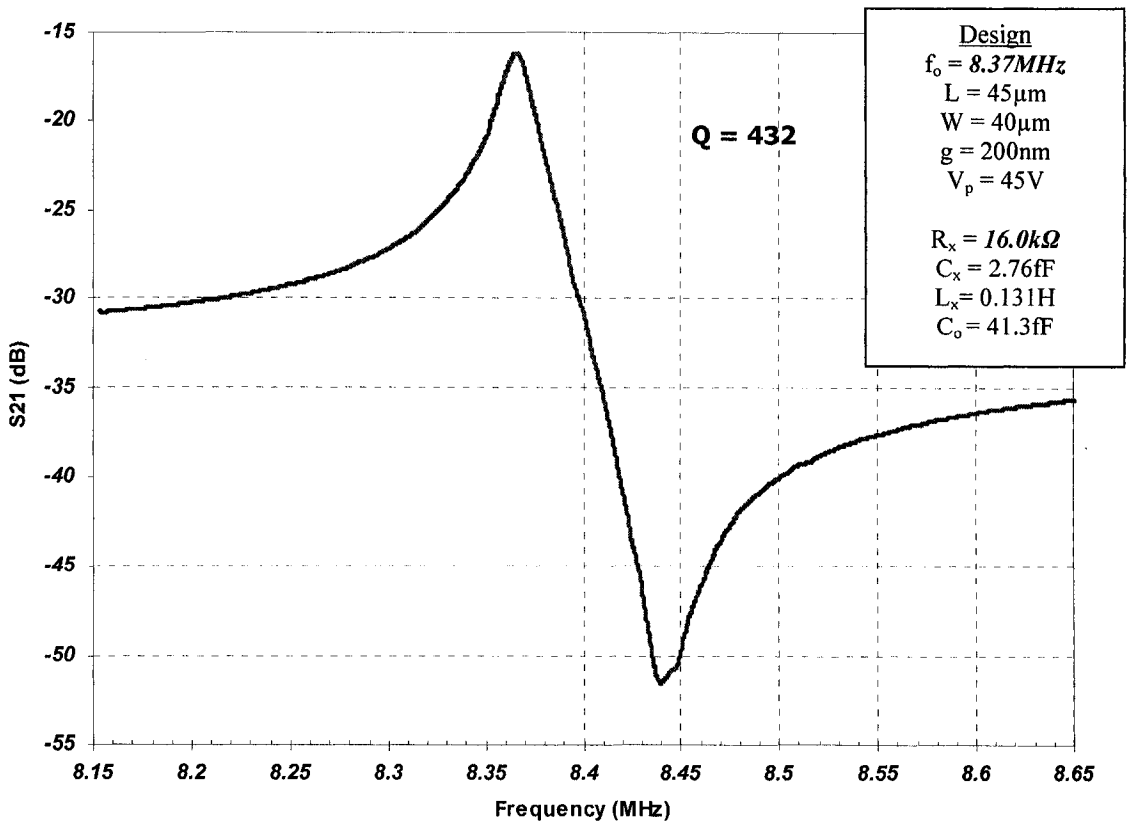

Figure 4-20: Measured S21 of a 10MHz, 40um wide resonator with rectangular electrodes (200nm gap)

Note that, in this case, the performance is similar except that the motional resistance is about four times smaller.

Resonators with smaller beam widths tended to have a lower Q-factor. For the 10μm wide devices, the average measured Q was in the order of about 250. The S21 of a 10μm wide, 5MHz resonator is shown in Figure 4-21.

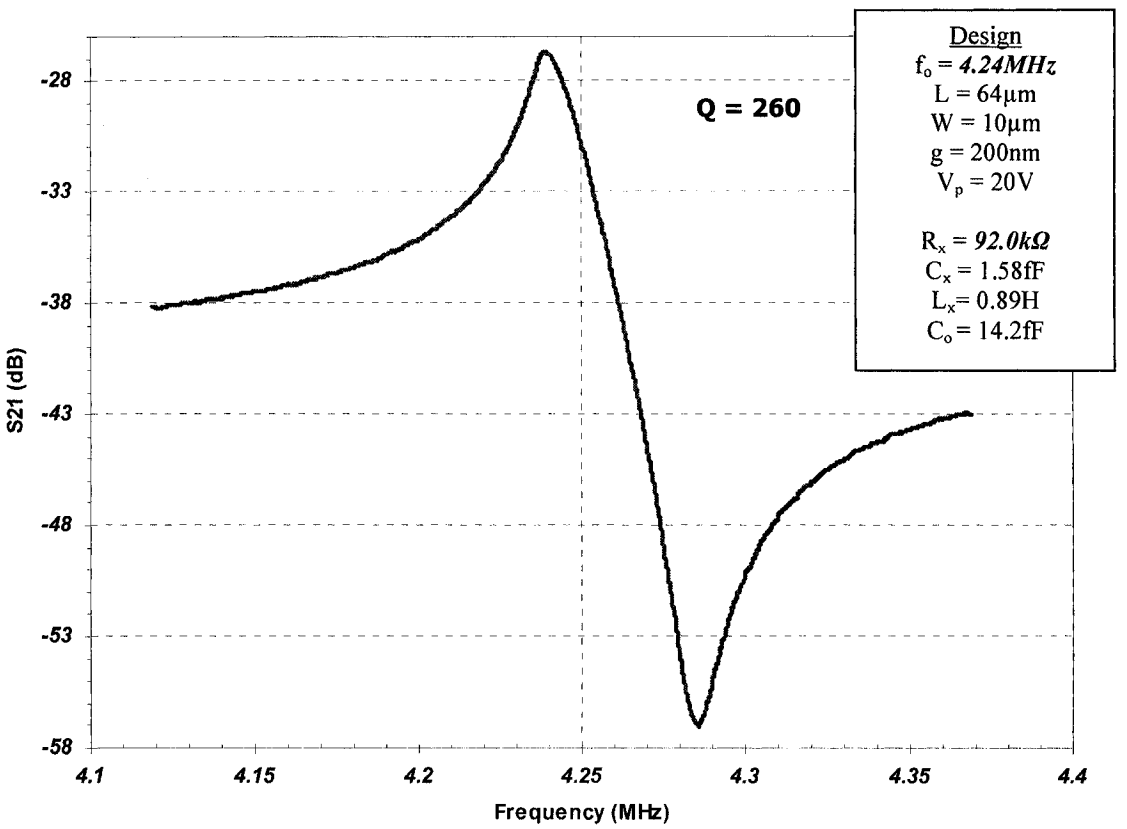

Figure 4-21: Measured S21 a 5MHz, 10um wide resonator with standard electrodes (200nm gap)

In this case, the frequency is approximately the same as the 40μm wide beam shown in Figure 4-20 as expected; however, the motional resistance is much higher due to the smaller electrode area. One other major difference is the shape of the transfer function. In this case, the resonant peak is leaning towards the left, which is characteristic of Duffing distortion. As explained in detail in section 2.5, the third-order non-linearity in the electrical spring constant tends to distort the shape of the resonant peak. Since the gap is 30% smaller for this device, the third-order non-linearity is also much larger, and thus, Duffing distortion happens at a

lower input power. As a result, a resonator with a smaller gap will have a low motional resistance, however, at the cost of lower power handling and linearity.

Similar results were also obtained for devices with *shaped* electrodes. Shown in Figure 4-22 is the measured S21 of a 10μm wide, 10MHz resonator with electrode shaping.

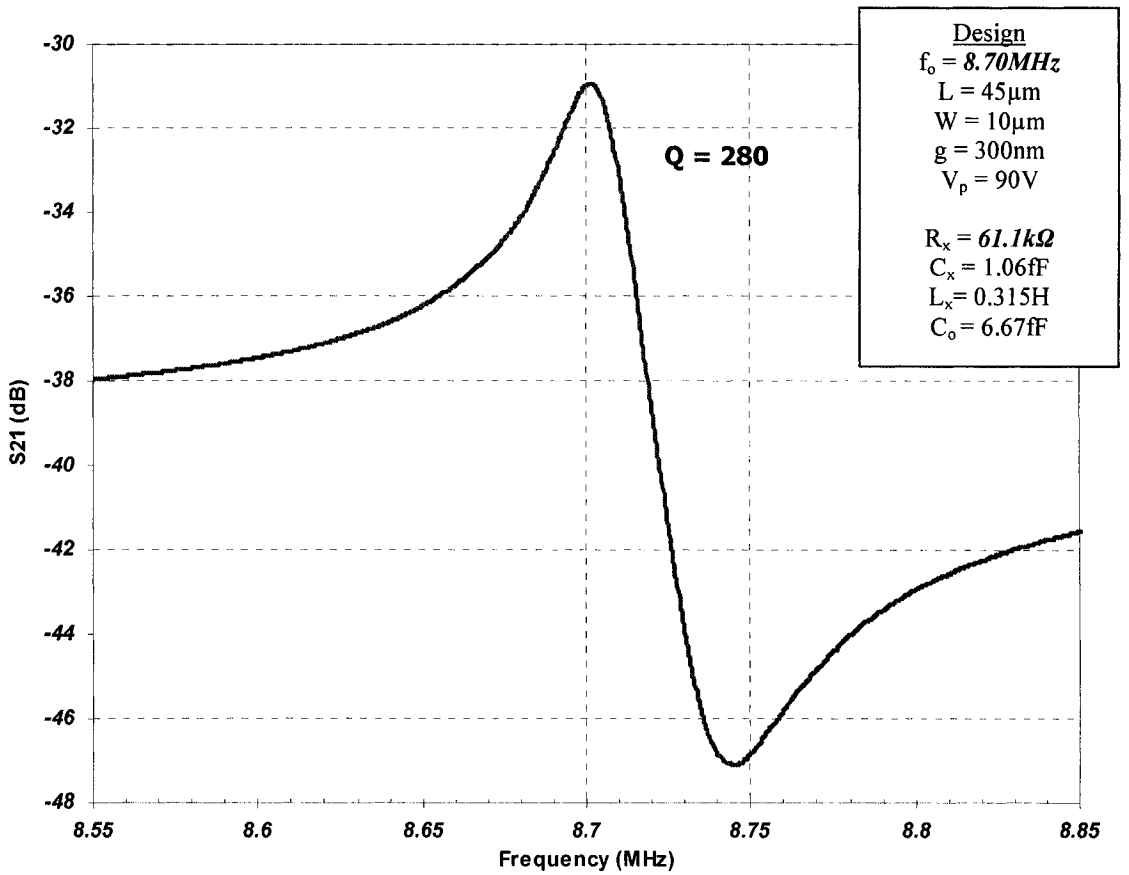

Figure 4-22: Measured S21 of a 10MHz, 10um wide resonator with shaped electrodes (300nm gap)

These devices were originally designed to suppress higher-order modes; however, since the signal level of the resonators was so low, no other output modes could be observed for any of the devices. Thus, it was impossible to determine whether or not the shaped electrodes helped to reduce feed-through at higher frequencies.

The measured Q-factor of these devices was also found to vary with the applied DC bias voltage. Figure 4-23 plots the measured Q-factor vs. the bias voltage for the 10MHz

resonator shown in Figure 4-22. For voltages smaller than 50V, the resonant peak was less than 3dB and thus, the Q-factor could not be measured.

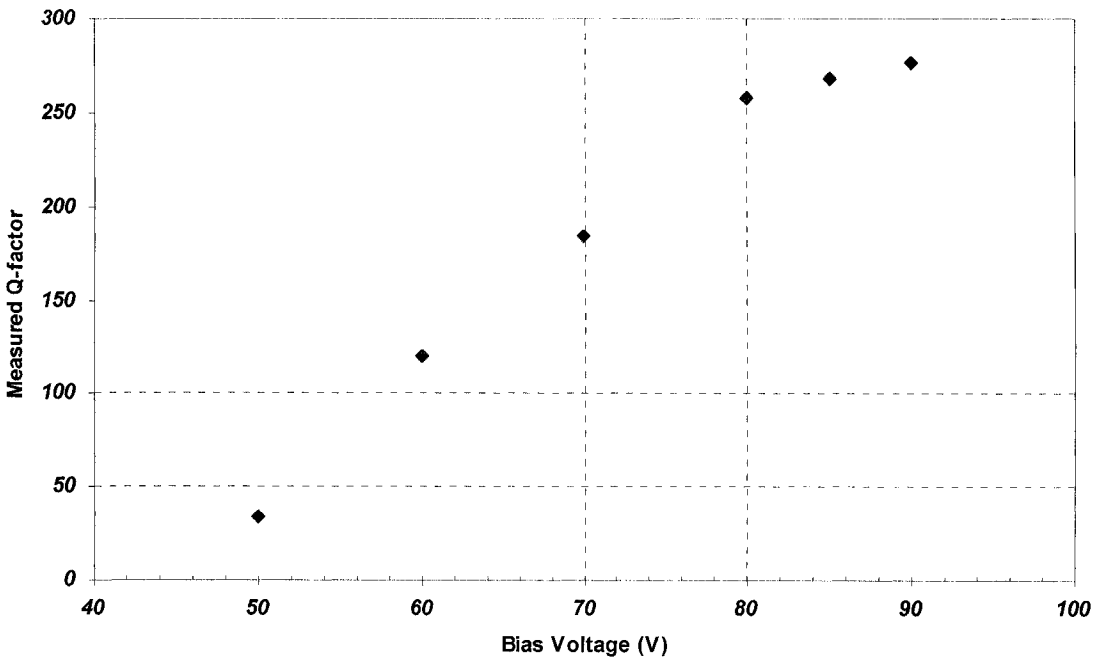

Figure 4-23: Measured Q-factor vs. bias voltage

The increase in the measured Q-factor with voltage is due to the effect of the parallel feed-through capacitance of the resonator shown in Figure 4-13. At a low bias voltage, the motional resistance (R_x) of the resonator is very large and thus the frequency response is dominated by this parasitic feed-through capacitance. The combined result is that the resonant peak is spread out, and the measured Q-factor will be much lower than the actual value. Since the resistance of the resonator decreases with the square of the bias voltage, at higher values of the bias voltages the motional current from the resonator will be much larger. In this case, the response is dominated by the resonator and the measured Q-factor will be close to the actual value of the mechanical resonance.

Figure 4-24 shows the simulated Q-factor vs. bias voltage using the small-signal model parameters given in Figure 4-22, for several different values of C_p.

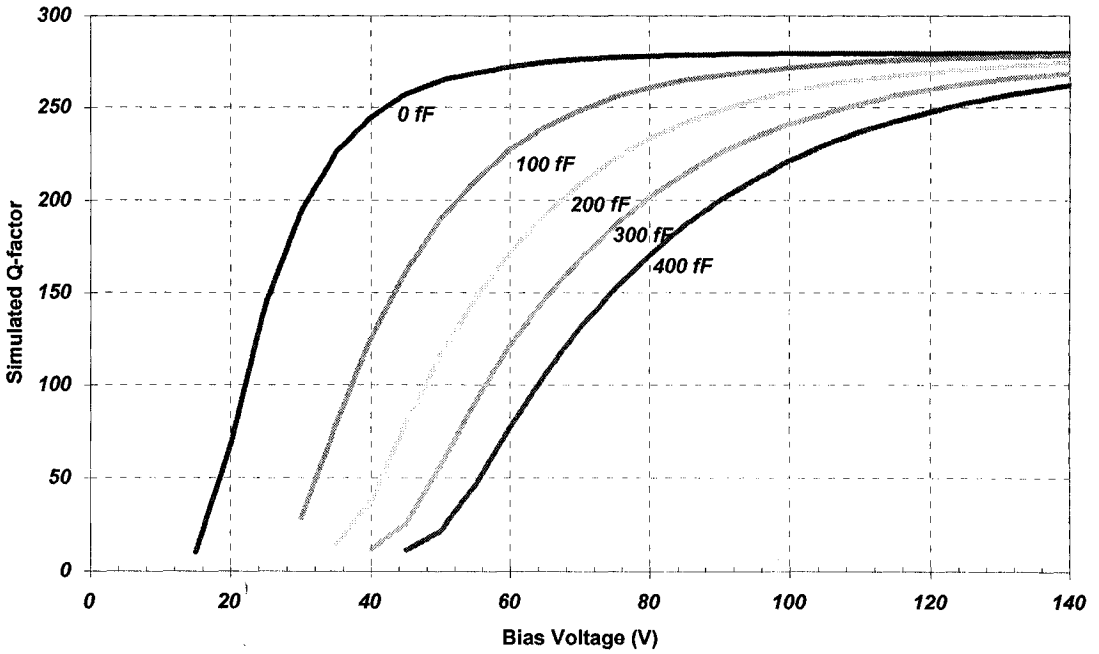

Figure 4-24: Simulated Q vs. voltage for different values of C_p

This plot clearly illustrates the effect of the parasitic feed-through capacitance (C_p) on the measured Q-factor. If the package capacitance between the input and output port is too large, the measured Q-factor will be much lower than the actual value. In all cases, however, the measured Q-factor will asymptotically approach the actual value at high enough voltages.

In general, the measured Q-factor for all fabricated devices was much lower than expected. From other published results [9], the Q-factor should be in the range of 1000-3000 for clamped-clamped beams of this type; however, the maximum measured value for these devices was approximately 500.

Several energy loss mechanisms may be limiting the Q-factor of the devices fabricated in this work. First, any residue left in the resonator gap will greatly increase the damping and reduce the Q-factor. Even a few small particles in the resonator gap are enough to seriously dampen the resonant peak. For these prototype devices, the polyimide was not filtered prior to spin-coating, which may have had an adverse effect on the device performance. Second, as

explained in chapter 2, the frequency of these devices is in the same range as the thermo-elastic damping peak of SiC and Al. Thus, the Q-factor may be limited by the intrinsic damping of the material. Other material effects such as grain-boundary sliding and localized defects may also be contributing to energy loss.

4.5.2 Resonant Frequency

In general, the resonant frequency of the measured devices correlated well with the beam length and expected frequency from analytical analyses. Figure 4-25 plots the measured frequency at low bias voltages for several different resonators, along with the theoretical design values.

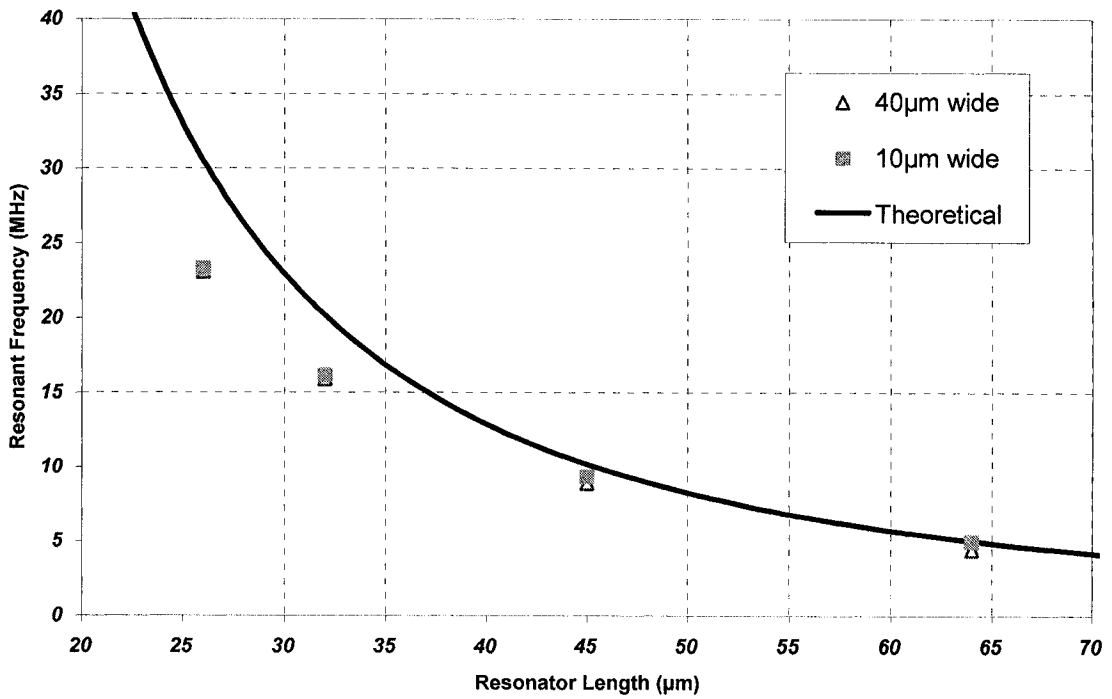

Figure 4-25: Measured frequency vs. theoretical (Eq. 2.18) value for resonators of different widths

Although the resonant frequency increases with decreasing beam length, it does not closely follow the theoretically predicted values for shorter beams. For longer beams the measured resonant frequency is larger that the design value, while for shorter beams, it is lower than the design value. Moreover, wider beams are observed to have slightly lower frequencies for

a given length. These variations are most likely due to several factors such as differences between the design and on-wafer dimensions, variation in the structural layer thickness, non-ideal topography of the beam (anchor step-up) and finite elasticity effects [10]. As the beam gets shorter, small changes in the beam length or topography will have a greater impact on the resonant frequency.

The "spring-softening" effect of the bias voltage (V_p) was also observed for all devices. Increasing the bias voltage increases the effective electrical spring constant of the device which subtracts from the mechanical spring constant to lower the resonant frequency. Shown in Figure 4-26 is the measured S21 of a 5MHz resonator at 2.5V increments of the bias voltage starting from 5V (right most curve), to 40V (left most curve).

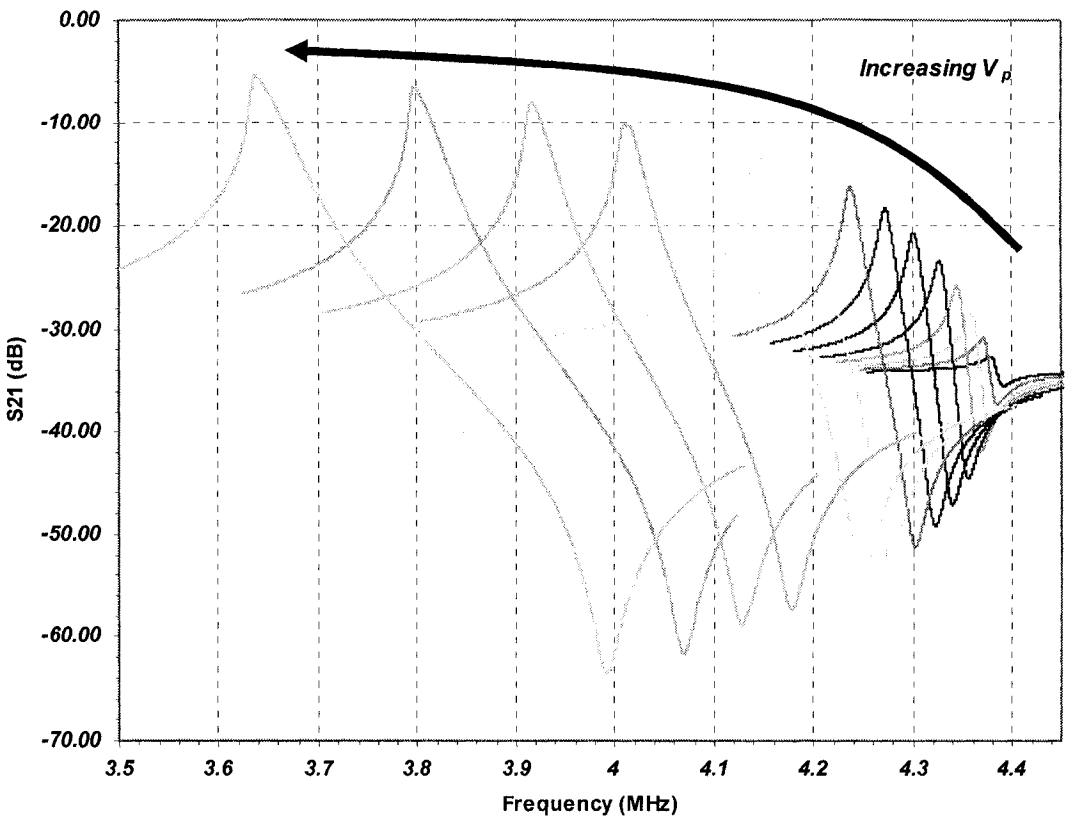

Figure 4-26: Measured resonant frequency vs. bias voltage for a 5MHz resonator

Note that, as the bias voltage is increased, the resonant peak shifts downward in frequency as well as growing in size. For this particular device, the frequency tunes from a zero bias value of 4.37MHz down to 3.64MHz, which is a change of about -18%. The space between the resonant and anti-resonant peak is also observed to increase, since the value of equivalent motional capacitance (C_x) is proportional to the square of the bias voltage. Since C_o and C_p in Eq. (4.3) do not change significantly with frequency, the separation in frequency will become larger.

Higher frequency resonators were observed to have a lower tuning range due to the larger effective spring constant. As shown in Eq. 2.86, the change in the resonant frequency is inversely proportional to k_m, and therefore stiffer beams will experience a smaller change in frequency over the same voltage range.

Figure 4-27 plots the measured percentage change in the nominal resonant frequency as a function of voltage for a 5MHz, 10MHz, 20MHz, and 30MHz resonator.

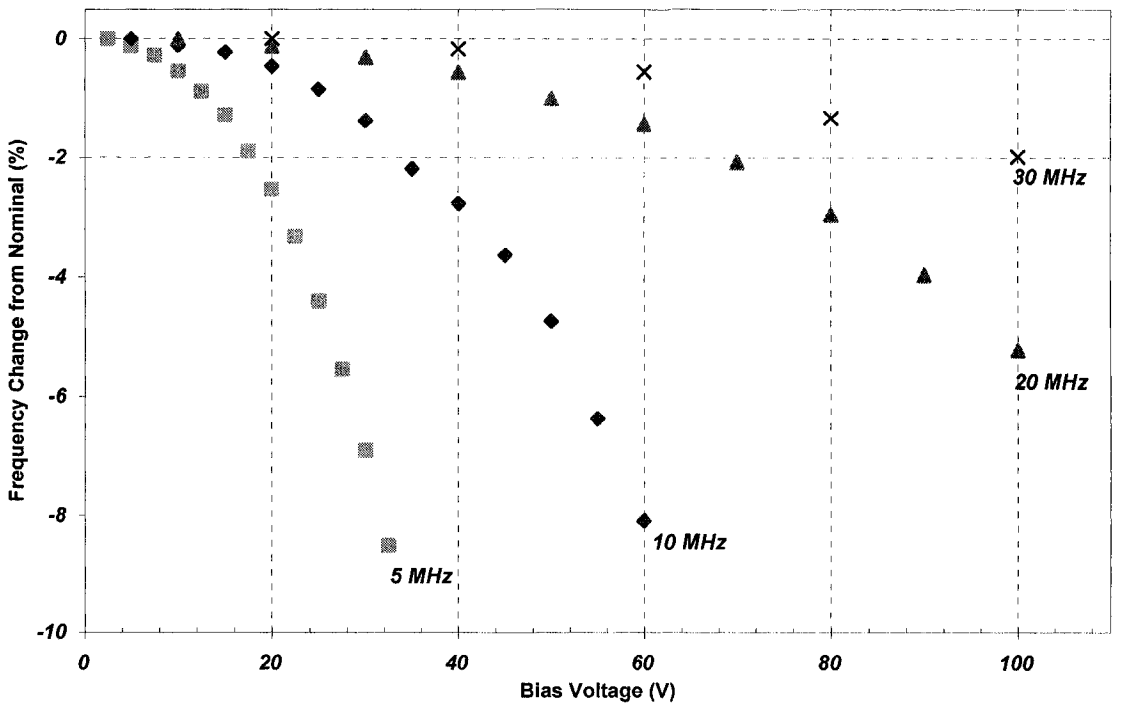

Figure 4-27: Measured frequency change vs. bias voltage for several different resonators

Table 4-1 summarizes the maximum measured tuning range for each of these devices, along with the theoretical maximum predicted by Eq. 2.86.

Table 4-1: Maximum measured and theoretical tuning range of several different resonators

Design Resonant Frequency (MHz)	Measured Max. Frequency Shift (MHz)	Theoretical Frequency Shift (MHz)
5	- 17.6 % @ 40V	-14.7 % @ 40V
10	- 16.7% @ 75V	- 13.1% @ 75V
15	- 5.2% @ 100V	- 6.7% @ 100V
20	- 2.0% @ 100V	- 3.1% @ 100V

The tuning ranges of all of these measured devices agree well with the theoretical values. In general, all of the 5MHz and 10MHz devices that were measured consistently had a much greater tuning range than what is predicted using Eq. 2.86. This observed difference is most likely a result of the static deflection of the beam which is not taken into account when calculating the theoretical values. As shown in Eq. 2.86, the tuning range is related to the inverse cube of the gap height. When the bias voltage is applied, the beam will tend to deflect toward the bottom electrode, which will make the resonant frequency more sensitive to changes in the bias voltage. This effect would be more prominent in the longer beams due to the lower effective spring constant, resulting in a larger tuning range.

4.5.3 Frequency Tuning Using Integrated Heaters

By adding an extra DC bias voltage to the top of the resonator as shown in Figure 4-16, further tuning of the resonant frequency was possible. Figure 4-28 plots the measured change in the S21 of a 40μm wide, 10MHz resonator, first using only tuning through the bias voltage, and then by only adjusting the heater current. For this design the heater resistance was measured to be approximately 1.4Ω.

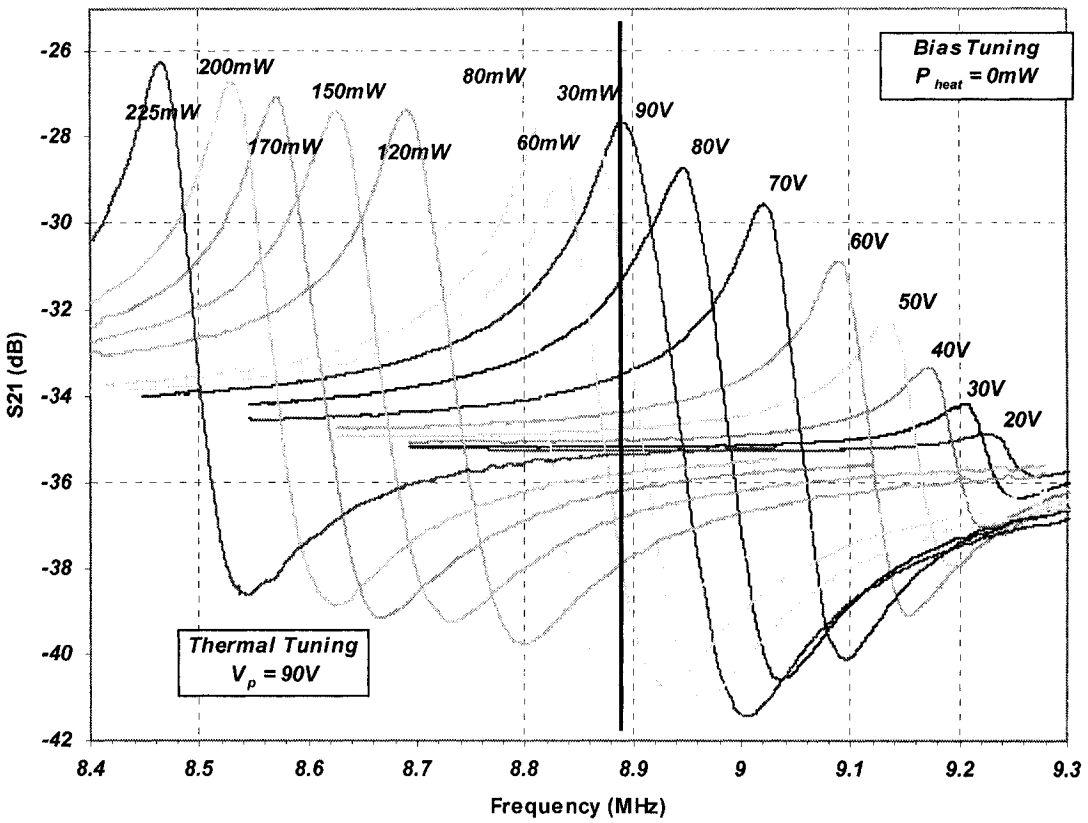

Figure 4-28: Frequency tuning of a 10MHz resonator using the bias voltage and thermal adjustment

For this plot, the bias voltage was first adjusted from 0V to 90V with no heater voltage applied. Once at 90V, further tuning was accomplished by increasing the heater power. Using only the bias voltage, the resonant frequency was observed to change from its nominal value of 9.25MHz down to 8.89MHz, which is a change of about 3.9%. When the heater is turned on, the center frequency can be adjusted down to 8.47MHz, which increases the total tuning range to 8.4%. The change in resonant frequency with heater power is shown in Figure 4-29.

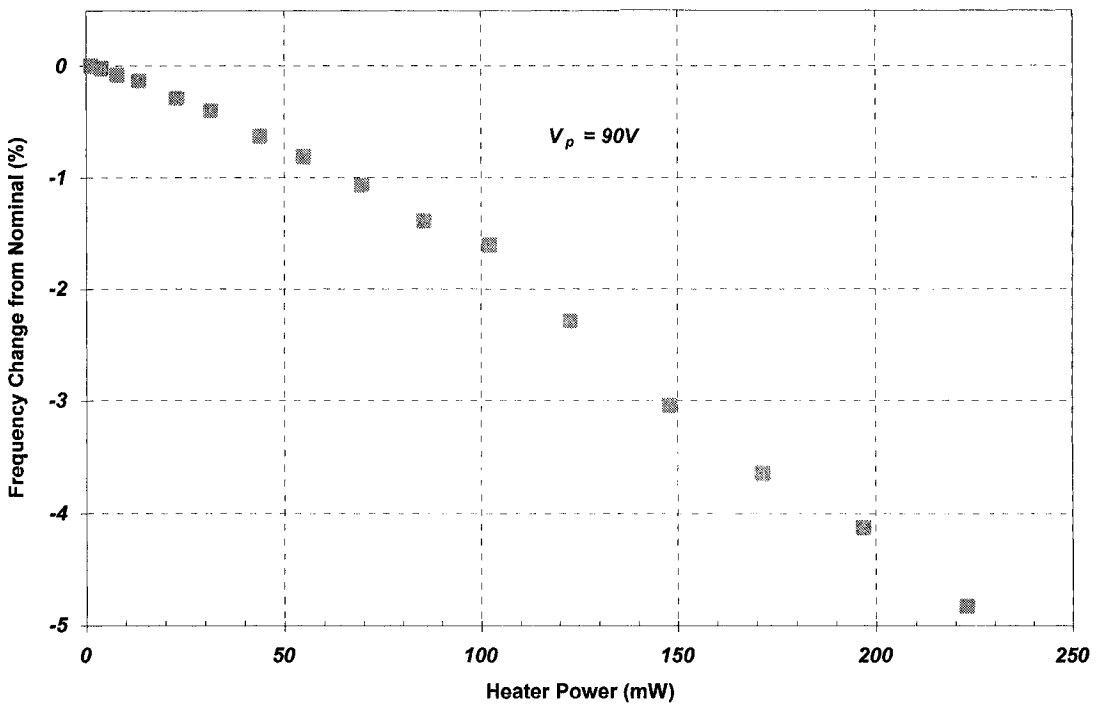

Figure 4-29: Percentage change in resonant frequency vs. heater power

A significant advantage of using thermal tuning is that it does not significantly alter the Q-factor of the device, and thus results in a larger usable frequency range than can be obtained when using bias voltage tuning alone. Changing the bias voltage also changes the frequency; however, since the Q-factor of the device is small at low voltages, the actual usable frequency range is limited. When using thermal tuning, the device can be used over the entire frequency range.

One drawback of this tuning method is the relatively slow response time of the system to changes in the tuning voltage. Since the temperature of the resonator will require a finite amount of time to reach steady state, the speed at which the frequency can be changed will most likely be limited. As a result, this type of tuning may be best suited to applications requiring high frequency stability over a large temperature range. In this case, the heater can be used in a feedback system to directly regulate the temperature of the resonator and keep the frequency constant. The other major drawback is the large amount of power required to

run the heater. In this case, the maximum frequency deviation was obtained with a heater power of about 225mW.

For these devices, the maximum current was limited by the bond-wires of the package which were observed to fail at a current of about 400mA. In future implementations, a more robust bonding scheme using flip-chip technology may be required if a larger tuning range is desired.

4.5.4 Q-factor vs. input power

The Q-factor of the MEM resonators was observed to be a strong function of the input test power. As discussed in Section 2.5, the third-order non-linearities in the spring constant leads to an effect called "Duffing" distortion. This non-linearity causes the frequency response of the device to become a function of the input power at large drive levels. Under these conditions, the resonant peak will tend to "bend" toward lower frequencies due to the non-linear spring softening effect, which results in both a change in the frequency and the measured Q-factor. Shown in Figure 4-31 is the measured S21 of a 10MHz resonator tested at several different power levels. As the input power is increased, the measured resonant peak shifts to lower frequencies and begins to narrow, significantly increasing the measured Q-factor. At the lowest power of -20dBm, the resonant peak is relatively broad with a measured Q of about 200. As the power is increased up to -5dBm, the peak becomes asymmetric and begins to shift toward the left, which is a result of the third-order spring softening non-linearity. As a result of this effect, the measured Q-factor increases to about 260. Above 0dBm, however, the peak remains asymmetric, but begins to 'lean' toward higher frequencies. As shown in Eq. 2.90, the third order spring constant is the difference between the material hardening co-efficient and the electrical softening caused by the DC bias voltage. This shift toward the right suggests that at this power level, material hardening and not spring softening is dominant. The vertical line in the frequency spectrum of these high power levels is a result of the quick transition down from the resonant peak, as the VNA sweeps the test frequency from a lower to a higher value (refer to Figure 2.19).

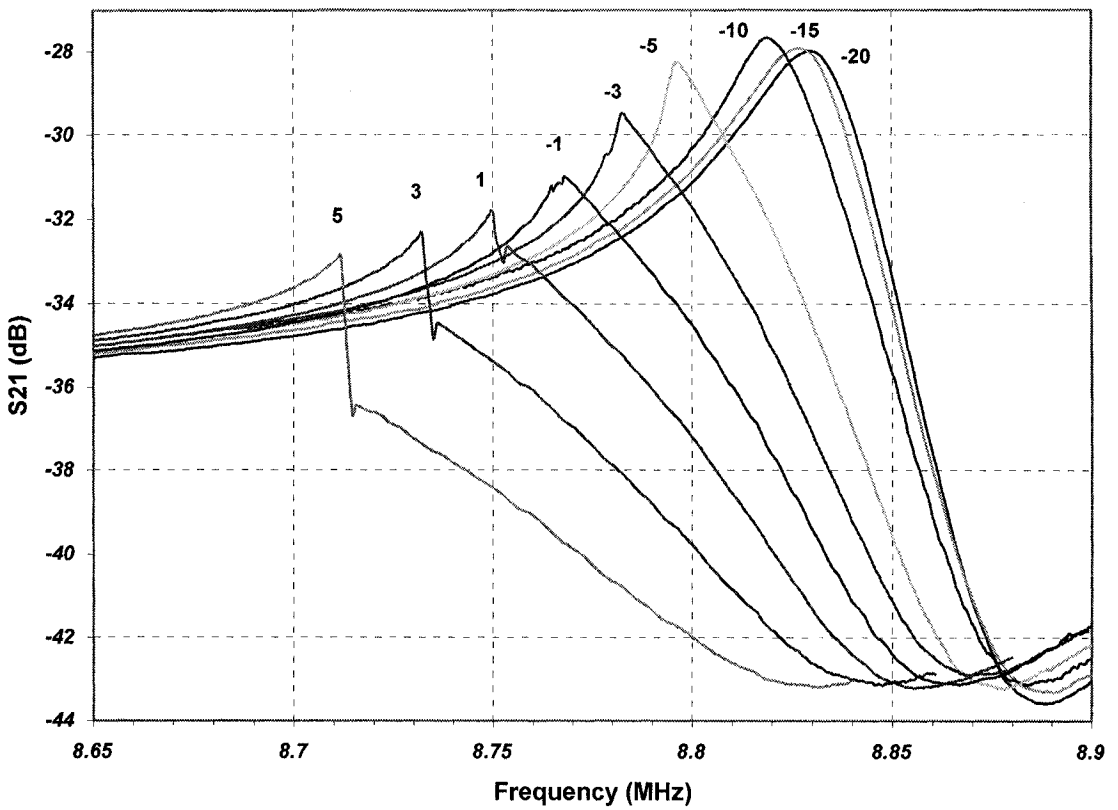

Figure 4-30: Measured S21 of a 10MHz resonator vs. input power

Another consequence of this non-linear behavior is that the measured Q-factor reaches a maximum at a certain power level, and then decreases when entering the material hardening regime. Shown in Figure 4-31 is the measured Q-factor of this device versus input power. Note that the maximum measured Q of about 260 occurs at an input power of -5dBm.

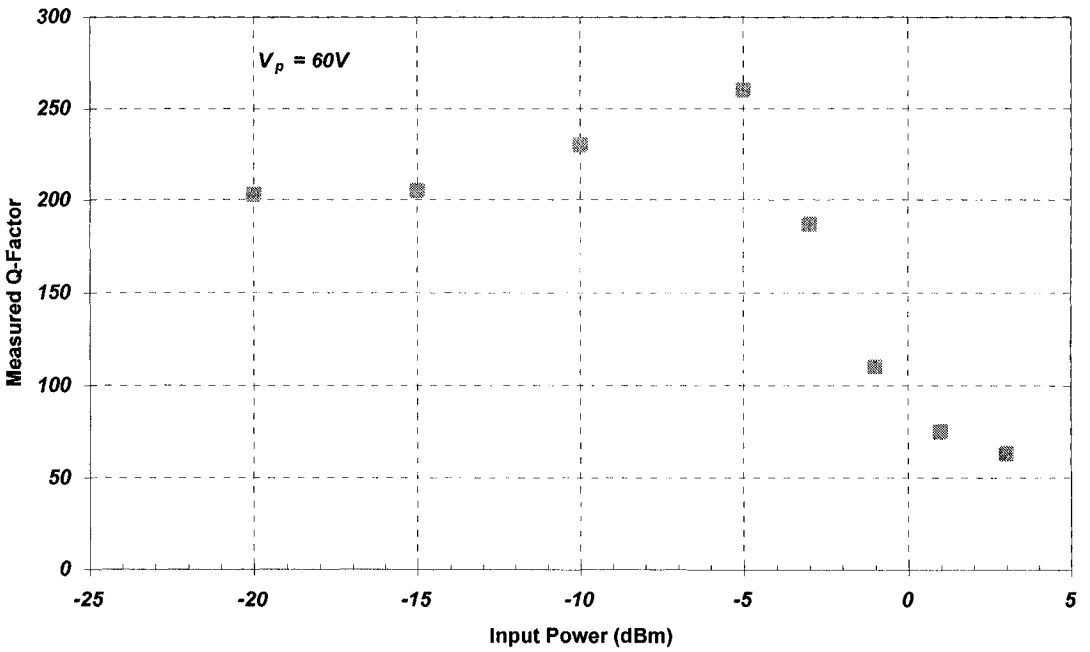

Figure 4-31: Measured Q-factor vs. input power

4.6 REFERENCES

[1] *Ansys*, Ansys Inc., http://www.ansys.com/

[2] N. Nemeth *et. al.*, "Structural modeling and probabilistic characterization of MEMS pressure sensor membranes," *ANSYS technical report*, available at: www.ansys.com.

[3] A. Wolfenden and A.C. Anthony, "Measurement of Young's modulus and damping for hexoloy SG silicon carbide", *Scripta Materialia*, vol. 41 (6), pp. 611–615.

[4] C. Compte *et. al.*, "Microprobe-type measurement of Young's modulus and Poisson coefficient by means of depth sensing indentation and acoustic microscopy," *Surface & Coatings Technology*, vol. 154 (1), May. 2002, p 42-48.

[5] F. D. Egitto, "Plasma etching and modification of organic polymers," *Pure and Applied Chemistry,* vol. 62 (9), 1990, pp. 1699-1708.

[6] L. J. Matienzo *et. al.*, "Surface composition and distribution of fluorine in plasma-fluorinated polyimide," *J. Vac. Sci. Technol. A,* vol. 6 (3), May/June 1988, pp. 950-953.

[7] J. Clark *et. al.*, "Measurement techniques for capacitively-transduced VHF-to-UHF micromechanical resonators," *Digest of Technical Papers,* the 11th Int. Conf. on Solid-State Sensors and Actuators (Transducers '01), Munich Germany, June 10-14, 2001, pp. 1118-1121.

[8] S. Young *et. al.*, "A novel low-temperature method to fabricate MEMS resonators using PMGI as a sacrificial layer," *J. Micromech. Microeng.*, vol. 15, pp. 1824-1830, 2005.

[9] Y-W. Lin *et. al.*, "Series-resonant VHF micromechanical resonator reference oscillators," *IEEE Journal of Solid-State Circuits,* vol. 39 (4), pp. 2477-2491, Dec. 2004.

[10] F. D. Bannon *et. al.*, "High-Q HF microelectromechanical filters," *IEEE Journal of Solid-State Circuits,* vol. 35 (4), pp. 512-526, April. 2000.

Chapter 5 Conclusion

5.1 SUMMARY

Table 5-1 provides a brief summary of the fabricated resonator designs along with some measured performance characteristics.

Table 5-1: Summary of fabricated designs and performance

Parameter	Value
Resonator lengths (L)	26μm to 64μm
Resonator widths (W)	10μm and 40μm
Polyimide gap thickness (g)	200nm and 300nm
SiC thickness (t_{sic})	2μm
Al thickness (t_{Al})	250nm
Chromium etch stop thickness (t_{Cr})	90nm
SiO_2 thickness (t_{oxide})	2.5μm
Substrate	6" Silicon (high-resistivity)
Measured resonant frequencies (f_0)	~ 5MHz – 25MHz
Max. measured Q-factor *(5MHz, $W = 40\mu m$, $V_p = 20V$)*	483
Max. tuning range *(5MHz, $W = 40\mu m$, $V_p = 40V$)*	17.6%
Max. tuning range *(30MHz, $W = 40\mu m$, $V_p = 100V$)*	2.0%
Max. thermal tuning range *(10MHz, $W = 40\mu m$, V_p=90V, $P_{heat} = 225mW$)*	4.8%

In this work, SiC MEM resonators were successfully fabricated using a novel low-temperature and low-stress process. Several different clamped-clamped beam designs were tested, with varying lengths, widths, and two different kinds of electrodes (rectangular and shaped). A novel thermal tuning method was also demonstrated, that significantly increased the tuning range of the resonators. Since the entire fabrication process used to create these devices did not use any high-temperature steps (>300°C), CMOS/bipolar integration may be possible in the future.

The resonant frequency of these devices ranged from ~5MHz to 25MHz, and increased with decreasing beam length. The maximum measured Q-factor of these devices was ~500 which was significantly less than the expected value of ~2000; however, losses due to thermo-elastic damping and residue in the resonator gap may be limiting the potential Q-factor.

5.2 TOPICS FOR FUTURE RESEARCH

5.2.1 Process optimization

This work has demonstrated the feasibility of a low-temperature, SiC MEMS fabrication process; however, significant optimization is still required. Specifically, the performance and yield of these devices is strongly correlated to the quality of the sacrificial layer. Since the gap is so thin, any defects or particles may result in a degradation of the Q-factor. In extreme cases, incomplete coverage of the polyimide on the bottom electrode may cause a short circuit between the input and output ports. Further work is required in order to optimize the quality of the thin polyimide sacrificial layer.

In this thesis, the minimum size of the gap that could be obtained was ~200nm, due to coverage issues. In future designs, the electrode thickness can be made smaller to accommodate a thinner sacrificial layer. In this case, however, another separate thick aluminum layer should be added to form the bond pads of the device since bonding reliability becomes an issue with thin pads.

5.2.2 CMOS/bipolar integration

To fully reap the benefits of MEMS, these devices should be directly integrated with active electronics to form a complete single-die system. Since the fabrication process of this work is all low-temperature, it can be integrated by simply adding this module on-top of the CMOS/bipolar wafer with no degradation to active elements or aluminum interconnects. Further work needs to be done to ensure that the MEM resonators can be reliably fabricated on these wafers.

5.2.3 Resonator temperature dependence and long term stability

In order to compete with commercially available quartz crystals, the issues of long term stability and temperature dependence need to be addressed. Uncompensated MEM resonators have relatively poor temperature stability in comparison to quartz crystals and thus, some form of active or passive temperature compensation is required. This can be accomplished using a number of different methods including integrated heaters and micro-ovens, using special device geometries or electronic compensation with external circuitry.

Since RF-MEMS is a relatively new technology, there is not much data on the long term stability and aging characteristics of MEM resonators. This aspect of device performance is very important, especially in telecommunications applications.